The Detection of Čerenkov Radiation from Neutrino Interactions

Robert James Boardman
Hertford College, Oxford

Thesis submitted for the degree of Doctor of Philosophy

Trinity Term 1992

Abstract

Predictions of the solar neutrinos flux at the earth imply count rates in solar neutrino detection experiments which are larger than those observed in four detectors. Many modifications to either solar, nuclear and neutrino physics have been proposed to resolve this discrepancy. In an attempt to distinguish between these alternatives a heavy water Čerenkov detector, the Sudbury Neutrino Observatory (SNO), is being constructed to measure the flavor-independent neutrino flux along with the energy spectrum of the electron-neutrinos. These measurements should determine whether solar neutrinos are changing flavor between the sun and the earth, without reference to any solar models, but require that the energy calibration in the SNO detector be accurately measured.

Several types of calibration source are being built by the SNO collaboration; sources based on Čerenkov and scintillation light are reported here. The classical theory of Frank and Tamm predicts the yield of Čerenkov photons from relativistic electrons in media used in the SNO detector and calibration sources. An electron transport routine, EGS4, is used to propagate electrons, and the predictions of the Čerenkov yield from relativistic electrons have been computed. The results have also been compared to an analytic calculation and good agreement was obtained.

Novel calibration sources of Čerenkov radiation have been constructed by encapsulating ^{90}Sr in an acrylic sphere. A more conventional source of Čerenkov radiation has been constructed by sealing a solution of ^{90}Sr inside a glass bulb. The properties of this source were found to be appropriate for use in the SNO detector. A Monte Carlo simulation code was used to predict the output of Čerenkov photons from this source and this enabled the measurement of absolute photomultiplier efficiencies. These values were consistent with values reported by several authors using other methods.

The Čerenkov sources have been used to measure the properties of the SNO photomultipliers, such as charge resolution and cathode area. The transit time spread (TTS) of the SNO photomultipliers was measured using coincident signals from a Čerenkov source with a SNO photomultiplier and a smaller photomultiplier with negligible TTS. The variation of the TTS with the operating conditions of the photomultiplier was also noted. These measurements demonstrate that event vertices in the SNO detector should be clearly resolved by using the timing of the photomultipliers alone.

Acknowledgements

Thanks are due to all members of the SNO group at Oxford for their many helpful suggestions and interest in this work. Thanks go particularly to my supervisor, Neil Tanner, who has given me the benefit of his guidance and sound advice. Thanks are due to Mike Lay who has provided me with much advice about the execution of Monte Carlo simulations using the EGS4 software. I am indebted to the many suggestions and advice from Dave Wark on many subjects, especially the computations of beta decay spectra and neutrino physics in general. Thanks go to Barrie Knox for his advice about the chemistry of calibration sources. Advice from Robert Black about the operation of the alpha spectrometer and several computing matters is appreciated. Martin Moorhead deserves thanks for many useful discussions about photocathodes and for the measurement of the optical performance of the reflectors. I would like to thank both Peter Trent and John Barton for the γ-counting radioactivity measurements of the photomultiplier bulbs and other materials for the SNO detector. My thanks go to Mike Lay, Peter Trent and Neil Tanner for their careful proof-reading of this thesis.

Several members of the SNO collaboration have kindly provided me with advice and experimental data. In particular, I would like to thank the following members of Queens University; H-B Mak for his help in the photocathode uniformity measurement and for proof-reading Chapters 5 and 7; Hamish Leslie for many useful discussions about calibration sources and for proof-reading Chapter 8; Peter Skensved for several discussions about calibrating Monte Carlo codes; and to Barry Robertson for alerting me to the problem of radiation damage.

I would like to thank the heads of the Sub-department of Nuclear and Particle Physics Prof. Perkins and (later) Prof. Cashmore, for their interest in, and support of, the SNO project. I have benefitted from a course in Relativistic Quantum Mechanics given by Robin Devenish, and a course in The Physics of Particle Detection given by Wade Allison; thanks are due for their stimulating and clear expositions of these subjects. The support staff of the laboratory deserve thanks; Bill Costar for the construction of the 'Mortar'; Maurice Lacosta for the construction of the acrylic spheres, Steve Giles for the skilled blowing of the glass bulbs for the Čerenkov sources; and Chris Goodwin for operating the spectrophotometer to measure the optical transmission of glass and acrylic.

I am pleased to acknowledge both the financial and technical support from Thorn-EMI Electron Tubes Ltd; in particular to the technical director, Ron McAlpine, for his constant interest and clear advice about many aspects of photomultiplier operation. I have benefitted from several useful discussions with the sales director, Tony Wright, especially about photomultiplier calibration.

Advice on the subject of the momentum of a photon (in a refractive medium) from Prof. Peierls is greatly appreciated.

I have found that the books *Neutrino Astrophysics* [1] by John Bahcall and *Čerenkov Radiation* [2] by J. V. Jelley both provide a tremendous source of data and references in their respective fields, and both have been an aid to thesis writing.

The financial support of the Science and Engineering Research Council (SERC) is gratefully acknowledged.

Finally, it is my pleasure to thank for my family for much support and encouragement. My girlfriend Ruth Loverseed deserves a special mention for proof-reading this thesis, and for her patience and understanding which has greatly aided its completion.

Contents

Chapter 1

Solar neutrino physics

Considerations of the amount of energy liberated by the sun on the time scale of stellar evolution lead one to conclude that the fusion of hydrogen nuclei must provide the energy radiated by the sun and other main sequence stars. In its simplest form the fusion process may be summarised by the reaction $4p + 2e^- \rightarrow {}^4\mathrm{He} + 2\nu_e + 4\gamma$ with an overall Q-value of 27.7 MeV. This process of nuclear fusion in the hot solar core has been subject to theoretical study for many years [3]. Before the relevant nuclear reactions were identified, simple models of the sun were able to account for its thermodynamic balance by the (correct) assumption that the relaxation time of the thermal transport processes are short compared to the lifetime of the sun[1]. In the 1960s physicists began to devise more detailed solar models [4] as increased knowledge of nuclear reactions and increasingly powerful computers became available.

Stated simply, these solar models attempt to simulate the possible reactions and transport phenomenon that occur in the sun, and thereby arrive at a coherent picture of the mechanisms of a stellar interior. Such a model must demonstrate that the observable features of the sun (or other star) are simultaneously consistent with a physically reasonable set of initial conditions. Any realistic model must at least be able to incorporate, if not predict, the observable features of other stars, for example the Mass-Luminosity relation. A solar model which distinguished the sun from other similar stars would be deeply unnatural. Furthermore, any such model should be able to make predictions of other observables which might be subject to experimental measurement. One such prediction is of the neutrino flux from the many individual reactions that are believed to occur during the fusion process.

These models suggested that it was the proton-proton chain, or 'pp' chain, that was the dominate proton fusion mechanism in the sun and not catalysis with heavier ions (the 'CNO cycle'). Figure 1.1 shows the reactions and branching ratios of the pp chain; data are taken from Bahcall [1]. It also emerged that considerable accuracy and attention to detail is necessary in order to predict the flux of high energy neutrinos; for example those produced from the

[1]The sun is then said to be in quasi-thermal equilibrium.

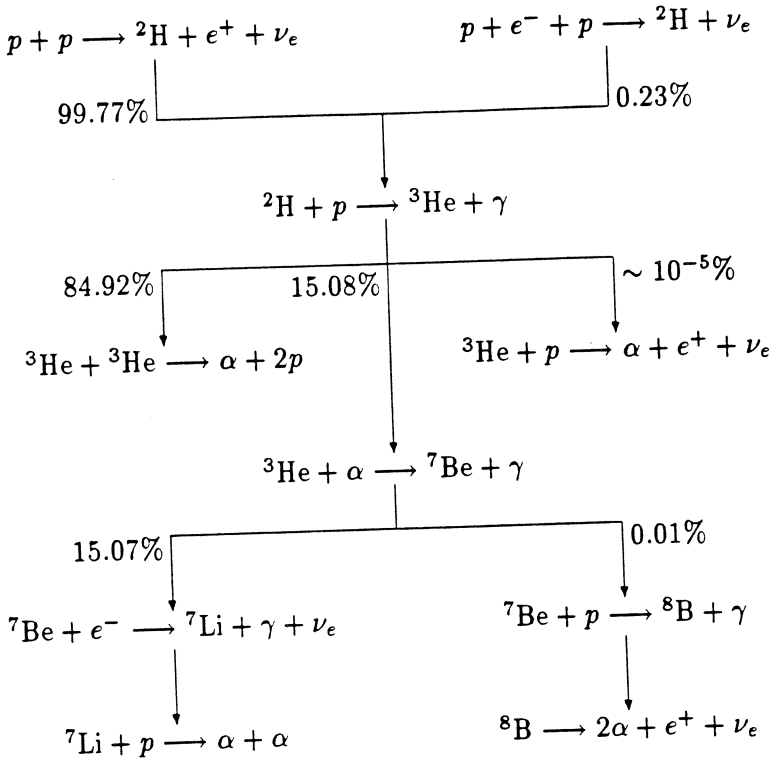

Figure 1.1: The pp chain: from Bahcall & Ulrich.

decay ${}^8\mathrm{B} \rightarrow 2\alpha + e^+ + \nu_e$ have an endpoint energy of 15 MeV. A solar model in which the central core temperature was not known with some accuracy would fail to predict accurately the ${}^8\mathrm{B}$ neutrino flux. This is because several of the reactions needed to produce ${}^8\mathrm{B}$ have a significant Coulomb barrier which provides relative suppression of the reactions of lower temperature ions. Until the advent of the recent Gallium experiments these high-energy neutrinos had a special significance as they provided the only prospect of experimental measurement of the solar neutrino flux.

Attempts to measure the flux of solar neutrinos are made very difficult by the short range of the weak interaction which gives very small reaction cross-sections for neutrino interactions. However the efforts of the early experimentalists in the field (particularly Ray Davis) established a radiochemical Chlorine experiment to measure the neutrino flux using a target containing ${}^{37}\mathrm{Cl}$. An electron neutrino and a ${}^{37}\mathrm{Cl}$ nucleus react through a charged-current interaction, producing an ${}^{37}\mathrm{Ar}$ nucleus and an electron in the final state. A neutrino interaction is inferred from the detection of the Auger electrons produced from the electron-capture decay of an ${}^{37}\mathrm{Ar}$ nucleus. The results of this radiochemical experiment (see below) have always been less than the theoretical predictions of the rate of ${}^{37}\mathrm{Ar}$ atoms produced from solar neutrinos. This disagreement has become known as the solar neutrino problem. Subsequent results from

three other solar neutrino flux measurements are all consistent with a solar neutrino flux which is less than that predicted by the standard solar model. After a review of the standard solar model, existing and future solar neutrino experiments are presented, and proposed solutions to the solar neutrino problem are discussed.

1.1 The standard solar model

The term 'standard solar model' refers to a class of models which make similar widely accepted assumptions about the stellar evolution equations and the boundary conditions applicable to the sun. Usually an iterative technique is used to converge to a final state which is the current sun.

1.1.1 Stellar evolution

The starting point for computations of the distribution of matter and radiation in the sun is the hypothesis of hydrostatic equilibrium. The observed long term stability of the sun provides strict limits on the allowed deviations from this hypothesis, and only small oscillations are permitted without another (unknown) mechanism. The study of periodic deviations, Helioseismology, provides very useful information about the density of the sun and all Helioseismology data are consistent with an internal structure which is free from significant turbulence. For a clear account of the implications of Helioseismology, see Christensen-Dalsgaard *et al.* in reference [6]. No likely mechanism has yet been identified, (on the grounds of energy conservation), which could cause a mixing of the core material sufficient to cause a reduction in the central temperature enough to reduce the ^{8}B neutrino flux so as to resolve the solar neutrino problem. However since no direct method of estimating the magnitude of core instabilities is currently availible, the statement that core-mixing is negligible must be regarded as a hypothesis [7].

Assuming the hypothesis of hydrostatic equilibrium, the gravitational inverse square law provides a relation between the density of matter and the pressure gradient in the sun[2]. The general solution for an arbitrary system would involve non-symmetrical solutions of Poisson's equation for the gravitational potential: $\nabla^2\Phi = -4\pi G\rho(\mathbf{r})$, where $\Phi(\mathbf{r})$ is the potential and $\rho(\mathbf{r})$ the matter density. However, deviations from spherical symmetry are believed to be small for the sun (for example, the shape of the sun is spherical to about 5 parts in 10^5), and hence symmetry is believed to be a good assumption for solar models. The pressure required to balance the gravitational force can be deduced by considering the forces on a spherical shell of radius r, resulting in the well-known relation

$$\frac{dP}{dr} = -\frac{G\,M(r)\,\rho(r)}{r^2}\,, \tag{1.1}$$

[2]Strictly this relation is only true in a non-rotating system.

where $M(r)$ is the total mass enclosed within a radius r. The angular frequency of rotation is set equal to zero in a standard solar model.

The equation of state in the sun provides another relation between pressure and density, enabling a simultaneous solution to be constructed. Fortunately, the equation of state in the solar core is similar to an ideal gas because matter (except for the heavy elements) is fully ionized and atomic interactions are thereby simplified. In addition to the thermal pressure due to the thermal motion of the plasma constituents, contributions from radiation pressure of photons, degeneracy pressure of electrons (a consequence of the Pauli principle), and screening interactions must be included in the equation of state [8]. This can be expressed as

$$P(r) = \frac{\sigma}{3}T^4 + \frac{\rho kT(1+D)}{\mu}, \tag{1.2}$$

where k is the Boltzmann constant, σ the Stefan-Boltzmann constant, μ the mean molecular mass and D incorporates the corrections listed above. The sum of these expansive pressures is then equated with the attactive force of gravity, to satisfy hydrostatic equilibrium.

The core material of the sun is believed to be stable with respect to convection and to thermal perturbations [9] and so the transport of energy in the centre of the sun is dominated by photon diffusion. The contribution from the electron conduction opacity κ_c to the total (mean) opacity κ_T given by

$$\frac{1}{\kappa_T} = \frac{1}{\kappa_c} + \frac{1}{\kappa_{rR}}, \tag{1.3}$$

is believed to be small in the solar core relative to the radiative opacity κ_{rR}. The opacities used in the standard solar model of Bahcall & Ulrich [5] and others are derived from computer codes developed by the Los Alamos National Laboratory to calculate the opacities as a function of nuclear abundances, density and temperature. (For an authoritative account see W. F. Huebner in Chapter 3 of reference [10].) For thermodynamic reasons the accuracy of these algorithms is crucial when computing the temperature profile in the solar core [11]. This profile is in turn vital for an accurate prediction of the ^{8}B neutrino flux as the latter is very sensitive to the plasma temperature, due to the Coulomb barrier which impedes the ^{7}Be(p,γ)^{8}B reaction.

So how accurate are the computed values of radiative opacity ? It is fortunate that the processes which contribute to the impedance of radiation through a plasma of light elements at high temperature are well understood and in principle relatively 'simple' to calculate. Inverse bremsstrahlung from protons and alpha particles, and the scattering of photons by free electrons, are believed to contribute a significant fraction of the total radiative opacity. However, in the solar core there is a higher abundance of heavy elements (metalicity), which contribute a significant fraction to the total opacity. Moreover these contributions are difficult to estimate accurately not only because their interactions are more complex, but also their abundances are subject to significant uncertainties. Notwithstanding these concerns, it seems likely that

the opacity coefficients assumed in the standard solar model are within 5% of the true values; it is unlikely that these uncertainties could resolve the solar neutrino problem.

In an alternative approach, several authors (for example Dziembowski *et al.* [12]) have used the large quantity of p-mode Helioseismology data to compute the pressure and temperature distributions in the solar core. Their results for the speed of sound are in agreement with those reported by Christensen-Dalsgaard *et al.* [6]. Dziembowski *et al.* [12] conclude that the differences between the solar model of Bahcall & Ulrich and these Helioseismology data can be removed by invoking a slightly increased opacity in the core material. Dziembowski *et al.* [12] deduce that the solar model of Bahcall & Ulrich is likely to *underestimate* the signal in the Chlorine experiment, although such a conclusion is not accepted as definitive by others.

1.1.2 Input parameters and boundary values

With the mechanism for simulating solar phenomenon in place, the input parameters need to be defined. These can be divided into two classes: the boundary conditions specific to our sun and the parameters (cross-sections, lifetimes, Q-values etc.) describing the nuclear phenomena which liberate heat. The only direct experimental constraints on the standard solar model are the observed values of mass, radius, photon luminosity, asphericity and age[3].

Other initial conditions that must be specified are the initial abundances of the heavy elements (heavier than helium). These have been inferred by astronomers by observing the electromagnetic spectrum (around the visible region) of photons from the sun and thereby deducing the present heavy element abundances at the solar surface. By hypothesis, this represents the initial elemental abundances (for nuclei heavier than mass 17) because changes due to nuclear reactions are thought to be negligible in this region. The (1988) standard solar model of Bahcall & Ulrich [5] incorporates the initial abundances of Grevesse [13], although these are in good agreement with those reported in another survey by Aller [14]. Models of the sun which use a low value for the helium abundance (sufficient to resolve the solar neutrino problem) appear to be ruled out by Helioseismology data, particularly the 5-minute oscillations [6].

The nuclear reactions that occur in the sun take place at lower energies than those normally measured in laboratory experiments and so some form of extrapolation is necessary to compute their cross-sections at low energies. One common parameterization for strongly exothermic reactions is to set

$$\sigma(E) = \frac{S(E)}{E}\exp(-2\pi\eta) \qquad \text{where} \qquad \eta(E) = \frac{\alpha z Z}{v/c} \tag{1.4}$$

for two ions of charges ze and Ze which collide with relative velocity v giving a kinetic energy

[3] Metoric ages are believed to provide a good indication of the sun's age. These are closely distributed about 4.55×10^9 years, which is the currently adopted age for the standard solar model.

Reaction	Label	Q-value	$S(0)$	dS/dE
$p(p,e^+\nu_e)^2$H	pp	1.442	4.07×10^{-22}	4.52×10^{-24}
$p(pe^-,\nu_e)^2$H	pep	1.442	-	-
^{2}H$(p,\gamma)^3$He	-	5.494	2.5×10^{-4}	7.9×10^{-6}
^{3}He$(p,e^+\nu_e)^4$He	hep	19.797	8×10^{-20}	-
^{3}He$(^3$He$,2p)^4$He	-	12.86	$5.5 \times 10^{+3}$	-0.9
^{3}He$(^4$He$,\gamma)^7$Be	-	1.586	0.54	-3.1×10^{-4}
^{7}Be$(p,\gamma)^8$B	^{7}Be	0.137	0.0242	-3×10^{-5}
^{8}B$(e^+\nu_e)^8$Be	^{8}B	17.98	-	-
Units		MeV	keV barns	barns

Table 1.1: Values of some reaction cross-section parameters.

E in the centre of mass system. The factor $\exp(-2\pi\eta)$ comes from the Gamow penetration of the Coulomb barrier whilst the $1/E$ dependence comes from the (λ^2) overlap of the particle wavefunctions. $S(E)$ is a slowly varying function expressing the small energy dependence of the matrix element. Values of the cross-section parameters of some reactions (with Coulomb barriers) in the pp chain are shown in Table 1.1. Data are taken from Bahcall [1] and Parker in Chapter 2 of reference [10].

1.1.3 Solar model neutrino fluxes

Many authors have devised standard solar models and some have used these to predict the fluxes of neutrinos from various reactions. These models predict many parameters such as matter density and temperature profiles but for the current work only the neutrino predictions will be considered. Figure 1.2 shows the energy spectrum of solar neutrinos taken from the Bahcall & Ulrich standard solar model [5]. The neutrinos from the pp chain are shown by solid curves whilst those from the CNO cycle are shown by dashed curves. The line sources have units of cm^{-2} s^{-1} whilst the continuum sources have units of cm^{-2} s^{-1} per MeV. Table 1.2 lists the predictions of several standard solar models which explicitly give the neutrino fluxes. Several other groups [15] [16] have calculated neutrinos fluxes from their models but do not report explicit values in their papers. The latter work by Sackman *et al.* [16] reviews the successes and failures of the standard solar model.

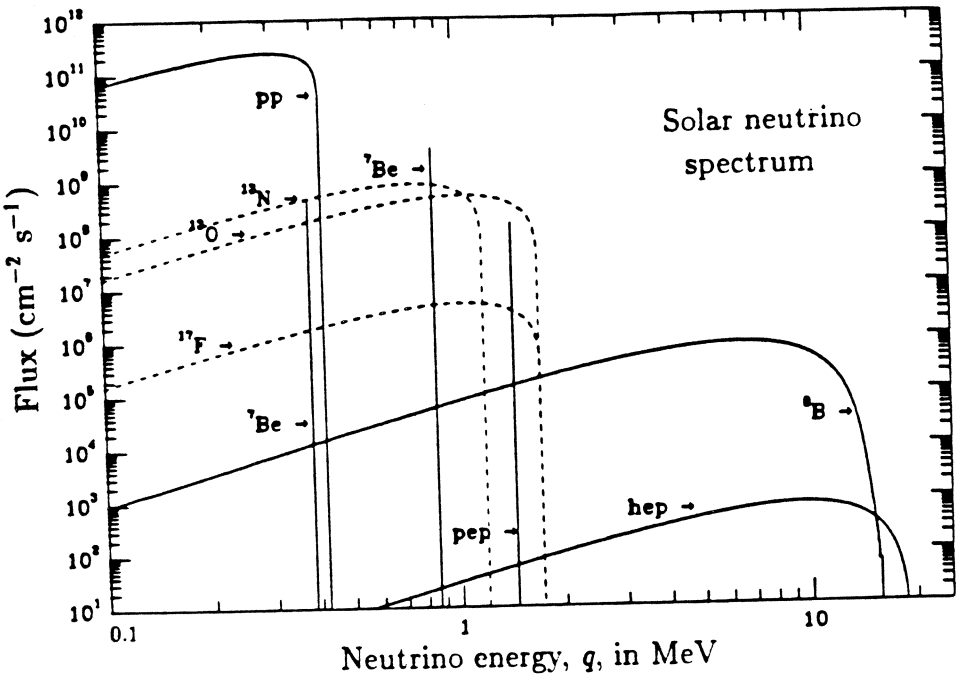

Figure 1.2: The energy spectrum of solar neutrinos from Bahcall & Ulrich.

The first column of Table 1.2 contains values from the Bahcall & Ulrich (1988) standard solar model [5] with errors described as a 'total theoretical range', which is claimed by the authors to be equivalent to three standard deviations. The second column shows the values reported in the Bahcall model of 1982. The next five columns show various reported flux values in order of increasing age back to Abraham and Iben [22] from 1971. As the experimental values of the reaction cross-sections and the opacities are being refined continually the later reports are thought more likely to be accurate. Reference to the original papers should be made for the uncertainties of these fluxes and their interpretation, as some authors quote one standard deviation and some quote three. Also, as stated by Bahcall, the distribution of the uncertainties is not well understood, and for this reason context is required to interpret them.

The predictions of the rate of ^{8}B neutrino production are quite sensitive to the matter temperature and the standard solar model of Bahcall & Ulrich [5] predicts that half of the ^{8}B neutrinos from our sun are produced in the central 1.1% (by mass) where the temperature exceeds 15×10^6 Kelvin. Often the sensitivity of the total neutrino flux to the central core temperature is expressed via a power law approximation of type $\phi(^8\mathrm{B}) \sim T^{\zeta}$ where ζ is a number determined by executing many solar models and noting the correlation between ϕ and T. Such a procedure [1] reveals that the ^{8}B flux is very sensitive to temperature $\phi(^8\mathrm{B}) \sim T^{18}$ and the ^{7}Be neutrinos are quite sensitive: $\phi(^7\mathrm{Be}) \sim T^8$. However since the number of pp reactions is well constrained by the energy release and this in turn fixes the central core

Reaction	[5]	[17]	[18]	[19]	[20]	[21]	[22]	Units
$p(p,e^+\nu_e)^2$H	6.0 ± 0.12	6.07	5.98	5.95	-	6.61	5.95	10^{10} cm^{-2} s^{-1}
$p(pe^-,\nu_e)^2$H	1.4 ± 0.07	1.5	1.3	1.2	1.5	-	1.50	10^{8} cm^{-2} s^{-1}
^{3}He$(p,e^+\nu_e)^4$He	7.6	-	-	-	-	-	-	10^{3} cm^{-2} s^{-1}
^{7}Be$(e^-,\nu_e)^7$Li	4.7 ± 0.7	4.3	4.18	4.6	4.6	3.16	5.15	10^{9} cm^{-2} s^{-1}
^{8}B$(e^+\nu_e)^8$Be	5.8 ± 2.1	5.6	3.8	5.3	6.8	3.9	9.61	10^{6} cm^{-2} s^{-1}
^{13}N$(e^+\nu_e)^{13}$C	6.1 ± 3.0	5.0	-	4.19	6	3.1	7.1	10^{8} cm^{-2} s^{-1}
^{15}O$(e^+\nu_e)^{15}$N	5.2 ± 3.0	4.0	-	5	6.0	2.4	3.71	10^{8} cm^{-2} s^{-1}
^{17}F$(e^+\nu_e)^{17}$O	5.2 ± 2.4	5	-	-	-	-	-	10^{6} cm^{-2} s^{-1}

Table 1.2: Explicit predictions of the solar neutrino fluxes.

temperature, given that the total opacity is also known.

1.2 Solar neutrino detection

To date four experiments have reported positive results of solar neutrino detection, three radiochemical experiments and one water Čerenkov detector. The experimental evidence for these measurements is briefly reviewed here.

1.2.1 The Chlorine experiment

The Chlorine experiment is located some 4850 feet below ground (equivalent to about 4100 m of water) in the Homestake mine in South Dakota to reduce background induced by cosmic radiation. The detector contains 615 tons of liquid perchlorethylene (C_2Cl_4), which represents a target of about 2.2×10^{30} atoms of ^{37}Cl. The unit 'SNU' is defined to be equal to one capture per 10^{36} target atoms per second, and therefore 1 SNU is equivalent to the creation of about 0.187 atoms of ^{37}Ar per day in the Chlorine experiment. As the half-life of ^{37}Ar is about 35 days, extractions are performed at monthly intervals. The background from cosmic ray muons has been the subject of several studies [23] which are in good agreement, and is consistent with a background rate of 0.08 ± 0.03 atoms of ^{37}Ar per day. Together with an inert ^{38}Ar carrier added at the start of a run, atoms of ^{37}Ar are extracted from the tank by purging with helium, and then purified. This mixture is then counted in a proportional counter for several months

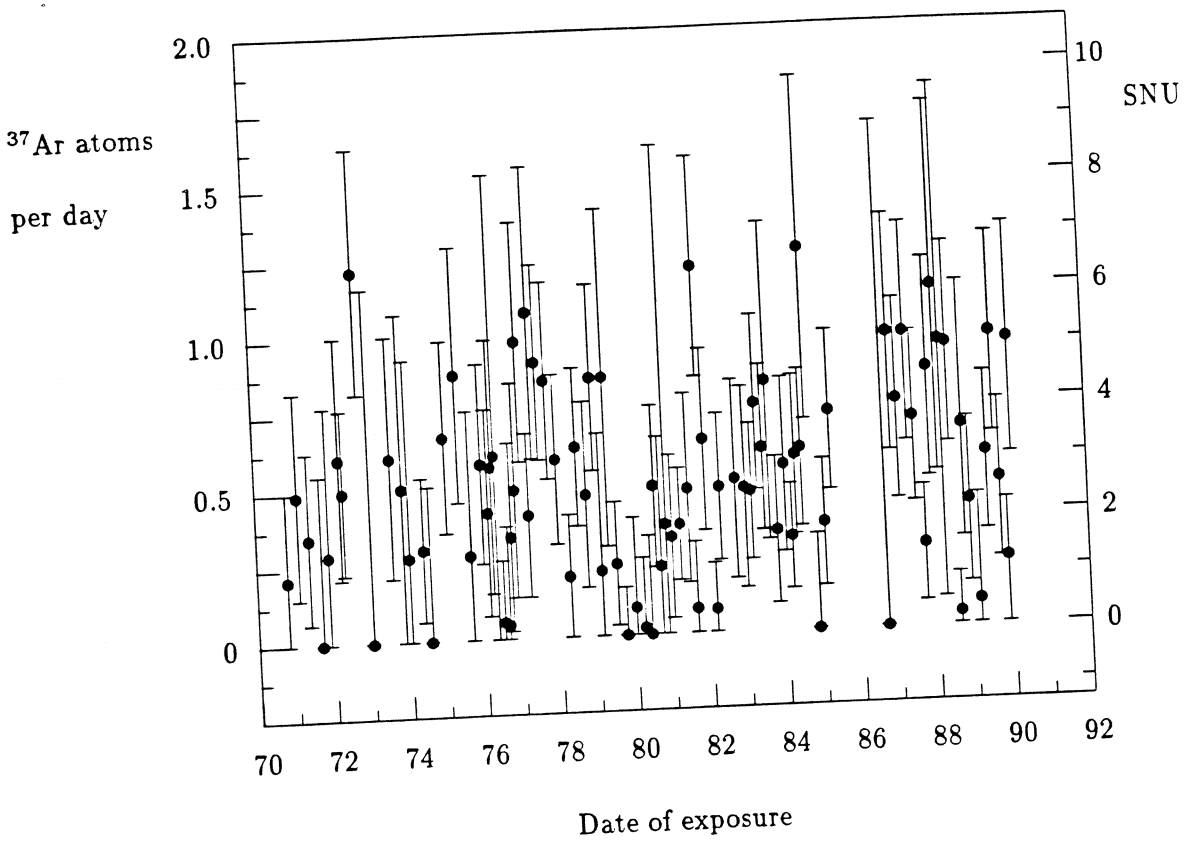

Figure 1.3: The results of the Chlorine experiment.

(several half-lives), and background events are reduced by rejecting events which do not have a pulse-height and rise-time consistent with an Auger electron. The combined extraction and counting efficiency of this process has been measured [23] and was shown to be greater than 95 %. The results of the many extractions from 1970 to the present are shown in Figure 1.3; the average capture rate for these data is about 2.2 $\pm$ 0.3 SNU.

The initial (pre-1964) value of the cross-section of the electron-neutrino capture reaction on the ^{37}Cl nucleus was actually too small. However once the spins, parities and energies of the excited states of mass 37 nuclei were measured precisely, an accurate estimation of the transition rate to the excited states of ^{37}Ar was possible. In particular, the large matrix element for transitions to the isobaric analogue state ($J^P = 3/2^+$, T = 3/2, at about 5 MeV in ^{37}Ar), means that the sensitivity to neutrinos from ^{8}B is greatly enhanced [24]. Using the reaction ^{38}Ar(p,d)^{37}Ar, Parker and Howard [25] were able to study the properties of the even parity states of ^{37}Ar, and verify the existence of the analogue state 4.98 MeV above the ground state. Figure 1.4 shows the ground and analogue state in ^{37}Ar in a greatly simplified nuclear level scheme. Also shown in the figure are some predictions of the capture rate in the Chlorine experiment shown in chronological order of publication from the latest report from Bahcall and Pinsonneault [26] (1992) to Abraham and Iben [22] (1971).

Predictions of the ^{37}Cl capture rate

Model	[26]	[16]	[5]	[17]	[18]	[19]	[27]	[28]	[20]	[21]	[22]
SNU	8.0	7.68	7.9	7.6	5.8	7.4	13.3	8.3	8.7	6.4	5.06

The neutrino capture reaction

$$\nu_e + {}^{37}\mathrm{Cl} \rightarrow {}^{37}\mathrm{Ar} + e^-,$$

has a threshold of 814 keV.

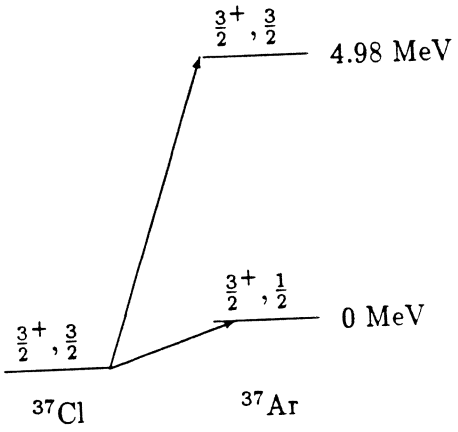

Figure 1.4: Neutrino capture reactions on ^{37}Cl. The labels on each nuclear level denote J^P, T. Only the ground state and analogue state of ^{37}Ar are shown.

The (1988) standard solar model of Bahcall & Ulrich [5] predicts a capture rate in the Chlorine detector of 7.9 $\pm$ 2.6 SNU where the errors quoted here are the 'total theoretical range' as described previously. Of this 7.9 SNU, about 1.1 SNU is due to the flux of ^{7}Be neutrinos and most of the rest is due to the ^{8}B neutrinos. Although the precise statistical significance of the discrepancy between the theoretical and experimental values is debated by workers in the field, there is a general consensus that the experimental results and theoretical predictions based on the standard solar model and current knowledge of neutrino propagation are inconsistent. There are many views about the origin(s) of the deficit.

1.2.2 The Kamiokande II experiment

The Kamiokande II detector [29] is a cylindrical water Čerenkov detector containing 2142 tonnes of high-purity water as a target for neutrino electron scattering. In order to shield it from cosmic rays, the detector is located at a depth of about 1 km (equivalent shielding to about 2700 metres of water) in the Kamioka mine, Japan. The Čerenkov radiation from the scattered electrons is detected with 948 Hamamatsu R1449 photomultiplier tubes with a large photocathode diameter of about 500 mm. These provide about 20% coverage of the walls of the cylindrical tank. There is an anticoincidence veto surrounding the main detector with

Fiducial volume	680 tonnes
Trigger efficiency	50 % at 5.2 MeV
	90 % at 7.5 MeV
Energy resolution	20 % $\times\sqrt{}$ 10/E(MeV)
Energy calibration	better than $\pm$ 5%
Vertex resolution	1.5 m at 10 MeV
Angular resolution	$\pm$ 30 degrees at 10 MeV

Table 1.3: The performance of the Kamiokande II detector.

another 1800 tonnes of water viewed by another 123 photomultipliers. The performance of the Kamiokande II detector is summarised in Table 1.3 and the parameters are measured after the photomultiplier gain change in 1988.

The Kamiokande II detector was originally designed for the detection of signals from proton decay and so was not built to have especially low levels of internal radioactivity. The Kamiokande collaboration took several steps to improve the signal-to-background ratio for detecting solar neutrinos:

1. Ion-exchange resins were installed to remove uranium and ^{226}Ra from the water. This reduced the number of triggers due to the ^{214}Bi beta decay.

2. The water tank and purification system were sealed to prevent the entry of ^{226}Ra produced in the mine. An inert cover gas was used.

3. The anticoincidence volume attenuated γ-rays from the rock, and this flux was further attenuated, along with γ-rays from the photomultipliers, by using a fiducial volume of only 680 tonnes. A further veto of events with a reconstructed direction of motion into the fiducial volume was made for vertex positions near the edge of the fiducial volume.

4. Cosmic ray muons (and pions from their inelastic scattering) were vetoed. The radioactive spallation products formed along the tracks of these cosmic rays were also vetoed by not counting signals for 50 seconds after a muon passed through the detector.

After all these measures were taken to reduce backgrounds the trigger event rates were still larger than those expected from solar neutrinos. This is illustrated in Figure 1.5, taken from Hirata *et al.* [29], which shows the trigger rates as a function of electron energy. The

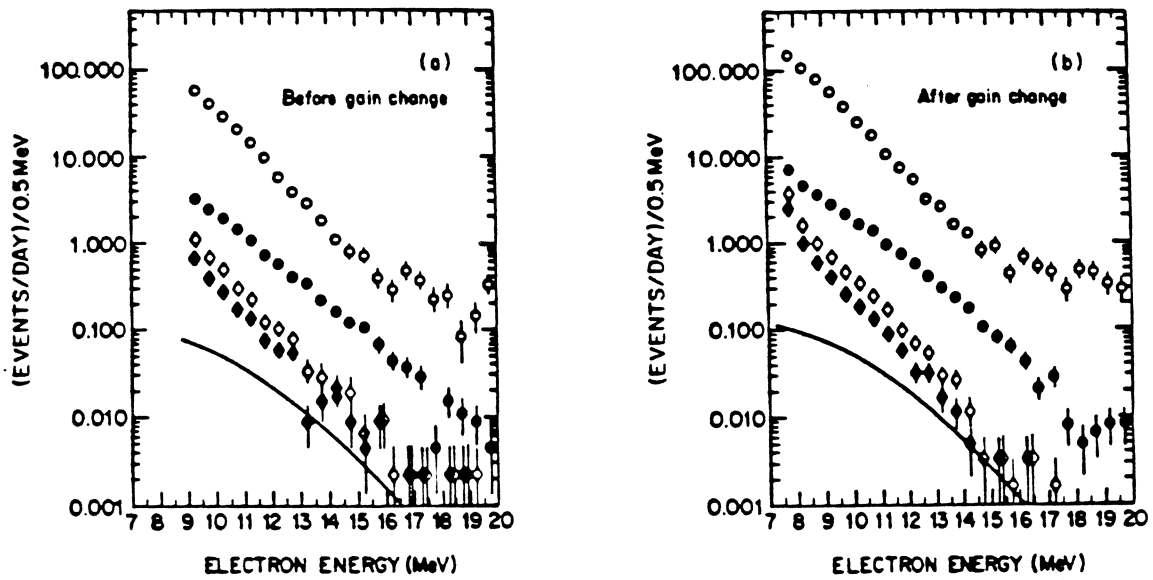

Figure 1.5: Trigger rates in the Kamiokande II detector, see text.

open circles show all events, the full circles show the events in the fiducial volume. The open diamonds show the events in the fiducial volume after the spallation cut, and after the γ-ray cut events are shown by the full diamonds. The solid curve shows the Bahcall & Ulrich (1988) standard solar model prediction of the electron scattering rate due to solar neutrinos. To distinguish the background from the signals due to solar neutrinos the reconstructed initial electron direction was used, see Figure 1.6. The solid line is a Monte Carlo prediction of the angular distribution of events assuming the standard solar model neutrino flux, and the points represent experimental data. $\theta_{\rm Sun}$ is the angle between the vector pointing away from the sun at the detector and the recontructed direction of the electron.

The result of the analysis of the data is that the flux of ^{8}B solar neutrinos compared with the (1988) standard solar model is:

$$\frac{\text{Kamiokande II data}}{\text{Bahcall \& Ulrich SSM}} = 0.46 \pm 0.05(\text{stat}) \pm 0.06(\text{syst.}) \qquad (1.5)$$

The Kamiokande collaboration have looked for time correlations (for example the day/night effect or correlations with sunspot number) in the solar neutrino signal and none have been found, (see Suzuki [30] for a review). The collaboration infers that non-adiabatic large-angle neutrino flavor mixing solutions of the MSW effect (see below) are favoured if this is the cause of the solar neutrino problem.

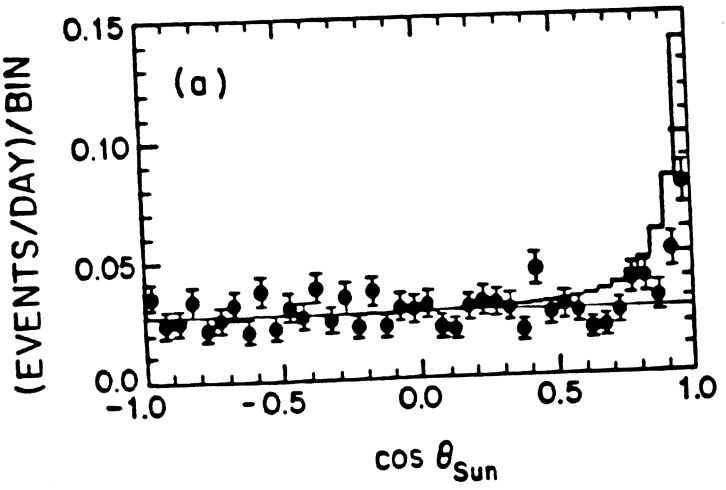

Figure 1.6: Angular distribution of Kamiokande events for 1040 days.

1.2.3 The Gallium experiments

The great attraction of using ^{71}Ga as a target for radiochemical solar neutrino detection is the low energy threshold for the inverse beta decay reaction

$$\nu_e + {}^{71}\mathrm{Ga} \rightarrow {}^{71}\mathrm{Ge} + e^- \qquad \text{Threshold energy} = 233 \text{ keV}. \tag{1.6}$$

The low energy pp neutrinos from the reaction $p + p \rightarrow {}^2\mathrm{H} + e^+ + \nu_e$ which have an endpoint energy of 420 keV can be measured using this reaction. These pp neutrinos are attractive to experimentalists for two reason. Firstly they are produced with higher fluxes than from other reactions, see Table 1.2, and secondly the predictions of the flux are more reliable than the other neutrino sources. The predicted capture rates from various solar neutrino sources are shown in Figure 1.7 below; the data are taken from the standard solar model of Bahcall & Ulrich (1988). Two groups, the SAGE collaboration and the GALLEX collaboration, are measuring the rate of production of ^{71}Ge from ^{71}Ga and both groups have now reported results.

The Soviet American Gallium Experiment (SAGE) is situated in a low background laboratory under Mount Andyrchi in the Baksan Valley of the Northern Caucasus, USSR. The overburden of rock is equivalent to about 4700 m of water. The target has now been upgraded to 60 tonnes (originally 30 tonnes) of gallium metal kept above its melting point of 29.8°C in 4 reaction vessels. The chemical extraction of ^{71}Ge atoms is complex, see reference [31], and a simplified account is given here. Before each run a small amount of natural germanium carrier is added. After 4 weeks of exposure to solar neutrinos, concentrated HCl is added, in the presence of H_2O_2, and the germanium is collected and concentrated by vacuum distillation.

	SAGE	Gallex
Mass of gallium	60 tonnes	30.3 tonnes
Chemical form of ^{71}Ga	Gallium metal	Gallium tetrachloride
Exposure interval	4 weeks	3 weeks
Counting interval	2-3 months	$>$ 6 months
^{71}Ge background rate	$<$ 3.3 SNU	$\sim$ 6 SNU
Auger electrons counted	K and L peaks	K and L peaks

Table 1.4: A comparison of the gallium experiments.

Germane, a gas suitable for proportional counting, is then synthesized and purified by gas chromatography. The extraction efficiency has been measured and is reproducible and stable at about 80%.

The standard solar model prediction of 132 SNU corresponds to 2.4 atoms of ^{71}Ge produced per day from a target of 60 tonnes of Gallium. The ^{71}Ge decays by electron capture with a half life of 11.4 days, and since the nucleus decays directly to the ground state of ^{71}Ga the decay can only be inferred from the detection of Auger electrons. The Auger electron spectrum from the decay of ^{71}Ge has a peak at about 10 keV from K-shell electron capture and a peak at 1.2 keV from L-shell electron capture. Background suppression is achieved by selecting those events which have the short risetime and energy consistent with an Auger electron. To veto external radioactivity the counters are surrounded by active NaI detectors. In the SAGE experiment the backgrounds were initially too high at 1.2 keV to permit counting of the L peak, but these have been overcome, and the L-shell electron capture decays are now used in addition to those from K-shell capture.

The Gallex facility [32] is located in hall A of the Gran Sasso underground laboratory, Italy, at a depth equivalent to 3300 m of water. Unlike SAGE, the Gallex collaboration have a target of 101 tonnes of gallium chloride solution equivalent to 30.3 tonnes of gallium. Chemical extraction of ^{71}Ge atoms is made easier than in the SAGE experiment as they form germanium chloride molecules which can be swept out of solution by an inert gas. The germanium chloride is then reabsorbed into water and converted to the counter germane gas (GeH_4), further purified, and finally counted in a low background proportional counter. Both groups have made extensive investigations of the extraction efficiency. Like SAGE, Gallex count the Auger electrons from the electron capture decay of ^{71}Ge in a proportion counter

Capture rates predicted for ^{71}Ga from Bahcall & Ulrich.

Neutrino source	pp	pep	hep	^{7}Be	^{8}B	^{13}N	^{15}O	^{17}F	Total
Capture rate (SNU)	70.8	3.0	0.06	34.3	14.0	3.8	6.1	0.06	132 ± 7

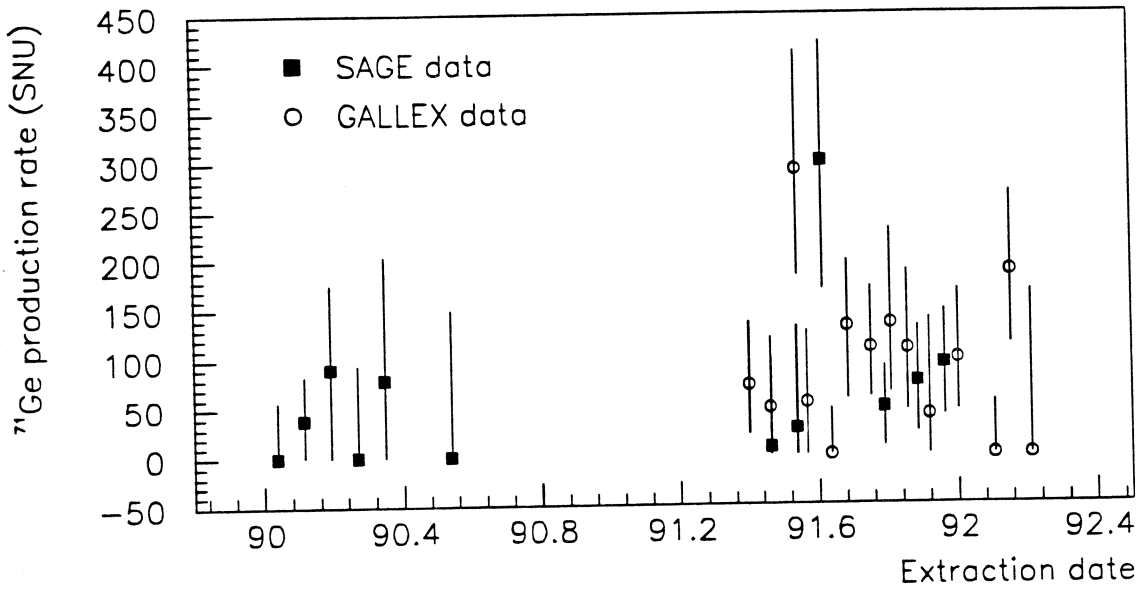

Figure 1.7: The predicted and measured ^{71}Ge production rate due to solar neutrinos.

and use risetime and pulse height information to veto background signals. Gallex also uses data taken from both the K-shell and L-shell peaks of the Auger electron spectrum. A simple comparison of the SAGE and Gallex experiments is shown in Table 1.4.

At the Neutrino 92 conference the latest data were presented from the Gallex collaborators [33] and the results of the extractions are shown in Figure 1.7 along with the prediction from the standard solar model of Bahcall & Ulrich (1988). At the ICHEP (1992) conference the SAGE collaboration [34] presented the results of 12 extractions which are also shown in Figure 1.7. The combined results of all 12 extractions in 1990 and 1991 is

$$\textbf{SAGE} \qquad ^{71}\text{Ge rate from solar } \nu_e \;=\; 58 \pm {}^{17}_{24}\,(\text{stat}) \pm 14\,(\text{syst.})\,. \qquad (1.7)$$

The SAGE collaboration is still analysing the systematic errors from the last 6 runs and so a combined result for the 12 extractions has not yet been given. After 14 extractions the Gallex collaborators report a result of

$$\textbf{Gallex} \qquad ^{71}\text{Ge rate from solar } \nu_e \;=\; 83 \pm 19\,(\text{stat}) \pm 8\,(\text{syst.})\,. \qquad (1.8)$$

These results are consistent and any disagreement has low statistical significance, and both

these experiments are consistent with a solar neutrino deficit.

1.3 Possible solutions to the solar neutrino problem

Many solutions to the discrepancy between the predictions of the standard solar model and the experimental measurements of the neutrino flux have been suggested. These fall into four main categories:

1. The standard solar model or boundary conditions are incorrect. Critics have suggested many modifications to the standard solar model to resolve the discrepancy such as low metalicity, rapid core rotation, strong magnetic fields, various mixing phenomena and others. There is a vast field of literature proposing non-standard solar models; see Bahcall [1] for a review.

2. The nuclear physics (expecially cross-section data) used to predict the neutrino production rates are incorrect. Most important for the ^{8}B neutrino flux are the $^3\mathrm{He}(^4\mathrm{He},\gamma)^7\mathrm{Be}$, $^7\mathrm{Be}(e^-,\gamma\nu_e)^7\mathrm{Li}$ and particularly the $^7\mathrm{Be}(p,\gamma)^8\mathrm{B}$ cross-sections.

3. The propagation of neutrinos from their creation in the sun to the earth is not sufficiently well understood. Simple decay of electron neutrinos is thought to be strongly disfavoured from the observation of (anti)neutrinos from supernova 1987A. This leaves the possibility of some neutrino flavor mixing and/or spin flip, both of which require physics beyond the standard model, and in particular at least one species of neutrino must be massive.

4. The experimental evidence is either flawed or somehow misinterpreted. With four experiments reporting low values of the solar neutrino flux using three different experimental methods, there is now a growing belief in the field that this is unlikely.

The first of these classes of explanation is somewhat speculative as there is no experimental evidence for any of the new phenomena. Moreover the recent successes of the standard solar model at predicting the Helioseismological oscillations in the sun give weight to evidence that the helium abundance is correctly assumed in the standard solar model. The most recent standard solar model of Bahcall and Pinsonneault [26] includes more refinements of initial abundances together with new Livermore radiative opacities, gravitational diffusion, improved screening corrections and the others. Yet the prediction for the Chlorine experiment is still 8.0 ± 3.0 SNU. It seems that the solar models have reached a level of sophistication at which the ^{8}B neutrino flux should be calculable with fair accuracy, and yet the solar neutrino problem remains. The nuclear physics data could be incorrect, but the errors needed in the cross-sections to resolve the solar neutrino problem are large compared to the uncertainties derived from the spread of the reported values. This leaves the third possibility of an explanation in

terms of neutrino propagation, and non-standard physics, which is the most exciting to particle physicists. Suggested modifications in neutrino propagation phenomena are now reviewed.

1.3.1 Vacuum oscillations

One proposed solution to the solar neutrino problem is that between their creation in weak interactions in the sun, and their detection on earth, the neutrinos change flavor by some mechanism. This can happen by oscillation phenomenon if the neutrino flavor eigenstates are different than the mass (propagation) eigenstates and at least one neutrino is massive. This supposes physics beyond the standard model of electroweak interactions, but the extension is quite a reasonable one. For example, in the neutral kaon system the weak interaction (CP) eigenstates K^0 and $\bar{K}^0$ are different from the mass eigenstates K_L, K_S and since there exists a mass difference between K_L and K_S, mixing of CP states occurs. More generally the transformation (the Kobayaski Maskawa matrix) between the weak and mass eigenstates of the three quark families gives a unitary matrix described by three angles and one observable phase. If lepton number is not conserved then an analogous transformation would apply in the lepton sector also.

The most simple manifestation of such a mechanism for solar neutrinos is oscillations of neutrino flavor as the neutrino propagates through a vacuum. This might solve the solar neutrino problem because all measurements of solar neutrinos so far have been sensitive only to electron neutrinos[4] and neutrinos which oscillated to a different flavor would not be counted. Suppose for simplicity that there are just two flavors of Dirac neutrino labelled ν_e and ν_μ whose basis states are $|\nu_e>$ and $|\nu_\mu>$ which form a complete orthonormal set in the flavor basis. If there are mass eigenstates $|\nu_1>$ and $|\nu_2>$ distinct from $|\nu_e>$ and $|\nu_\mu>$ and one of these states is massive then there will be a unitary transformation (rotation) between the representations:

$$\begin{aligned} |\nu_e> &= \cos\theta\ |\nu_1> + \sin\theta\ |\nu_2> \\ |\nu_\mu> &= -\sin\theta\ |\nu_1> + \cos\theta\ |\nu_2>\ , \end{aligned} \tag{1.9}$$

where θ is the mixing angle conventionally chosen in the range $0 < \theta < \pi/4$.

The wavefunction $|\Phi(x)>$ of the neutrino can now be expanded in this basis in terms of the plane-wave solutions of the Dirac equation. For simplicity the spinor terms are dropped and so

$$|\Phi(x)> = \alpha\ |\nu_1>\ e^{-ip_1\cdot x} + \beta\ |\nu_2>\ e^{-ip_2\cdot x}\ , \tag{1.10}$$

where $\hbar = c = 1$, α and β are constants, and p_1, p_2 are the four-momenta for neutrinos in the states $|\nu_1>$ and $|\nu_2>$ respectively. Since the neutrino was created in an electron-neutrino state

[4]The Kamiokande II detector has a small neutral-current sensitivity, but the signals are indistinguishable from charged-current elastic scattering.

by a weak interaction, the boundary condition $|\Phi(x)> = |\nu_e>$ must apply at $x = t = 0$, and so $\alpha = \cos\theta$, $\beta = \sin\theta$. At some later time the probability of this neutrino having oscillated to another flavor state is given by the overlap

$$\text{Probability } \nu_e \rightarrow \nu_\mu \;=\; |<\nu_\mu|\Phi(x)>|^2 \;=\; \sin^2 2\theta \, \sin^2\left[\frac{(p_1 - p_2)\cdot x}{2}\right] . \qquad (1.11)$$

For neutrinos with total energy E much greater than their rest mass energy the energy momentum relation becomes $E - pc \simeq m^2c^4/E$. Hence the phase in the square bracket becomes $\Delta m^2 Lc^3/4\hbar E$, where L is the earth-sun distance and $\Delta m^2 = |\, m_1^2 - m_2^2 \,|$ is the difference between the squares of the masses of the plane-wave mass eigenstates.

The long baseline given by the distance $L \simeq 1.5 \times 10^{11}$ metres means that solar neutrino 'flavor interferometry' can probe very small neutrino masses. For a 1 MeV solar neutrino the phase at the earth becomes unity for $\Delta m^2 = 5.3 \times 10^{-12}$ (eV)^2. For Δm^2 much less than this value the phase is small and there is too small a probability of oscillation. For Δm^2 much larger than this value the phase will oscillate rapidly with neutrino energy and so experiments would record that a fraction $0.5 \sin^2 2\theta$ of the neutrinos would change flavor. The mixing angles required to solve the solar neutrino problem by this means are quite large, certainly greater than those encountered in the quark sector, and this solution is not favoured by current theoretical prejudice.

If Δm^2 happens to lie in the range 2×10^{-12} eV$^2 < \Delta m^2 < 4 \times 10^{-10}$ eV^2 then the fraction of neutrinos changing flavor can exceed $0.5 \sin^2 2\theta$ for some solar neutrino energies. Thus significant distortions of neutrino energy spectra would be generated. There is not yet enough evidence from the Kamiokande II experiment to deduce the ^{8}B neutrino energy spectrum with sufficient confidence to test this possibility. However, it is widely believed that such an unnatural choice of mixing angle (too large) and Δm^2 (too tightly constrained) makes it unlikely that the solar neutrino problem can be solved by such fine-tuning.

1.3.2 Matter enhanced oscillations

The presence of matter can alter the rate of propagation of any particle through a dense medium by means of the coherent scattering of the particle with the scattering targets in the medium. Assuming only conservation of probability, the optical theorem relates the total cross-section of the scattering process to the imaginary part of the scattering amplitude $f(p,\theta)$ in the forward direction $\theta = 0$. The most simple example is the refractive index in classical electrodynamics, where the refractive index of photons can be calculated from the polarizability of atoms in the medium, see Jackson [35]. The refractive index n for a photon of momentum p is then

$$n(p) \;=\; 1 + \frac{2\pi N}{p^2} f(p,0) \,, \qquad (1.12)$$

Case	Condition	Transition probability
Low density	$l_\nu \ll l_e$	$\sin^2 2\theta_\nu \sin^2(\pi r/l_\nu)$
Resonant density	$l_\nu/l_e = \cos 2\theta_\nu$	$\sin^2[(\pi r \sin 2\theta_\nu)/l_\nu]$
High density	$l_\nu \gg l_e$	$(l_e/l_\nu)^2 \sin^2 2\theta_\nu \sin^2(\pi r/l_e)$

Table 1.5: Neutrino flavor transition probabilities after a distance r.

where N is the number of scattering centres per unit volume.

The reduction of the phase velocity of a particle by virtue of its coherent scattering with scattering centres is a very general concept and applies just as much to (massive or massless) neutrinos as photons. Now since the weak interaction strength is much less than in electrodynamics, the forward scattering amplitude for neutrinos is much less than that for photons in a dense medium, and the phase velocity of neutrinos (in a medium with a density such as that in the sun or earth) is very close to (but larger than) that in a vacuum. The phase of the weak eigenfunctions contains an additional refractive index factor which, in principle, is different for the two eigenstates.

The general forward scattering amplitude for neutrinos in matter is complicated by the scattering off nuclei, and to compute this would require knowledge of the number densities of all nuclei present. However if one restricts the question to the *difference* between the forward scattering amplitude of electron and muon neutrinos then the treatment can be simplified to the consideration of just one process. In 1978 Wolfenstein [36] pointed out that the forward scattering amplitude for electron neutrinos is greater than that for muon neutrinos in matter because the former can also scatter electrons by a charged-current interaction (exchange of the W boson). He noted that this meant that the phases of the weak eigenstates would therefore oscillate at different rates because of the different 'refractive indices' of the different neutrino flavors. Returning to the analogy of the K^0, $\bar{K}^0$ system, neutrino flavor oscillations in matter are analogous to the K^0 regeneration phenomenon[5]. Note that Equation (1.10) must be transformed into the flavor basis before changing the phase velocity, because the Wolfenstein mechanism is flavor dependent and is not selective of the mass eigenstates.

Wolfenstein [36] showed that the interaction Hamiltonian is $\sqrt{2}GN_e$ for electron neutrinos only, where G is the Fermi coupling constant and N_e is the electron number density. This interaction changes the effective mixing angle to the 'matter mixing angle' θ_m which is a

[5]Note that symmetry breaking mechanism in the K^0, $\bar{K}^0$ system (causing regeneration) is a different mechanism than the Wolfenstein neutrino flavor oscillations. The $\bar{K}^0$ has more interactions available as it can undergo strangeness changing interactions giving hyperons in the final state.

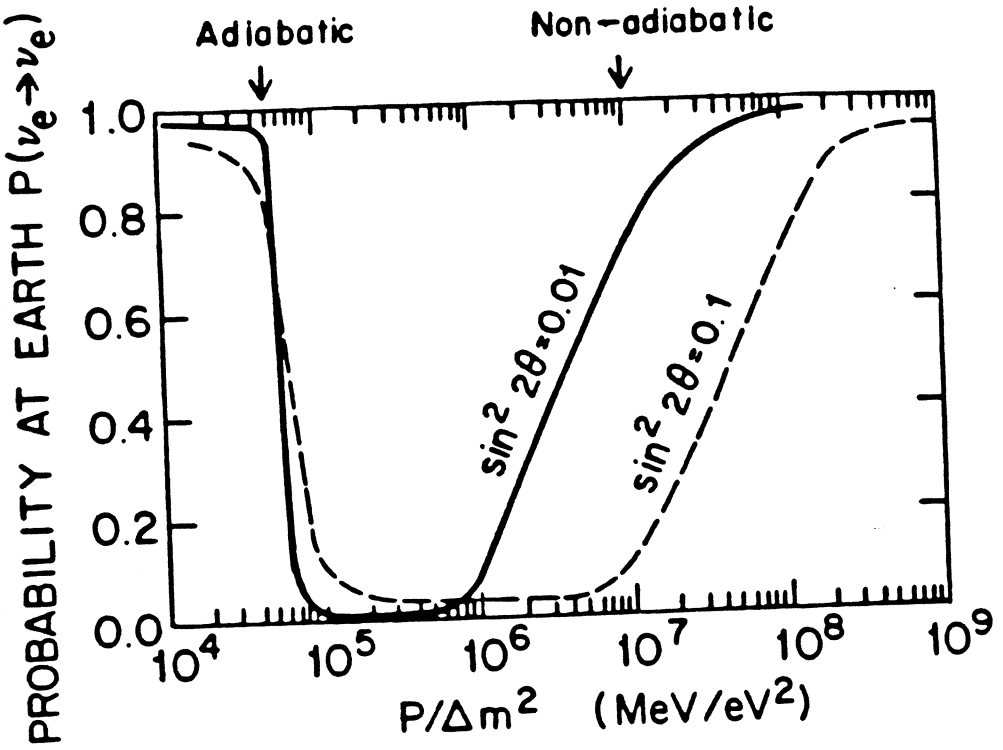

Figure 1.8: The probability of flavor oscillation for neutrinos created in the solar core as a function of momentum $p/\Delta m^2$.

function of the electron density. The computation is straightforward but rather tedious, and is performed in Appendix A for the case of constant electron number density. The key feature is that for a certain electron density, the mixing becomes resonant and $\sin^2 2\theta_m \rightarrow 1$. Expressed in terms of the vacuum oscillation length $l_v = 2\pi / |E_1 - E_2|$ and neutrino-electron interaction length $l_m = 2\pi\hbar c/\sqrt{2}GN_e$, the transition probabilities are shown in Table 1.5.

The more general case of the varying electron density was developed by Mikheyev and Smirnov [37]. They demonstrated that if the neutrinos of energy E were created in a region of electron density greater than the resonant density

$$\text{At resonance} \quad N_e = \frac{\Delta m^2 \cos 2\theta_v}{2\sqrt{2}GE}, \tag{1.13}$$

then as they propagated out of the sun, they would pass through a region of resonant density. Depending on the neutrino energy, mass, and local electron density, several characteristic types of flavor oscillation can occur:

1. If the density is changing slowly enough the *adiabatic condition* is satisfied:

$$\frac{E}{\Delta m^2 c^4} < \frac{N_e}{\hbar c}\left[\frac{\partial N_e}{\partial r}\right]^{-1} \sin 2\theta_v \tan 2\theta_v , \tag{1.14}$$

   and flavor oscillations will be maximal.

2. If expression (1.14) becomes an equality, then flavor mixing does not have chance to become resonant and the oscillation probability is reduced. In this *non-adiabatic* regime

this oscillation probability becomes quite energy dependent, and so neutrino energy spectra would become distorted.

The probability of flavor oscillation by the Mikheyev-Smirnov-Wolfenstein (MSW) effect is shown in Figure 1.8. The results of various solar neutrino experiments are often interpreted in terms of the exclusion of various regions in the ($\sin^2 2\theta$, Δm^2) plane. For large vacuum mixing angles, the inequality (1.14) is satisfied for wide energy ranges; for solar neutrinos in the energy range $\sim$ 0.1 to 10 MeV the value of Δm^2 required is of order $10^{-7} \rightarrow 10^{-5}$ $(\mathrm{eV})^2$. This neutrino mass is considered to be theoretically plausible by many authors; see for example reference [38]. Notice also the dependance on energy (momentum) in the non-adiabatic regime. This distortion of the neutrino energy spectra would provide an experimental means of discovering the neutrino oscillations without reference to the standard solar model. The capability to detect ν_μ and ν_τ neutrino flavors would also confirm the existence of flavor oscillations as these are not created in the sun.

1.3.3 Magnetic effects

There has been speculation that neutrinos generated in the core of the sun may be undergoing a transition through an interaction of the solar magnetic field with a hypothetical neutrino magnetic moment [40]. In the case of a Dirac neutrino this would cause a transition to a right-handed neutrino, which is non-interacting in the standard electroweak model, and hence it would not be registered in terrestrial experiments. In the case of a Majorana neutrino the transition would change the flavor of the neutrino. To ensure significant transition probability, the value of the neutrino magnetic moment would have to be of order $10^{-12}\,\mu_B$. This value is surprisingly large in the context of the standard model. Invoking a neutrino mass $m_{\nu e}$, the standard model prediction from charged-current Feynman graphs leads to a predicted moment of order $10^{-19}\,(m_{\nu e}/\mathrm{eV})\,\mu_B$, tiny compared to the required magnetic moment. Clearly a minor extension to massive neutrinos in the standard electroweak model is not sufficient.

Interest in such theories was initiated by the suggestion that the rate of production of ^{37}Ar atoms in the Chlorine experiment is correlated with the sunspot cycle. Presumably the causal mechanism is the induced variation of the solar magnetic field. Changes in the outer convective zone/photosphere do not directly affect the core material where the neutrinos are generated; such changes are the solar equivalent of weather or climate changes. Bahcall and Press [39] have made a systematic survey of the statistical significance of the sunspot number correlation to the Chlorine data shown in Figure 1.3. They conclude that there is no evidence (Null hypothesis accepted) for any correlation for the first half of the data set, but they claim that the data support a correlation for the second half of the data sample. The Kamiokande II collaboration has examined their data for correlations with the sunspot number and has found

no such effects [29, 30]. Clearly this question will require more experimental investigation before a definitive answer emerges.

1.4 Prospects for new experimental results

The field of solar neutrino physics is about 30 years old but in many ways is not yet fully mature. The number and variety of solar neutrino detection experiments will increase significantly in the future. In particular, sensitivity to lower energies, higher count rates and energy resolution, and sensitivity to neutral-current processes are required. On the horizon there are new detector technologies, such as cryogenic detectors, ^{115}In neutrino absorbtion, and coherent scattering detectors which could provide novel techniques to count solar neutrinos in real time. (See Bahcall [1] for a review.) In this section the more immediate prospects for measurement of the solar neutrino flux are discussed[6].

Currently two of the existing four neutrino detectors, namely SAGE and Gallex, are taking data and this process will continue for several years to establish better statistical accuracy. Hopefully a consensus will emerge between these experiments to determine the capture rate of solar neutrinos on ^{71}Ga. Continued extractions for several years should provide some test of the stability of the signal from the gallium experiments. Calibration of both experiments is planned in 1993 with a ^{51}Cr neutrino source.

The other two solar neutrino detectors, the Chlorine and Kamiokande II experiments, are changing their configurations. The Chlorine experiment is about to be converted to an Iodine experiment which can detect solar neutrinos via the reaction $^{127}\mathrm{I} + \nu_e \rightarrow {}^{127}\mathrm{Xe} + e^-$. This has similar chemical extraction properties to the Chlorine experiment, but provides an enhanced cross-section for reactions with the ^{7}Be neutrinos. The Kamiokande II detector has recently had some minor repairs, replacements of broken photomultipliers, and further measures have been taken to suppress radioactive backgrounds. The detector, now known as Kamiokande III, is taking solar neutrino data again.

Work has started on the construction of a substantially larger version of the Kamiokande detector, called SuperKamiokande, which will contain 50,000 tonnes of high purity water as a solar neutrino target, in addition to the search for proton decay. For solar neutrino detection, the background suppression will require that a fiducial mass of about 22,000 tonnes of water forms the active target. The Čerenkov radiation from neutrino electron scattering

[6]The ICARUS collaboration has presented an imaginative proposal for a liquid argon time projection chamber (TPC) which would provide an electronic 3-dimensional image of charged particle tracks together with good energy resolution [42]. The detector volume is divided into two wire chambers each with 3600 vertical wires and 4800 horizontal wires; the drift time to each wire gives information of the position of an ionization track. The charge collected by each wire gives an estimate of the energy deposited (locally), and the total energy resolution has been estimated at about 3% for few MeV electrons and γ-rays. The detector has been suggested as a target for solar neutrinos.

events will be detected by about 12,500 Hamamatsu R1449 photomultipliers with improved time resolution. The energy threshold of SuperKamiokande will be reduced from that in the Kamiokande II detector by the reduction of internal and external radioactivity, better vertex resolution, and better water purity. If the electron energy threshold can be reduced to 5 MeV, SuperKamiokande will record about 8,400 elastic scattering events per year. The detector will provide an improved measurement of the solar neutrino energy spectrum and any possible time dependence.

The Borexino collaboration, consisting of scientists from Europe and the U.S.A., have proposed the construction of a neutrino detector using 300 tonnes of a boron-loaded liquid scintillator as a target [41]. With a fiducial volume of about 100 tonnes the detector would record about 15,000 events a year from the ^{7}Be neutrinos and just over 130 events per year from the ^{8}B neutrinos, assuming the standard solar model neutrino fluxes. The very low energy threshold (about 250 keV) required to enable the detection of the ^{7}Be neutrinos means that radioactive contamination will have to kept to exceptionally low levels. Unlike Čerenkov detectors, Borexino is sensitive to the alpha particle decays from natural radioactivity, and so elements such as ^{232}Th must be reduced to one part in 10^{16}.

A heavy water Čerenkov detector, known as the Sudbury Neutrino Observatory (SNO), is currently under construction in Canada, and is expected to be completed in 1995. The use of heavy water as a solar neutrino target medium will provide an extra charged-current and an extra neutral-current reaction, and the reaction rates will thereby by increased by a factor of more than an order of magnitude over the Kamiokande II detector. The Sudbury Neutrino Collaboration aims to resolve the question of neutrino flavor oscillations by observing the total neutrino flux by a neutral-current interaction and comparing this to the flux observed from the charged-current reaction channels. The motivation for the construction of the detector is described in the SNO proposal document [43], and the details of the actual implementation are described in the following chapter. Work for the optimisation and calibration of the detection forms the background for the work in this thesis.

Chapter 2

The Sudbury Neutrino Observatory

The Sudbury Neutrino Observatory aims to resolve the solar neutrino problem by performing a real-time high-statistics measurement of the flux of neutrinos from the sun by detecting the Čerenkov radiation generated from neutrino interactions in 1000 tonnes of high purity D_2O. The D_2O is held in an acrylic vessel of 6 m radius which is surrounded by about 7000 tonnes of light water to act as shielding. The Čerenkov radiation is detected by an array of photomultipliers which surround the D_2O. To shield it from cosmic rays, the detector is located at a depth of 2070 m in a nickel mine near Sudbury, Ontario in Canada.

A unique feature of the SNO detector is that by using D_2O both charged-current and neutral-current neutrino interactions can be measured. The detection of the neutrons produced in the neutral-current interaction means that the total flavor-independent neutrino flux can be measured, and by comparing this flux with that from electron neutrinos only, any neutrino flavor-changing will be measured. Furthermore since SNO can measure the total flux of ^8B neutrinos from the sun this information can then be used to constrain the standard solar model, to the extent that the low energy cross-section of the reaction $^7Be + p \rightarrow {}^8B + \gamma$ is known.

The event rate of neutrino interactions in the SNO detector will be significantly larger than that in the other existing water Čerenkov detector to report the solar neutrino flux, Kamiokande II. This is due to two factors. Firstly the radioactive contamination of the materials used in the SNO detector will be significantly lower than in the Kamiokande II detector. This means that the threshold for observing neutrino interactions will be lower in the SNO detector (about 5 MeV) than in the Kamiokande II detector (7.5 MeV), and hence more of the neutrino energy spectrum can be measured in SNO. Secondly the neutrino interaction cross-sections in heavy water are about an order of magnitude larger than that of the $e^- + \nu_e \rightarrow e^- + \nu_e$ scattering used by Kamiokande II. This increased rate means that the energy spectrum of the ^8B neutrino flux will be measured accurately. By looking for distortions of the spectrum it should possible to search for the effects of neutrino flavor oscillations.

If the MSW effect is the explanation of the solar neutrino problem this technique should be particularly sensitive if the value of Δm^2 happens to be towards the lower end of the currently expected range 10^{-7} eV^2 $< \Delta m^2 <$ 10^{-4} eV^2. In this non-adiabatic oscillation case the distortion of the shape of the ^{8}B neutrino energy spectrum is quite dependent on the vacuum mixing angle. These two techniques for probing the neutrino flavor oscillations, although not totally decoupled, may provide a consistency check if flavor changing is found to occur.

2.1 Neutrino interactions

The SNO detector is sensitive to neutrinos via three interactions which are summarized in Table 2.1 and their cross-sections are plotted in Figure 2.1 as a function of neutrino energy. The angular distributions shown in Table 2.1 refer to the initial direction of the electron with respect to the incident neutrino. Reaction I, dubbed 'inverse beta decay of the deuteron', has only a non-vanishing Gamow-Teller matrix element and so the angular distribution [44] is given by

$$I(\theta) = 1 - \frac{1}{3}\left(\frac{v}{c}\right)\cos\theta \simeq 1 - \frac{1}{3}\cos\theta\,, \tag{2.1}$$

where v is the initial velocity of the final state electron and θ is the angle between the initial direction of the electron and the neutrino[1]. The reaction has good energy resolution as the initial energy of the electron has the energy of the neutrino minus the Q value of 1.44 MeV. The cross-section for reaction I has been computed by Kubodera *et al.* [45, 46] and Ying *et al.* [47].

The elastic scattering (ES) reaction II, as used in Kamiokande II, provides an unambiguous signature of solar neutrino detection as the initial direction of the electron is sharply peaked in the direction away from the sun. There is no threshold to this reaction but just as in the Compton effect there is a kinematic constraint on the initial direction θ of the scattered electron with respect to the incident neutrino. For an initial electron of kinetic energy E_e the angle θ is of order $\sqrt{m_e c^2/E_e}$ radians provided that $E_e > m_e c^2$. This should not be confused with the subsequent multiple scattering of the electron in the D_2O. The cross-section for $e^- + \nu$ scattering has been calculated by t' Hooft [48] who reports the differential form

$$\frac{d\sigma}{dE_e} = \frac{2G^2 m_e}{\pi}\left[(g_A + g_V)^2 + (g_A - g_V)^2\left(1 - \frac{E_e}{E_\nu}\right)^2 + (g_A^2 - g_V^2)\frac{m_e E_e}{E_\nu^2}\right]\,, \tag{2.2}$$

where G is the Fermi coupling constant expressed as $1.02 \times 10^{-5} m_p^{-2}$ using natural units $\hbar = c = 1$, and E_ν is the incident neutrino energy. The factor before the square bracket is numerically equal to 1.72×10^{-44} cm^2 MeV^{-1}. The Weinberg model of the electroweak

[1] It should be born in mind that the SNO detector has its own intrinsic resolution of the initial direction and energy of the electron. Thus the distribution of primary electron energies and directions will be degraded when the distribution is measured in the SNO detector

	Reaction	Type	Q-value	σ at 10 MeV	Angular distribution
I	$d + \nu_e \rightarrow p + p + e^-$	CC	-1.44 MeV	2.7×10^{-42} cm^2	$I(\theta) = 1 - \frac{1}{3}\cos\theta$
II	$e^- + \nu \rightarrow e^- + \nu$	ES	zero	9.2×10^{-44} cm^2	forward peaked
III	$\nu + d \rightarrow \nu + p + n$	NC	-2.22 MeV	1.1×10^{-42} cm^2	none - neutron detected
IV	$\bar{\nu}_e + d \rightarrow n + n + e^+$	CC	-4.03 MeV	1.2×10^{-42} cm^2	$I(\theta) = 1 - \frac{1}{3}\cos\theta$
V	$\bar{\nu}_e + p \rightarrow n + e^+$	CC	-1.80 MeV	5×10^{-42} cm^2	almost isotropic

Table 2.1: Neutrino interactions in the SNO detector.

interaction [49] predicts that

$$g_V - g_A = \sin^2\theta_W \quad \text{and} \quad g_A = \begin{cases} +1/4 & \text{for } e^- + \nu_e \rightarrow e^- + \nu_e \\ -1/4 & \text{for } e^- + \nu_\mu \rightarrow e^- + \nu_\mu \end{cases} \tag{2.3}$$

and the Weinberg angle θ_W has been experimentally determined to be $\sin^2\theta_W = 0.226$. The scattering of ν_e is larger than other flavors as the latter can only proceed via Z^0 exchange whereas the former can also exchange a W boson. The total cross-sections plotted in Figure 2.1 are the t' Hooft differential cross-sections integrated over final state electron energy. The cross-section of reaction II quoted in Table 2.1 is for $\nu_e + e^-$ scattering. Reaction II has a rather smaller cross-section than other reactions in SNO, but this is compensated for by the fact that there are 5 times as many electrons as deuterium nuclei in the D_2O molecule.

The use of D_2O as a target medium gives the SNO detector the unique capability to detect solar neutrinos (above the deuteron binding energy of 2.2 MeV) via a neutral-current (NC) interaction III. This capability enables SNO to measure the total neutrino flux. Using the observed ν_e flux from reaction I, SNO should be able to determine the fraction of solar neutrinos which have changed flavor between their creation in the sun and their observation in the SNO detector. It should be noted that this capability does not require any solar model at all. Reaction III has good energy resolution but any realistic method of detecting the final state neutron must involve its thermalisation and therefore all information about its initial direction and energy is lost. The cross-section for reaction III has also been computed by Kubodera *et al.* [45, 46, 50] and Ying *et al.* [47]. Progress has been made recently in refining these computations and the cross-section is now believed to be known within a few percent accuracy in the energy range relevant to solar neutrinos [46].

The SNO detector is sensitive to antineutrinos via reactions IV and V. Reaction IV is the analogue of reaction I with antineutrinos, whilst reaction V (the inverse of the beta decay

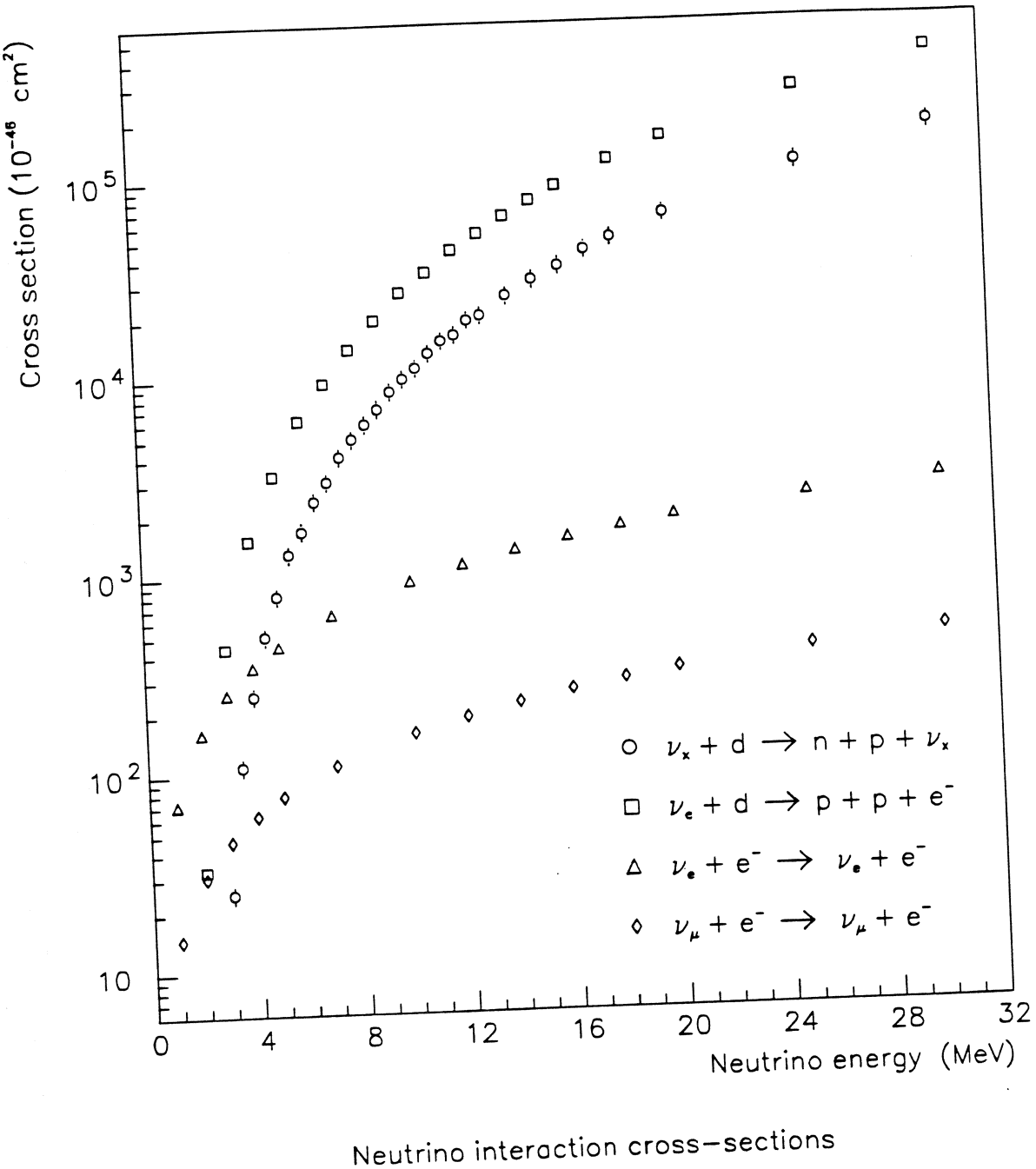

Figure 2.1: The neutrino interaction cross-sections for the energy range appropriate to solar neutrinos. Data for the neutral-current and charged-current interactions are taken from Kubodera *et al.*, see text for references.

	Reaction	SSM		Vacuum	MSW effect	
		full	× 1/3	mixing	adiabatic	non-adiabatic
I	$d + \nu_e \rightarrow p + p + e^-$	9750	3255	3260	3750	3750
II	$e^- + \nu \rightarrow e^- + \nu$	1100	360	480	645	488
III	$\nu + d \rightarrow \nu + p + n$	2800	933	2800	2800	2800

Table 2.2: Neutrino interaction rates in the SNO detector per kt-year.

of the neutron) can be detected in the light water part of the detector only. Sensitivity to antineutrinos is not considered to be important for solar neutrino physics, but is important in observations of the antineutrinos emitted during the cooling phase of a supernova [51].

Although the SNO detector is primarily designed to solve the solar neutrino problem, its sensitivity to ν_μ and ν_τ neutrinos from a supernova could be useful for identifying their mass. For example if the tau neutrino had a rest mass[2] of 30 eV and was emitted with 15 MeV from a supernova at 10 kpc from the earth, its time of flight to the earth would be about 2 seconds longer than that of an electron neutrino. This is due to the difference of the velocities of the two neutrino types. Hence the burst-phase pulse of neutrinos from the supernova would be resolved as two distinct pulses in the SNO detector. By this means SNO would be sensitive to the ν_τ mass provided that neutral-current and charged-current events can be distinguished.

Given that the cross-sections of the neutrino interactions are known and there will be about 1000 tonnes (1 kt) of D_2O in the SNO detector the expected interaction rate of solar neutrinos can be calculated. The SNO proposal [43] lists the expected interaction rate for the standard solar model neutrino flux given a plausible efficiency for detecting neutrons. As discussed below the scheme detects 8.6 MeV γ-rays produced from radiative neutron capture on ^{35}Cl, present in the form of NaCl dissolved in the heavy water. The rates shown in the SNO proposal document are reproduced in Table 2.2 assuming 100% detection efficiency and a electron energy threshold of 5 MeV. The interaction rates in the case of vacuum neutrino flavor mixing and the MSW effect are shown in the assumption that the standard solar model predicts the rate of creation of solar neutrinos. The adiabatic MSW case is calculated for a neutrino cut off energy of 9 MeV below which neutrinos are not converted. In Table 2.3 the expected number of events recorded in the SNO detector from a supernova at 10 kpc is shown; the data are taken from Burrows *et al.* [52] and assume 100% detection efficiency.

[2]This tau neutrino mass would be enough to make the universe 'flat', i.e. have the critical density defining the boundary between an open and closed universe.

	Reaction	Target medium	Neutrino events ν_e burst phase	cooling phase
I	$d + \nu_e \rightarrow p + p + e^-$	D_2O	10	82
II	$e^- + \nu \rightarrow e^- + \nu$	D_2O / H_2O	1	22
III	$\nu + d \rightarrow \nu + p + n$	D_2O	6	272
IV	$\bar{\nu}_e + d \rightarrow n + n + e^+$	D_2O	0	67
V	$\bar{\nu}_e + p \rightarrow n + e^+$	H_2O	0	330

Table 2.3: Number of events per kt or target in the SNO detector from a supernova at 10 kpc.

2.2 The SNO detector

The detector itself is sited in the norite[3] rock part of the Creighton nickel mine of INCO Ltd, located in the town of Walden, about 25 km west of Sudbury. The SNO cavity is to be barrel shaped, being at least 21.4 m in diameter at the widest point and about 30 m high including the electronics area above the main detector. An outline of the SNO detector is shown in Figure 2.2 although the latest revision of the design now has the electronics mounted on the deck on top of the cavity. The cavity site is in an area of the mine which is currently active and will remain so for the life of the experiment. The depth of the SNO cavity is 2070 m, and the overburden has the equivalent stopping power of about 6000 m of water. Apart from neutrinos, muons are the only component of the cosmic ray flux which are significant at such depth. The muon flux is small with only about one muon per hour passing through the active detector volume, with only about one muon stopping in the detector per day. As in the Kamiokande detector the muon induced spallation products from ^{16}O (produced by energetic muons) present a significant background problem in addition to the muons themselves, as some spallation products are high energy beta emitters.

The Čerenkov radiation from relativistic electrons (and muons) will be detected using about 9600 photomultipliers mounted on 750 panels. The panels are mounted on a support structure made from struts of 4 inch stainless steel tubing in the shape of a geodesic dome (three-frequency icosahedron) of approximate radius 8.9 m. The 2.5 m of light water between the photomultiplier support structure and the acrylic vessel shield the heavy water from γ-

[3]The so-called 'hanging wall' rock is composed of norite, which was chosen as it has lower thorium and uranium content than the other rock types (gabbro, granite and diorite) in the mine and also for its suitability for the excavation of large cavities.

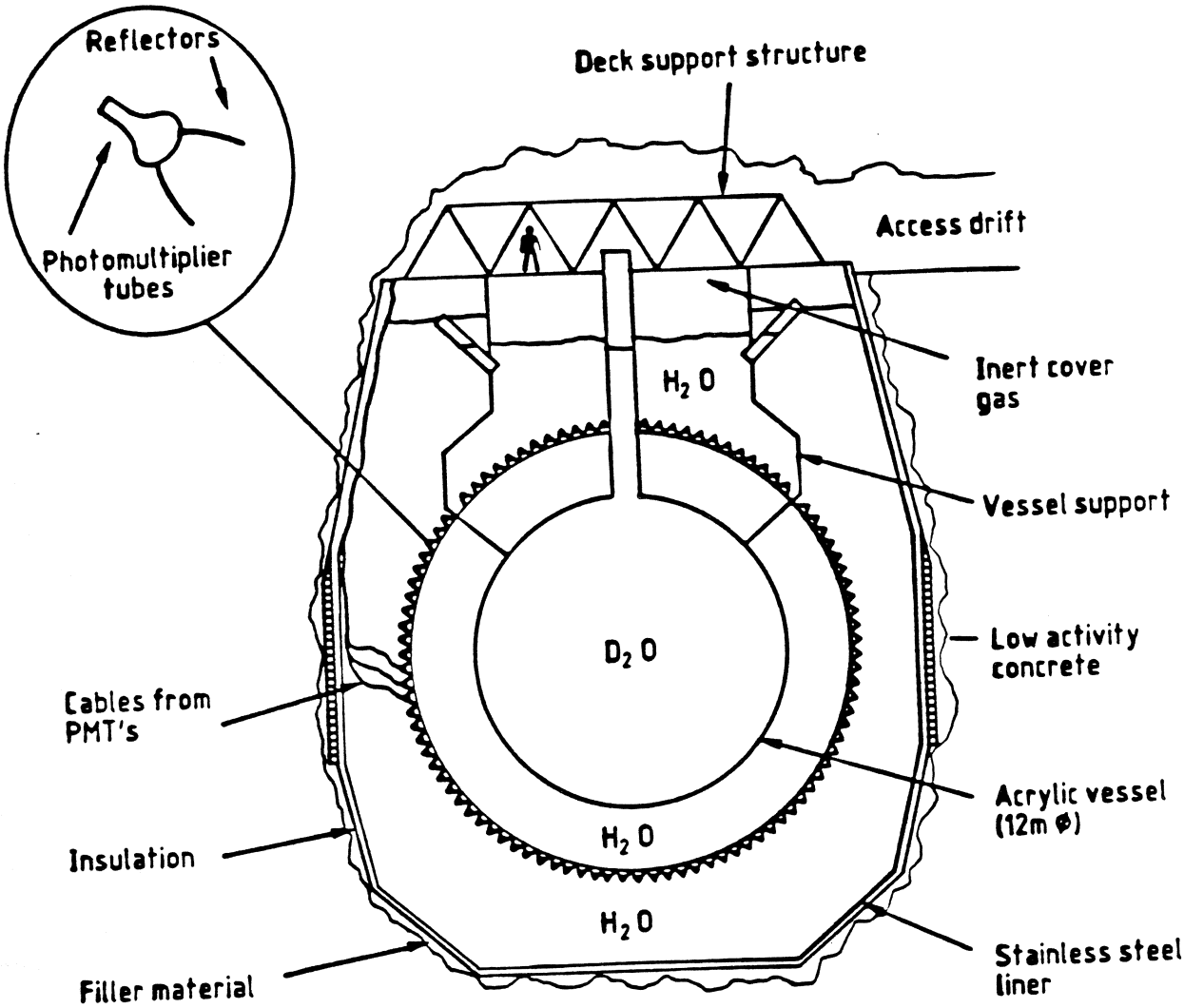

Figure 2.2: Outline of the SNO detector.

rays caused by radioactivity in the photomultipliers. Naturally occurring γ-rays of sufficient energy to mimic a high energy electron (via Čerenkov radiation from Compton scattered electrons) are a source of background, but also any γ-ray of energy greater than 2.2 MeV can cause photodistintegration of the deuteron and hence appear as a neutral-current event. The daughters of ^{238}U and particularly ^{232}Th have high energy γ-ray transitions[4] and so these isotopes must be rigorously excluded from the detector components. The glass bulbs used to manufacture the photomultipliers were made from Schott 8246, a special low radioactivity glass melted especially for the SNO collaboration. They were required to have less than 100 ppb of thorium and uranium. Assay of the samples of this glass has been performed by γ-ray spectroscopy at Birkbeck College and the University of Guelph and the results are summarised in Table 2.4 for batches 2 to 11.

[4]The 2.615 MeV transition in ^{208}Pb and the 2.445 MeV transition in ^{214}Po present the greatest problems.

	^{40}K	^{238}U	^{232}Th
University of Guelph	25.9 ± 5.6	47.6 ± 4.8	19.9 ± 2.5
Birkbeck College	20.3 ± 2.9	38.8 ± 4.6	10.1 ± 1.5

Table 2.4: Concentration of contaminants in Schott 8246 glass in ppb by mass.

The Hamamatsu R1408 photomultipliers have a bialkali photocathode of diameter 200 mm (see Chapter 7) and nine mesh dynodes coated with caesium antimonide. Each photomultiplier will be operated at a voltage which produces a charge gain of 10^7 for single photoelectrons. By virtue of the high voltage between cathode and first dynode, the photomultipliers have low transit time spread ($\sigma < 2$ ns, see Chapter 6) thereby enabling interaction vertices to be reconstructed by timing alone to an accuracy of about 30 cm. The reconstruction accuracy is important for the rejection of background signals, especially outside the D_2O. The photomultipliers are sensitive to magnetic fields and so the SNO cavity is fitted with field coils to cancel the earth's magnetic field in the volume of the cavity; see Chapter 6 for further discussion.

To increase the optical coverage area, reflecting non-imaging concentrators [53, 54] are mounted on the photomultipliers which increase the solid angle subtended by the photomultipliers around the D_2O from 40% to 70% . By using reflectors the number of detected Čerenkov photons is increased by about 65%. These reflectors are designed to accept photons within a cone of half angle 56.4°, so that each photomultiplier cannot see its near neighbours. This 'blinkering' effect greatly reduces the background due to γ-rays generated near the photomultiplier support structure. The cone angle is chosen so that the fiducial volume within a radius of 7 m is visible to all photomultipliers, see Figure 2.3. The reflectors are manufactured from strips of highly polished aluminium used as a substrate for several layers of dielectrics to achieve high durability and reflectivity. The strips are mounted in a plastic holder to ensure they conform to the computed shape. Some tests of a prototype reflector in water have been made by Moorhead [53] and the concentration factor as a function of angle is shown in Figure 2.4.

The electronic systems to record the analogue signals from the photomultipliers will record their size and absolute time. The charge deposited in a photomultiplier signal will be recorded by a dual range Analogue-to-Digital Converter (ADC) which has a range of 0.05 to 1000 photoelectrons. The trigger operation is essentially free from deadtime and the discriminator threshold can be set in the range 0.1 to 0.6 photoelectrons. Whenever the number of channel triggers in 100 ns exceeds a fixed level, called NHit, a global trigger will initiate the acquisition and recording of data. The time resolution of a single channel discriminator is less than 1 ns

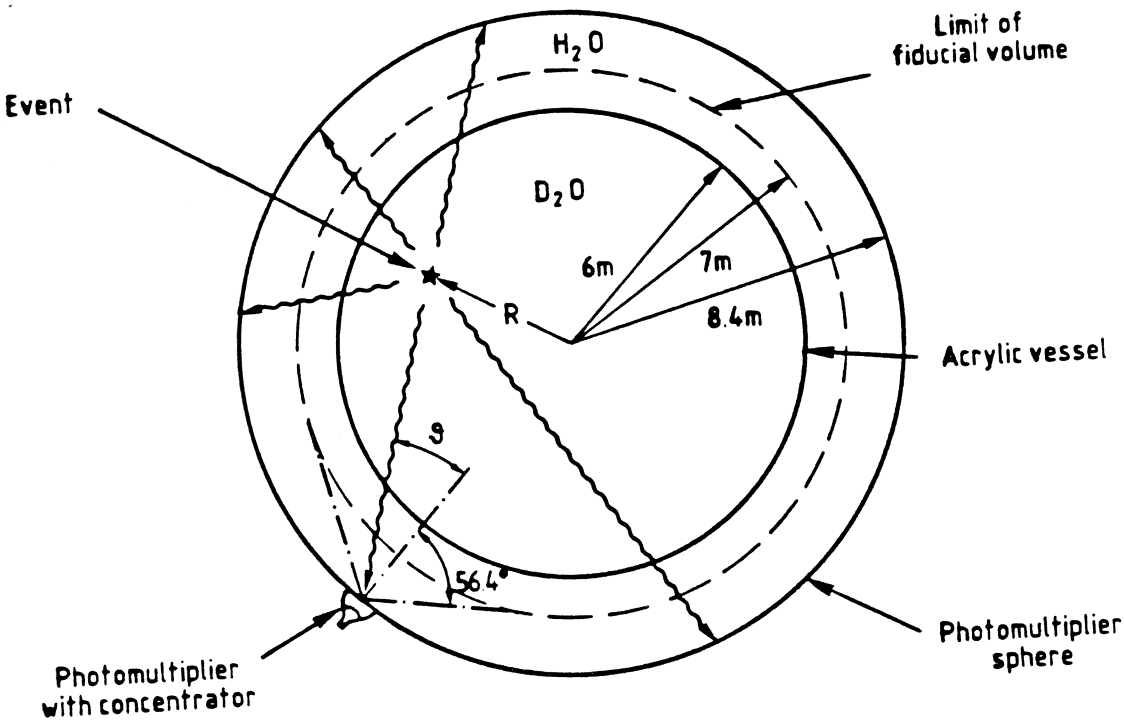

Figure 2.3: The collection of light from the fiducial volume in the SNO detector.

and signals are recorded to the nearest 0.2 ns. The absolute (universal) time is recorded to an accuracy 1 μs to aid the identification of a supernova in conjunction with other detectors. If a supernova were to occur the electronic system would be able to record a burst of at least 10^5 events in one hour.

The detection of free neutrons within the D_2O will be a major contribution to the resolution of the solar neutrino problem as this will measure the total flux of neutrinos from the sun via reaction III. Without another means of detection, neutrons would simply capture on the D_2O liberating a 6.25 MeV γ-ray, of which less than half would exceed the detection threshold equivalent to a 5 MeV electron. Also background rejection is very difficult as there is no direction or energy information to discriminate neutral-current neutrino interactions from other neutron sources. There are currently two options for the detection of neutrons. The default option is to add 2500 kg of pure NaCl to the D_2O and to use the radiative capture reaction $^{35}Cl + n \rightarrow {}^{36}Cl + \gamma$ to produce a γ-ray shower of total energy $\simeq$ 8.6 MeV.

The ^{35}Cl capture cross-section is quite large at 43 b and simulations of the neutron transport [55, Annex 1] show that 83% of neutrons from the neutral-current reaction will capture on either ^{35}Cl or D_2O, whereas only 24% of externally generated neutrons will capture. However the external neutrons should be distinguishable to some extent by virtue of the fact that they capture near the edge of the D_2O. These studies also show that the mean time to capture a

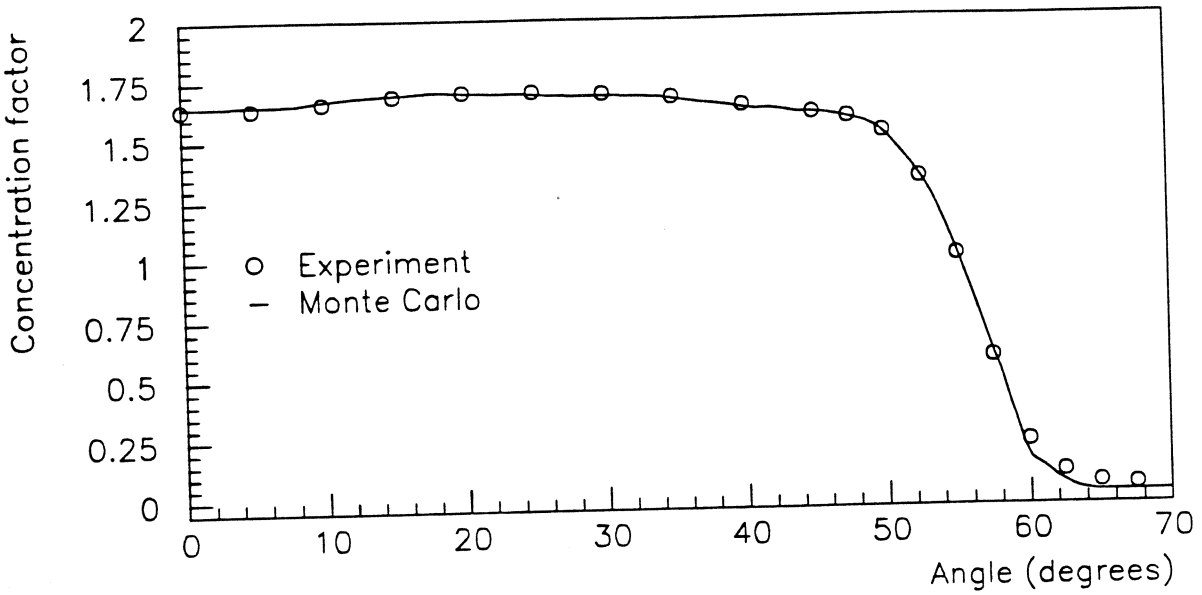

Figure 2.4: Theoretical and measured performance of aluminium reflectors.

neutron in the D_2O is about 5 ms.

The SNO collaboration is also investigating the use of proportional counters (filled with ^3He or ^6Li or Gd) in the D_2O to detect neutrons. This detection method would have the advantage of providing a means of distinguishing neutral from charged-current interactions on an events by event basis. One proposed design [56] is to construct the counters from pure nickel of wall thickness 0.25 mm and outer radius 25 mm, containing ^3He at 3 atmosphere pressure, and a nickel anode wire of diameter 50 μm. The tubes would be 2 m long tethered to form 'strings' with a 112 strings mounted on a 100 cm square lattice in the detector making a total length of 900 m of tubing. Clearly the major problem is making the counters radioactively clean at the level of a few parts in 10^{12}. Some background rejection in the counter is possible by using the pulse height and risetime information. Work is currently underway to simulate the effects of these counters in the detector and measure the properties of prototype counters.

The acrylic vessel containing the D_2O is 12 m in diameter and will be fabricated from about 200 panels of thickness 50 mm. The acrylic used to manufacture the vessel has two important properties. Firstly it has very low levels of thorium and uranium in order to reduce the number of γ-rays showering in the D_2O and hence the neutron background. Secondly the material has very good optical properties, especially ultra-violet transmission, in order to minimize the attenuation of Čerenkov radiation. These two properties are both achieved by keeping the polymethylmethacrylate monomer free from contamination until polymerization. No stabiliser chemicals (which attenuate ultra-violet light) are added. The grade of glassy acrylic suggested for use in the SNO detector has good optical transmission above about 325 nm

for a vessel thickness of 50 mm; see Chapter 4 or Davidson *et al.* [57] for a more extensive account. The (polymerized) acrylic has been assayed using neutron activation analysis and mass spectrometry and the results indicate that acrylic with only 1 ppt of uranium and thorium can be attained. This level of radioactive contamination is satisfactory for the acrylic.

In the D_2O volume of the detector itself the required levels of radioactive purity are even more stringent. The standard solar model predicts 18 neutrons per day produced by the neutral-current interaction and so the rate of neutron production by photodistintegration should ideally be 1 per day or less. Monte Carlo studies predict that this background would be generated by concentrations of ^{232}Th and ^{238}U of 3.7×10^{-15} and 45×10^{-15} respectively by mass. These constraints can be relaxed by about an order of magnitude for the H_2O. The water purification plant will include ion exchange and reverse osmosis stages plus a bed of MnO_2 beads for the removal of radium. Despite being below the Čerenkov threshold tritium can produce optical photons by bremsstrahlung and atomic de-excitation of ^{3}He, see Chapter 3. The D_2O for the SNO detector has been distilled to reduce the tritium loading to below 0.05 μCi Kg^{-1} and the increase in effective noise rate from the remaining tritium is only about 1 count per second in each photomultiplier.

2.3 Detector response and backgrounds

The response of the detector to relativistic electrons from both neutrino interactions and radioactive contaminants has been simulated by Monte Carlo methods [58]. The basis of these simulations is the EGS code system [59] which enables electrons and photons to be tracked through various media. The code is discussed further in Chapter 3, with specific reference to the yield of Čerenkov radiation predicted from the integration along the simulated particle tracks. The results suggest that the number of photomultiplier hits as a function of initial electron energy is linear at about 8 hits per MeV electron energy for an event inside the D_2O. The energy resolution of the detector is dominated by the statistical fluctuations of the number of photomultipliers which detect Čerenkov photons. For a mean of $N(E)$ hits from an electron of initial energy E the Poisson distribution predicts a standard deviation of $N^{1/2}$ hits. Near the predicted electron energy threshold of 5 MeV the resolution should be about 15%.

The initial direction of an electron can be quite well determined from the pattern of Čerenkov photons, but the multiple Coulomb scattering of the electron along its trajectory degrades the (circular) photomultiplier hit pattern. Rayleigh scattering[5] of about 5% of the Čerenkov photons and Fresnel reflection (at the acrylic boundaries) also cause some smearing of the hit pattern. For a 10 MeV electron the initial direction can be reconstructed with

[5]'Rayleigh scattering' is used here to represent any elastic scattering of Čerenkov photons in water. In a liquid the cross-section for elastic scattering by density fluctuations is given by the Einstein-Smoluchowski formula, see Jackson [35]. The mean scattering length is of order 70 m.

a standard deviation of about 27°, although this improves somewhat with increasing initial energy.

An important background rejection feature of SNO is ability to reconstruct the position of the source of the Čerenkov radiation, and hence the interaction vertex. It is proposed to use the relative timing of the photomultiplier hits alone. Rayleigh scattering and Fresnel reflection also limit the accuracy of vertex reconstruction, but photomultiplier noise and transit time spread degrade the resolution further. The precise importance of these factors depends on the details of the fitting algorithm used to deduce the vertex from the times at which the photomultipliers produce a signal. The very simple event fitting algorithm ('fitter') used in the existing Monte Carlo codes suggests that position of events can be reconstructed with standard deviation of 27 cm for an electron of initial energy 10 MeV. It is hoped that a better fitter will reduce this resolution, although a large reduction is very unlikely.

With any fitter there will always be background events which reconstruct within the D_2O volume which could be interpreted as arising from neutrino interactions. As discussed above, the most problematic radioactive backgrounds are from the ^{238}U and ^{232}Th decay series which produce two types of backgrounds for the solar neutrino detection in the SNO detector. Firstly the prompt $\beta - \gamma$ cascades near the ends of these decay series have quite high energies (up to 5 MeV) and given the available energy resolution of the detector some of these will mimic electrons produced from neutrino interactions. The 'internal' $\beta - \gamma$ cascades occur from impurities in the water, acrylic or ropes that support the acrylic vessel. 'External' $\beta - \gamma$ events are those wrongly reconstructed inside the D_2O which actually occurred in the photomultipliers, reflectors, support structure, cables and electronics deck.

High energy γ-rays can also be produced from alpha decay directly via $(\alpha, p\gamma)$ or $(\alpha, n\gamma)$ and indirectly via the radiative capture of the free neutron (n, γ). Thus alpha decays (from isotopes in the ^{238}U and ^{232}Th decay chains) in the surrounding rock or from the photomultiplier support structure region can cause backgrounds. For example the aluminium reflectors are a possible source of the $^{27}Al(\alpha, p)^{30}Si$ reaction which produces a 6.915 MeV γ-ray. Shielding calculations from measurements of the γ-ray flux in the mine [55, Annex 10] suggest that the flux of γ-rays from the rock will be of order 1 per week over 5 MeV in the D_2O. This is comparable with the computed flux from the photomultiplier support structure region. It is hoped that a light water fill of the acrylic sphere will enable a measurement of these backgrounds, although the internal $\beta - \gamma$ rate may be different with H_2O in place of D_2O.

In addition to these backgrounds the neutral-current interaction has to compete with the photodistintegration of the deuteron $\gamma + d \rightarrow p + n$ by any γ-ray whose energy is above the 2.2 MeV threshold. The neutron thereby produced is indistinguishable from one produced in a neutral-current neutrino event. The most significant sources of such γ-rays are from the

Isotope	Series	Total $\beta - \gamma$ energy	Largest γ-ray energy
^{214}Bi	^{238}U chain	3.26 MeV	2.445 MeV (1.5%)
^{208}Tl	^{232}Th chain	5.00 MeV	2.614 MeV (36%)

Table 2.5: Beta decay isotopes with high energy γ-ray decays.

excited states of ^{208}Pb at the end of the ^{232}Th decay series and of ^{214}Po in the ^{238}U decay series. The decay energies are summarised in Table 2.5 in which the third column shows the prompt $\beta - \gamma$ energy in MeV. In fact some ^{214}Bi beta decays go directly to the ground state of ^{214}Po and the electron can produce as much Čerenkov radiation as the 5 MeV $\beta - \gamma$ cascade. The fourth column shows the energy of the highest γ-ray energy with the fraction of decays in the chain which emit this γ-ray shown in parenthesis.

To eliminate these sources of background both the D_2O and H_2O must have as little contamination as possible of the long lived isotopes in both the ^{232}Th and ^{238}U decay series. Targets concentrations of 10^{-15} and 10^{-14} respectively have been set for these isotopes in the D_2O; an extra order of magnitude can be tolerated in the H_2O. In addition to the purification techniques discussed above, assay techniques should be available to determine the concentration of these isotopes in both the D_2O and H_2O. The required concentrations are too low to analyse by mass spectroscopy, although the next generation of Inductively Coupled Plasma Mass Spectroscopy (ICPMS) machines may be able to achieve a sensitivity of 10^{-15} by mass for ^{232}Th and ^{238}U. Work by Sinclair *et al.* [55, Annex 12] has demonstrated techniques to assay water samples to the required level by alpha particle counting of the radon isotopes in the decay chains. In the case of the ^{232}Th chain a short coincidence time of 0.14 seconds between the decay of ^{220}Rn and its daughter ^{216}Po greatly reduces counter backgrounds. In the case of the ^{238}U chain ^{222}Rn is extracted with a helium carrier gas and is then collected in a cold trap. The alpha decays of ^{222}Rn are then counted in a low background Lucas cell (acrylic cell lined with zinc sulphide scintillator). These direct alpha counting techniques do not rely on the assumption that the various isotopes in the decay series are in equilibrium, although the efficiency for extraction and detection of alpha decay isotopes has to be known. From these results the deuteron photodistintegration background can be calculated.

All of these backgrounds are included in the Monte Carlo simulations of the detector response. One of the interesting features of these backgrounds is how they vary with energy. In Figure 2.5 the results of the Monte Carlo simulation of 1 year's data plotted as a function of reconstructed energy for a light water fill of the acrylic vessel. Figure 2.6 shows the equivalent for a heavy water fill and Figure 2.7 shows the effect of adding 2500 kg of NaCl to the heavy

water. All three data sets are for one year of operation. In the figures the labels ES, CC and NC indicate the electron scattering, charged-current and neutral-current events respectively. The 'PMT' and 'cavity' labels indicate high energy γ-rays while the $\beta - \gamma$ backgrounds are labelled by triangles.

2.4 Energy calibration

The energy calibration of the SNO detector is critical for the reliable estimation of the solar neutrino flux and backgrounds. The energy scale cannot be derived by Monte Carlo simulation alone as many detector parameters such as optical transmission and photomultiplier efficiency can only be determined experimentally *in situ*. Experience from other water Čerenkov detectors suggests that there is an overall normalization factor which must be applied to the predicted number of photomultiplier hits to restore agreement with experimental measurements. In a small test detector [43] built by the SNO collaboration a factor of 0.82 of the predicted number of photoelectrons was found for any given event. A comparable figure of about 0.85 was obtained in the Kamiokande II detector. In the IMB detector only 0.53 of the predicted number of hits were recorded from the measurements of through-going muons. The 'lost efficiency' has been attributed to the counting efficiency of single photoelectrons by photomultipliers or some other optical attenuation in the detector. Whatever the explanation, it is clear that *in situ* energy calibration is vital.

As the flux of cosmic ray muons is so low, the detector will be calibrated by a combination of high energy γ-rays sources to be inserted into the aqueous volume; see Chapter 8. As a result of its successful use in SNO photomultiplier calibration experiments (reported in Chapter 5), a compact ^{90}Sr Čerenkov source is proposed to provide an absolute optical calibration of the detector. This would involve measuring the changes in the count rates of the photomultipliers as a function of the position of the ^{90}Sr source. Also several 'routine' monitor sources will be used to monitor the relative optical response of the detector by providing prompt bursts of light which can be reconstructed as single events above the SNO threshold. For example prototype scintillator sources have been constructed and found to have encouraging properties. In this thesis an investigation is made of the likely reliability of the EGS predictions of the yield of Čerenkov radiation upon which the Monte Carlo studies are based. This investigation, see Chapter 3, also helps to establish the credibility of simulations of the yield of Čerenkov radiation from the ^{90}Sr calibration source.

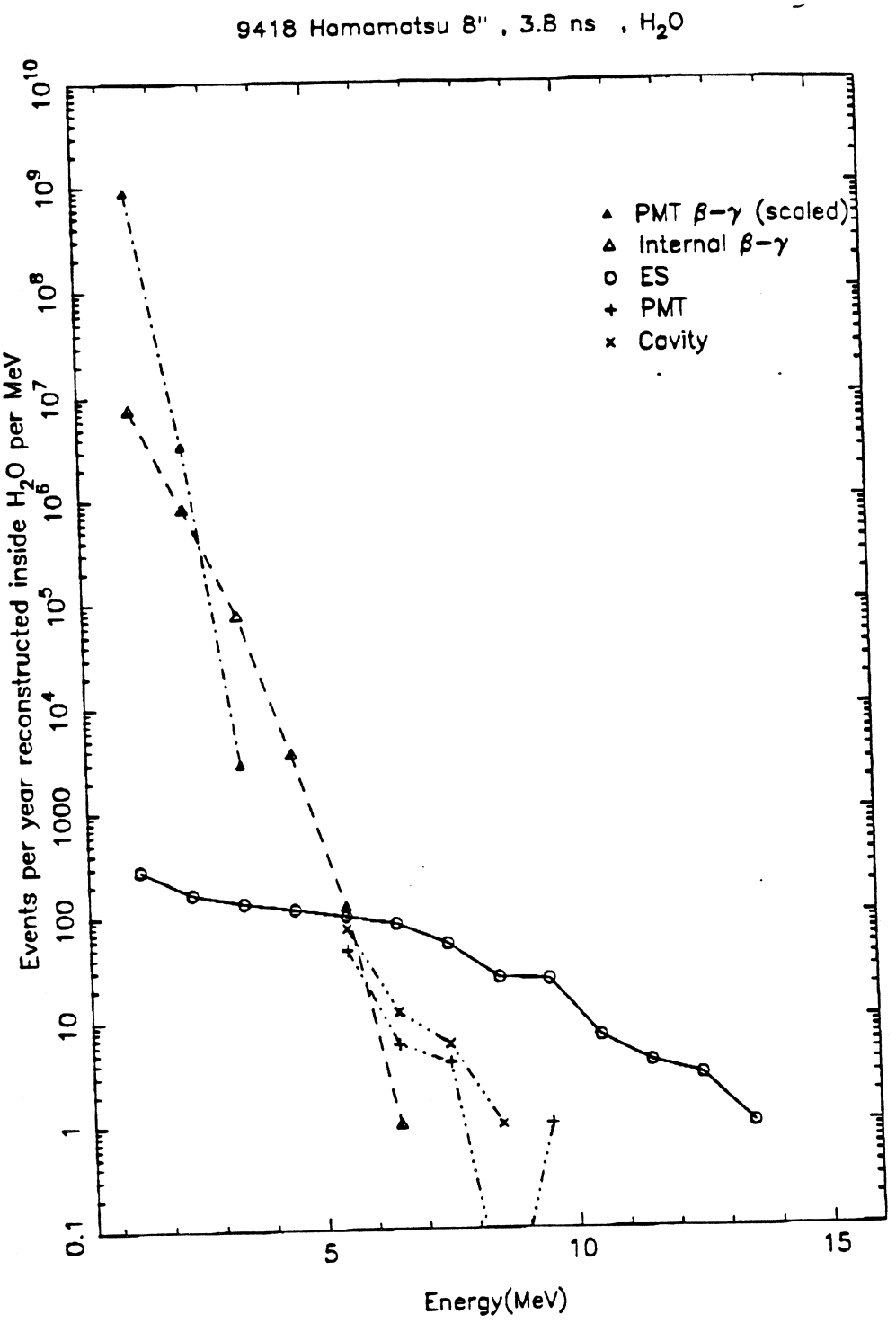

Figure 2.5: Event energy distribution from year of data with H_2O in the acrylic vessel.

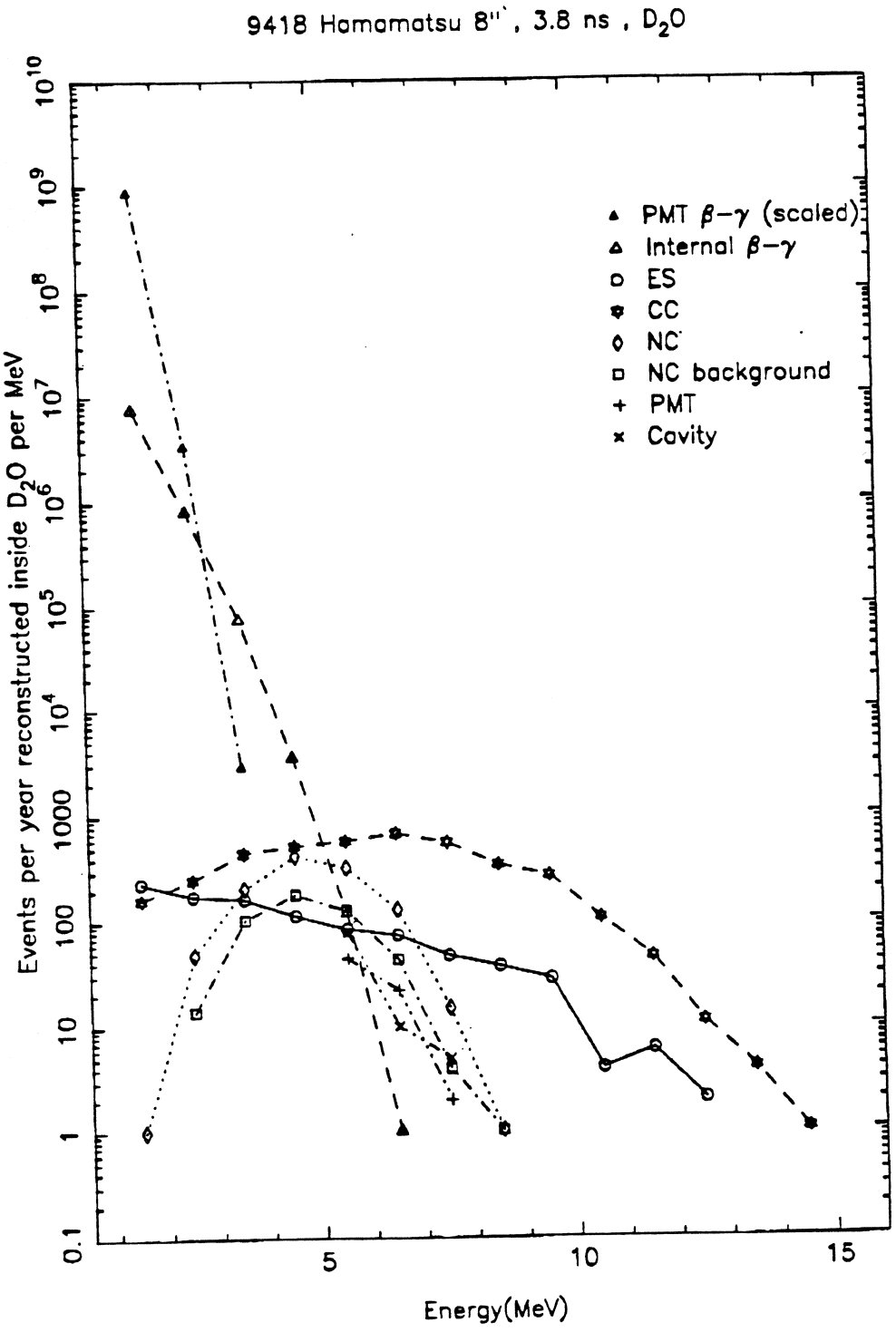

Figure 2.6: Event energy distribution from year of data with D_2O only in the acrylic vessel.

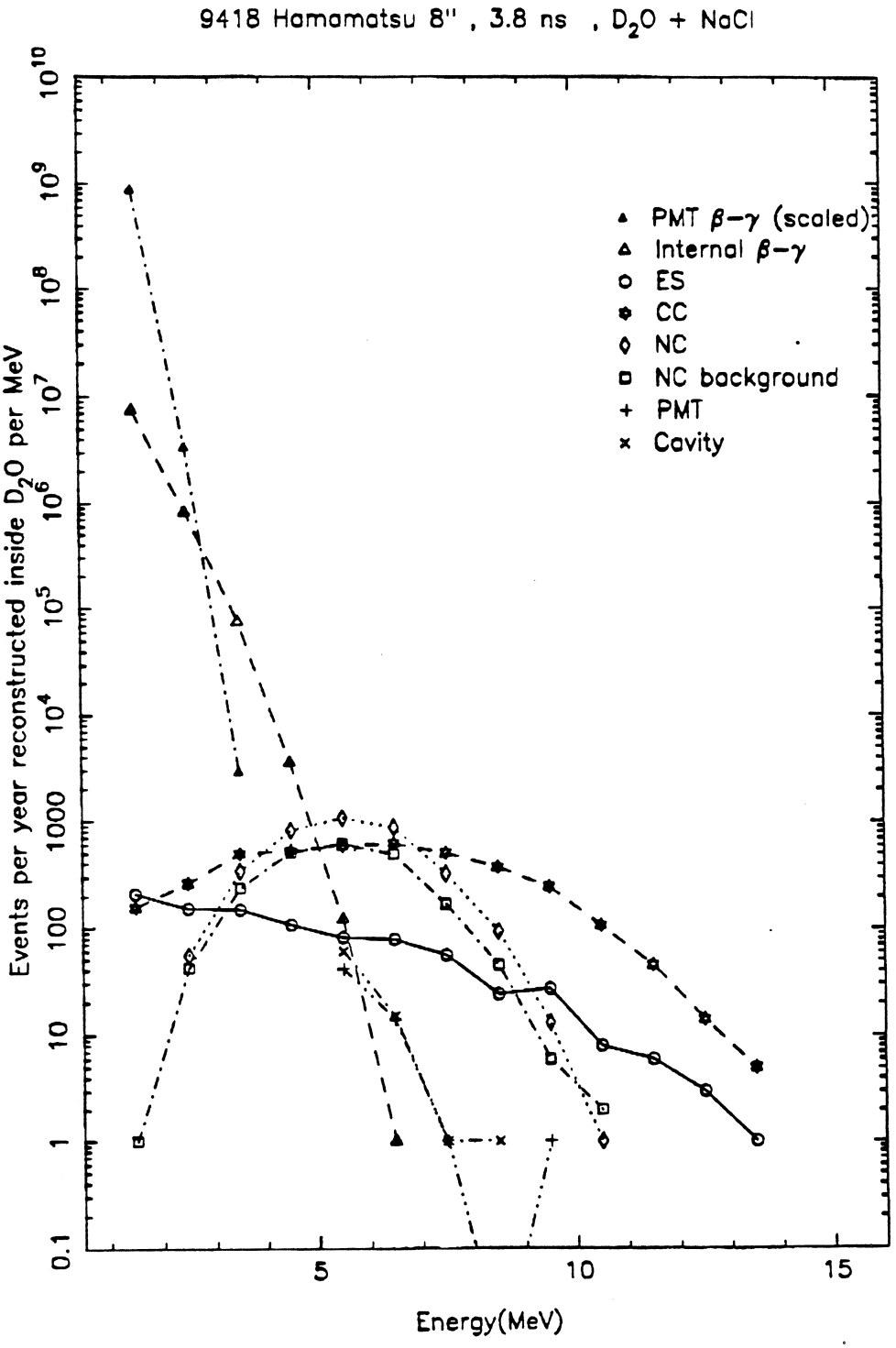

Figure 2.7: Event energy distribution from year of data with D_2O plus 2500 kg of NaCl in the acrylic vessel.

Chapter 3

Čerenkov radiation

When a charged particle travels faster than the phase velocity of light in a transparent medium, a continuous spectrum of photons is generated. This light has become known as Čerenkov radiation, after the detailed reports of the phenomenon by Čerenkov [60] in 1934; for a comprehensive account see Jelley [2] and references therein. The Čerenkov effect has since been subject to both classical and quantum mechanical treatments, but the original classical theory of Frank and Tamm [61], provides a quantitatively accurate description valid under many common circumstances. Moreover their treatment contains most of the important physical principles relevant to the effect, and at optical wavelengths their theory is in agreement with the quantum mechanical results.

From a classical standpoint, Čerenkov radiation can be viewed as the coherent summation of the polarization field induced by the charged particle traversing a polarizable medium. This leads to a non-vanishing value of the Poynting vector[1] for directions with a common angle with respect to the direction of motion of the particle. The condition for the emission of photons is that the speed of the particle β must exceed $1/n(\omega)$, where n is the refractive index of the medium for photons of angular frequency ω. Naturally the medium must be transparent at the wavelength concerned, although an optical attenuation length significantly greater than the photon wavelength does not affect the theory as the attenuation process can be treated independently. The simplest version of the theory assumes that the medium is a linear isotropic homogeneous dielectric with unit (relative) magnetic permeability. The effects of multiple Coulomb scattering and energy-loss resulting from ionization of the medium are also ignored, although these are not significant constraints to the theory for electrons stopping in commonly occurring media.

According to the theory of Frank and Tamm, photons of (angular) frequency ω are emitted at a zenith angle θ_c with respect to the direction of motion, where θ_c is given by the coherence condition $\cos\theta_c = 1/\beta n$. However, the opening angle can be derived on dynamical grounds,

[1] The vector representing the flux of electromagnetic energy.

using a semi-classical approach to photon propagation, see Appendix B. The azimuthal angle of emission is random, as demanded by cylindrical symmetry, so the radiation is said to be emitted on a cone of half-angle θ_c. The theory also predicts the yield of Čerenkov radiation, which can be expressed in terms of the number of photons N emitted in an angular frequency interval $d\omega$, along a charged particle track length dx, as

$$\frac{d^2N}{dx\,d\omega} = \frac{\alpha}{c}\left(1 - \frac{1}{\beta^2 n(\omega)^2}\right), \tag{3.1}$$

if $\beta > 1/n$ and zero otherwise, where α is the fine structure constant and c is the speed of light in vacuum.

Since the energy of an individual photon is $\hbar\omega$, the energy emitted as Čerenkov radiation diverges with decreasing wavelength, but this 'ultra-violet catastrophe' is averted by the behaviour of the refractive index beyond the regions of anomalous dispersion. These regions are so called because the value of the derivative $dn/d\omega$ is negative, caused by resonance phenomena, and this can cause the refractive index to fall below unity for some frequency bands. These bands are typically just above the resonant frequency of the anomalous dispersion. In these frequency bands the refractive index is less than unity, so that Čerenkov radiation cannot occur. For frequencies greater than the highest of these bands, the refractive index (via the dielectric constant) is determined by the electron plasma frequency of the medium [35]. One consequence (critical for Čerenkov radiation) is that in the wavelength limit $\lambda \to 0$, the refractive index of matter approaches unity from below, and so the ultra-violet catastrophe is avoided[2].

How valid are the assumptions of Frank and Tamm to the processes of stopping electrons in a low Z material such as water ? The central assumption that the emission of Čerenkov radiation can be treated classically is quite valid in the optical wavelength region, where the photon energy is much less than the electron rest mass [109]. Here one finds that the predictions of quantum mechanical treatments [63, 64] reduce to the classical ones, as required by the correspondence principle. The classical study of Nag and Sayied [65] demonstrated that for magnetic materials the yield of equation (3.1) is increased by a factor μ_r, the relative permeability of the medium. However, the requirements that the dielectric media are optically inactive, linear and non-magnetic ($\mu_r = 1$) are satisfied with high precision for the materials encountered in the SNO detector and in the Čerenkov sources described in this work. Further, for optical wavelengths these materials have a slowly changing refractive index (as a function of wavelength), with a small imaginary component. Small amounts of impurities in these materials can shorten attenuation lengths, and in the range of wavelengths of interest to this work (300 nm $< \lambda <$ 600 nm), these must be measured separately. Typically, the imaginary part of

[2]The ultra-violet catastrophe is also avoided by considering the dynamics of the energy and momentum of the photon created. The approximations used to derive Equation 3.1 are not valid for short wavelength photons.

the electric susceptibility $\chi_e(\omega)$, where $\epsilon_r = 1 + \chi_e$, increases towards the short wavelength end of this range, and the optical transmission of the materials under consideration effectively have a short wavelength cut-off. However, in bulk materials this point is reached whilst the imaginary component is still small compared to unity (about 3×10^{-5}), and the Kramers-Kronig relations[3] guarantee that the real component of the electric susceptibility changes slowly over such an interval.

The change of particle velocity in the dielectric caused by ionization, Coulomb scattering and the production of bremsstrahlung photons will affect the coherence of the polarization field. However, the coherence condition is established promptly, and provided the stopping power causes only a small fractional change in the velocity of the charged particle during one cycle of the photon frequency, the production of Čerenkov radiation is unaffected. The most critical case is when the electron is just above the threshold velocity, $\beta = c/n$, and so this condition reduces to

$$\frac{d\beta}{dt} \ll \frac{\omega}{n} . \tag{3.2}$$

This condition is easily satisfied for the range of electron energies and stopping powers of materials used in the SNO detector and in the Čerenkov sources described in this work. Hence the classical theory of Frank and Tamm provides an accurate prescription for predicting the yield of Čerenkov radiation (in the defined wavelength region) from materials considered in this work.

Although the theory of Frank and Tamm is believed to predict the yield of Čerenkov radiation correctly, there are several other mechanisms whereby a significant flux of ultra-violet photons can be generated by the motion of a charged particle through matter. In particular, many materials scintillate when traversed by high energy charge particles. Even if a material is only weakly scintillating, this will often dominate the yield of ultra-violet photons (about 400 nm wavelength). In water scintillation light is negligible compared to that from Čerenkov radiation for electrons above threshold. A limit has been placed on the yield of scintillation light from acrylic[4], by using both a 400 MeV proton beam (below Čerenkov threshold) and a 400 MeV pion beam (above threshold) on an acrylic[5] target. The protons incident on the acrylic would have created some Čerenkov radiation via δ-rays, but it was still possible to establish that the scintillation yield was at least 5 orders of magnitude lower than typical Čerenkov radiation yields above threshold.

In addition, when electrons propagate through matter they can produce bremsstrahlung photons, from interactions with the atomic nuclei of the surrounding medium. Radioactive beta decay sources are used in this work, and these decays generate internal bremsstrahlung. Both

[3]The Kramers-Kronig dispersion relations predict a connection between the real and imaginary parts of χ_e.
[4]N. W. Tanner, private communication.
[5]Polymethylmethacrylate is referred to as acrylic in this work.

of these fluxes of bremsstrahlung photons are believed to be negligible compared to Čerenkov radiation (at optical wavelengths), but not trivially so, and estimates of their contribution are made in Chapter 4. Measurement of the light emitted from tritiated H_2O (Czapski and Katakis [66]) and D_2O (Earle in annex 13 of [55]) suggest that the total amount of light produced in water by electrons below Čerenkov threshold is of order 10^{-5} photons per 100 eV of energy deposited. This has been attributed to bremsstrahlung photons and from the de-excitation of He^+. Taken together, this evidence strongly suggests that for the sources used in this work and for electrons above the Čerenkov threshold in the SNO detector, the Čerenkov effect gives by far the largest yield of optical photons.

3.1 Computations of Čerenkov radiation yields

The sources of Čerenkov radiation described in this work require accurate computations of the total light yield from stopping electrons. The method used to compute the yield of Čerenkov radiation from a stopping electron is to follow the propagation of the electron shower through the medium, and integrate expression (3.1) along the tracks of the charged particles present. The differential expression of the Čerenkov yield is therefore convenient for numerically computing the total emitted radiation from a stopping electron. However, there is a complication arising from the fact that the total number of electrons above the Čerenkov threshold is not constant during the shower. A relativistic electron can produce a 'knock-on' electron (sometimes called a δ-ray) by an elastic collision with an atomic electron, or a high-energy γ-ray which can subsequently produce a δ-ray, or an electron-positron pair at higher energies. All of these effects are subject to chance, but the probability of an interaction producing an energetic secondary particle increases with initial electron energy.

The integration of Equation (3.1) takes the form

$$\frac{dN}{d\omega}(\omega) = \sum_j \int_{T_j} \frac{\alpha}{c}\left(1 - \frac{1}{\beta_j^2 n^2(\omega)}\right) dx_j \,, \tag{3.3}$$

where the sum is over all j charged particles in the shower which exceed the Čerenkov threshold, and the integral is along the charged particle track T_j of the j^{th} particle. In general the tracks of the charged particles can pass through media of different refractive indices, and so the value of n is a function of position. Before the sum/integral can be performed, the kinematic relation for β as a function of distance, and details of the other charged particles, must be provided. Because of the random nature of the stopping mechanism, probability distributions should be used. Henceforth it is assumed that the energy of the shower is low enough so that only electrons (and positrons) can emit Čerenkov radiation.

Since the interactions of electrons and photons are random (non-deterministic), the integrated yield of Equation (3.3) is different for electrons with identical initial conditions. Conse-

quently, it is difficult to proceed with computations in an analytic way. Two ways of overcoming this difficulty are presented in this work: firstly, a Monte Carlo method is used to track all particles in the shower, incorporating all the physical processes, and thus computing an expectation value for the quantity $dN/d\omega$ in Equation (3.3). Secondly, gross approximations can be made which enable the computation of $dN/d\omega$ by definite (numerical) integration. This involves assuming that all the Čerenkov radiation is generated from the initial electron, that there is no straggling[6], that there is only one medium present, and that the stopping power of electrons is accurately predicted by ICRU tables [67]. These tables provide the stopping power per unit density for various materials, with a resolution of 16 stopping power data points per decade of electron kinetic energy. Using this relation between kinetic energy and distance, the analytic approximation reduces Equation (3.3) to

$$\frac{dN}{d\omega}(\omega) = \int_{E_i}^{\beta(E_f)=1/n} \frac{\alpha}{c}\left(1-\frac{1}{\beta^2(E)n^2(\omega)}\right)\left(\frac{dE}{dx}\right)^{-1} dE\,, \tag{3.4}$$

where E_i and E_f are the initial and final electron kinetic energy, and the upper integration limit is the equation whose solution gives the energy of the electron at threshold. Hence the final energy is defined by the threshold for the production of Čerenkov radiation. By using the stopping power dE/dx in this continuous fashion, the integral is thus transformed to a summation with respect to kinetic energy. Note that there is another assumption implicit in this use of the stopping power; that the expectation value of the reciprocal of the stopping power is the reciprocal of the expectation value of the stopping power. This approximation is thought to be satisfactory at electron energies of order 1 MeV.

In this work, good agreement is demonstrated between these two methods for low energy electrons, with kinetic energy between the Čerenkov threshold (175 keV in acrylic) and the end-point of ^{90}Y, 2.28 MeV. In this energy range the analytic approximation is valid, and the results are used to verify the results of the Monte Carlo shower simulation routine and its implementation. This approximation is used to check computer code simulating the production of Čerenkov radiation from low energy electrons, for example those produced from the beta-decay of ^{90}Y. For energies above several MeV the analytic approximation breaks down, predicting less Čerenkov radiation than the Monte Carlo method. Most of the extra contribution to the Čerenkov yield comes from the contribution of δ-rays. These data are presented and discussed in more detail in the next section along with details of the EGS4 Monte Carlo code.

[6] Landau 'straggling' refers to the process by which the electron path length acquires a spread.

3.2 The EGS4 Monte Carlo system

The EGS code system is an Electron Gamma Shower transport algorithm, which tracks electrons and photons in a probabilistic fashion suitable for use in Monte Carlo simulations. This system is widely used for particle transport in a wide range of high energy physics simulations, and is extensively documented by the authors Nelson, Hirayama and Rogers [59]. The current version, EGS4, includes all the important electron and photon interactions necessary for the reliable transport of low energy electron showers with initial energy greater than 100 keV. This enables the code to be used in Monte Carlo simulations of the Čerenkov radiation from low energy electrons. The specific use of the code for low energy electrons has been documented by Rogers [68], Jenkins *et al.* [69], and the production of Čerenkov radiation has been subject to investigation by the author of this work with colleagues D.L. Wark and M. D. Lay, [70]. The data presented in this section focus specifically on the total yield of Čerenkov photons produced in a low energy electron shower.

The physics used in the EGS4 code system is well documented in the report [59], but for completeness a brief summary of the processes relevant to this study are listed below.

1. The multiple (Molière) scattering of electrons by nuclei (as a consequence of Coulomb interactions) is included.

2. The production of bremsstrahlung photons is included, but unfortunately the Elwert correction factor [71, 72] is not implemented in this version.

3. Continuous energy loss is used to propagate a particle whenever a discrete interaction is not used in a particular section of track length. The stopping power is computed from the sum of the soft (below the threshold for treatment as a discrete interaction) bremsstrahlung and the collision loss. The collision loss is computed using the Bethe-Bloch rules with corrections for the density effect[7].

4. A simple version of the photoelectric effect is used, whereby only the primary photoelectron is subsequently tracked. Auger electrons and atomic fluorescence are ignored.

5. Pair production is included. The subsequent positrons are tracked by the code, and positron annihilation is included.

6. Bhabha (e^+e^-) and Møller (e^-e^-) scattering are included using exact expressions.

7. Compton scattering is included.

[7] The treatment of Sternheimer is implemented.

One possible problem for low energy electron showers is the omission of the Elwert correction factor, see [72], also discussed by Rogers [68], which means that EGS4 incorrectly estimates the number of bremsstrahlung photons generated in an electron shower. However, in the specific application of the code reported here, it is not thought to have significant effect on the yield of Čerenkov radiation from the shower. This is because only a tiny fraction of the total yield results from intermediate bremsstrahlung photons; for example such a photon could Compton scatter an electron. Further, the effective stopping power of the electron is also believed to be unaffected, as the code always ensures that the sum total (mean) stopping power is independent of the contribution from one particular interaction. It is the effective stopping power which is calibrated against experimental data, see below.

In the current implementation the routine SHOWER propagates a particle until it reaches a boundary, or it has lost a pre-determined fraction ESTEPE of its kinetic energy. Alternatively, the step may involve an interaction which causes another electron or photon to be created with kinetic energy above pre-determined limits, called AE and AP respectively, above which the individual particles are transported separately. Thus AE and AP affect the fraction of the total stopping power which is attributed to discrete interactions as opposed to continuous energy loss. In the current study, the energies (ECUT and PCUT) below which any particle is no longer tracked are set equal to AE and AP respectively. The EGS4 code system has a pre-processor code called PEGS4, which makes linear fits (as a function of energy) to the cross-section and branching ratio data that are required for each material to be used in the simulation. These data are computed for energies down to AE and AP for electrons and photons respectively.

The most basic verification of the implementation of the EGS4 code is the requirement that the predicted amount of Čerenkov radiation should be insensitive to the choice of internal parameters, AE, AP and ESTEPE discussed above. An investigation of the sensitivity of the yield of Čerenkov radiation to changes in the parameter ESTEPE was performed for 20,000 electrons of initial kinetic energy 1 MeV. These were propagated in an infinite medium of water of unit density and refractive index 1.343. The values of AE and AP were set at a low value of 3 keV, and the values of ESTEPE were chosen in the range 1% to 20%. A program called EGS4TEST was used to perform the sum (3.3), and calculate an estimator of the unbiased standard deviation of the distribution of Čerenkov radiation from electrons with identical initial conditions. The results of the simulation are shown in Figure (3.1), in which the error bars indicate the values of the unbiased estimator of the standard deviation of the mean yield estimator [8]. Note the offset along the yield ordinate.

The data clearly demonstrate the small sensitivity of the total yield of Čerenkov radiation

[8] Unless stated otherwise, 'error bars' refer to a statistical estimator throughout this work.

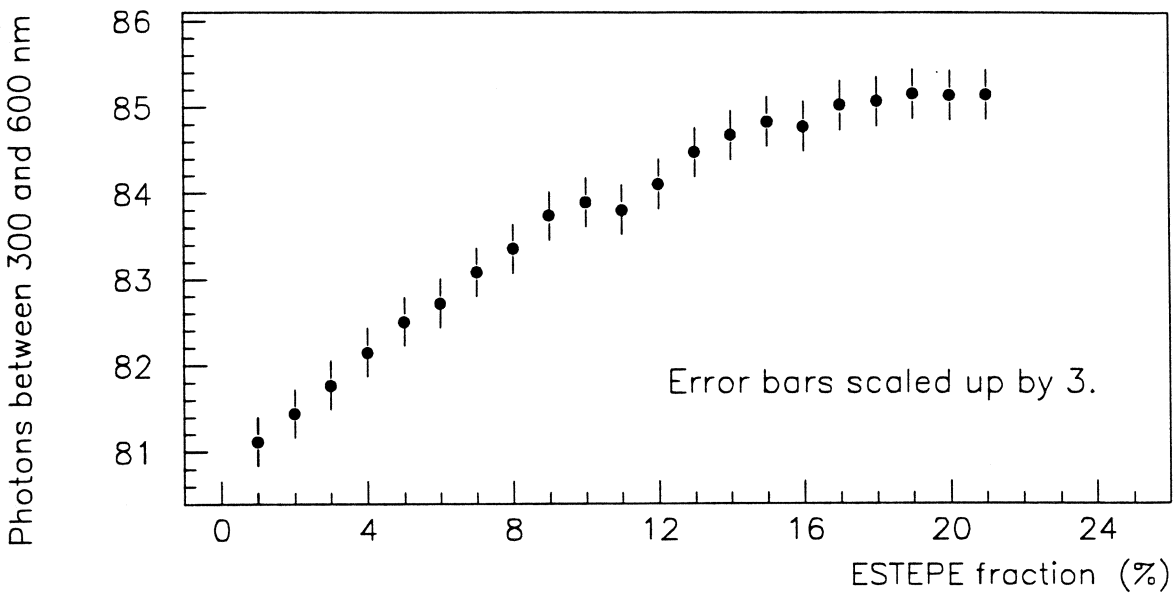

Figure 3.1: The variation of Čerenkov yield with ESTEPE for 1 MeV electrons in water.

to the step size parameter ESTEPE. The observed increase of yield (expressed as the number of photons in the wavelength range 300 to 600 nm) with ESTEPE is believed to be from the approximation made in the code whereby the velocity β is assumed to be constant over the interval of size ESTEPE, and this value of β is used when evaluating the yield of Čerenkov radiation[9]. However, in reality, the value of β is declining during the interval, and so an overestimation of the Čerenkov yield is made. This explanation also accounts for the observation that the dependence on ESTEPE, as a fraction of the total yield, falls with increasing electron energy. This error vanishes as the step-size ESTEPE tends to zero. Hence it is likely that the most reliable results, as far as yield is concerned, will be obtained with small values of ESTEPE. Since it is unlikely that the absolute values of the stopping powers are correct at the one percent level, values of ESTEPE lower than about 4% are probably sufficient. Note that there is a price to be paid in execution time for using small values of ESTEPE; the program execution time is approximately inversely proportional to $\ln(1 - \text{ESTEPE})^{-1}$.

The sensitivity of the results to changes in the values of AE and AP are investigated in the same way. In an exact simulation, the predicted Čerenkov yield would be independent of both AE and AP, unless either was above the Čerenkov threshold. Above this threshold, the yield should fall monotonically with increasing AE and AP, until AE reaches the initial particle energy, whereupon the yield should be zero. The latter condition is well satisfied, but the condition that the yield of Čerenkov radiation be independent of AE and AP below threshold is a more stringent test of the Monte Carlo code. In principle we may expect to see small changes in the yield as AE and AP are changed as this effectively 'turns off' the

[9]The computation of 'average' value of β is complicated by discrete interactions and is not performed here.

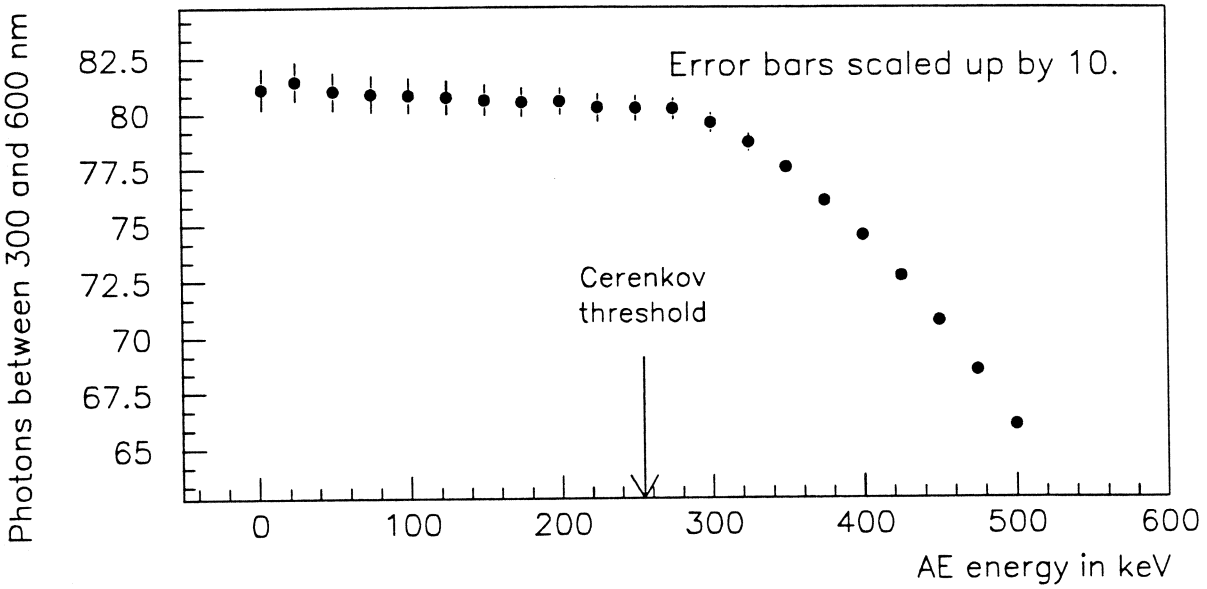

Figure 3.2: The variation of Čerenkov yield with AE for 1 MeV electrons in water.

straggling of the electrons, and the averaging process may be biased.

The program EGS4TEST was used to track 20,000 electrons of kinetic energy 1 MeV, in an infinite medium of water, using different values of AE and AP. In the study AP was found not to effect the Čerenkov yield from these electrons, and this parameter is set at AE. The results of varying AE (and AP) in the range 3 to 400 keV are shown in Figure 3.2, where the energies refer to kinetic energy, not total energy. It is clear that the yield drops as the parameter AE is raised above the Čerenkov threshold (254 keV for $n = 1.343$). However there is some evidence that the yield also falls with increasing AE below the threshold, but this effect is small. It may be conjectured that this is an effect of the straggling process described above, and if this were the case the results at low values of AE would be the most reliable. Simulation of electrons of different energies suggest that this effect is largest at low energies, and is consistent with the conjecture that the effect is caused by straggling. Again there is a price to be paid for using low values of AE; the execution time increases with smaller values of AE and varies in approximate proportion to $\ln E_i/\mathrm{AE}$, where E_i is the initial kinetic energy.

The comparison of the results of the EGS4 Monte Carlo and the analytic approximation is a useful one for determining relative accuracy and finding coding errors. When a Monte Carlo simulation code of this type is written, it is vital to perform as many tests of the predictions of the code as possible, as this is often the only way of finding relatively small systematic errors. In the simulation presented here, an error which affected the yield by 5% may go undetected as a simple numerical (order-of-magnitude) check of the result may not find the error. Errors much smaller than this are not important in the the current work.

It should be stated clearly that there are many common physical assumptions made in

these two simulations, despite the very different methods employed. The key assumption of the validity of the theory of Frank and Tamm is used throughout. In addition, the degree of independence of the stopping power tables and the rules used by PEGS to generate the look-up tables is uncertain, but it is likely that many formulae and assumptions are common to both.

In this investigation the EGS4 routine was used with the parameter ESTEPE set at 1%, and AE and AP set to 150 keV for speed of computation. The stopping medium chosen was acrylic of density 1.182 g/cm^3, and refractive index 1.50. A program called EGS4CEREN was used with the EGS4 code to compute an estimator of the sum of Equation (3.3), by tracking 30,000 electrons. These data were compared with the results of definite integration using the analytic approximation, Equation (3.4), as computed by a program CEREN, which performs the integration using a third-order finite-difference method[10].

The results for low energy electrons are plotted in Figure 3.3, where the continuous line represents the prediction of the analytic approximation, and the data points (denoted by crosses) represent the results of the EGS4 Monte Carlo code. The random errors in the latter case are within the size of the displayed crosses, the standard deviation of the mean estimator of the yield is about 0.5%. The data in the figure demonstrate remarkable agreement between the two simulation methods. Note that there has been no normalisation factor applied to these data, and we conclude that errors from simulation alone are less than 1% for electrons with kinetic energy in the range shown in the figure. From this we conclude that for electrons from the beta-decay of ^{90}Y, with an end-point of 2.28 MeV, the errors caused by simulation alone are small.

However, the data at intermediate energies, shown in Figure 3.4, demonstrate systematic differences. The continuous line and the crosses are as before, and the circles show the EGS4 predictions of the yields from the *initial electron only*. The yield from the initial electron is for comparison with the analytic approximation. The difference between the yield of these two in the EGS4 predictions is largely caused by the contribution of Čerenkov radiation from δ-rays, and hence this difference vanishes at low energies. The initial electron yield of EGS4 and the analytic approximation show reasonably good agreement.

Direct experimental tests of the EGS4 code have been presented by Rogers [68] and many are quoted in the description of EGS4 [59]. Many of these comparisons are sensitive to the scattering properties of the medium as well as its electron stopping power. An investigation by M. D. Lay, see [70], has shown that many of these experiments where scattering is important can be reconciled with the prediction of the EGS4 code given a suitable choice of internal parameters. Such a choice, particularly of the parameter ESTEPE = 3%, can reproduce most

[10] Based on the approach of Gill and Miller, see [73].

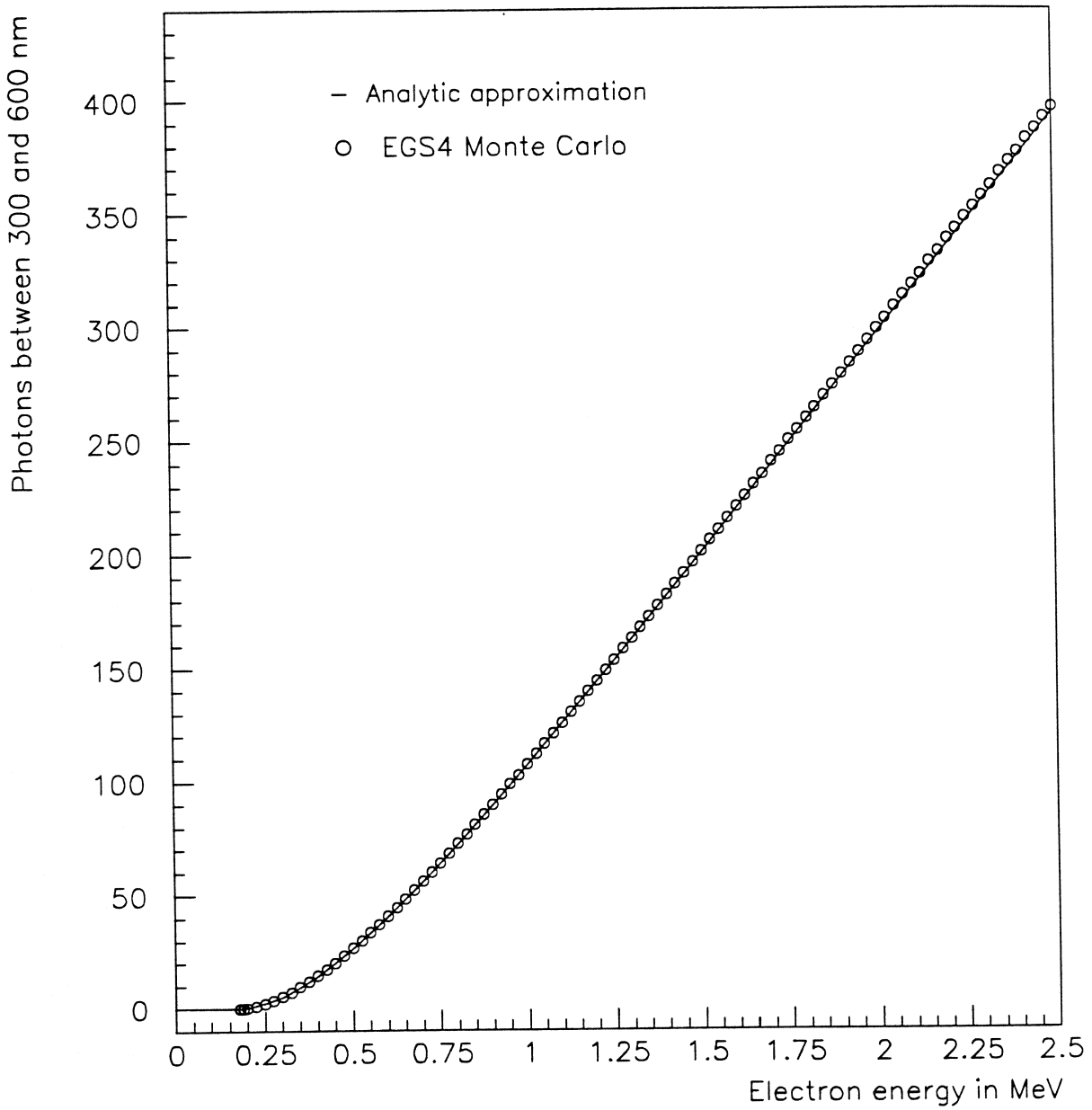

Figure 3.3: The Čerenkov yield in acrylic from low energy electrons. The crosses show the EGS4 data whilst the solid curve shows the analytic approximation.

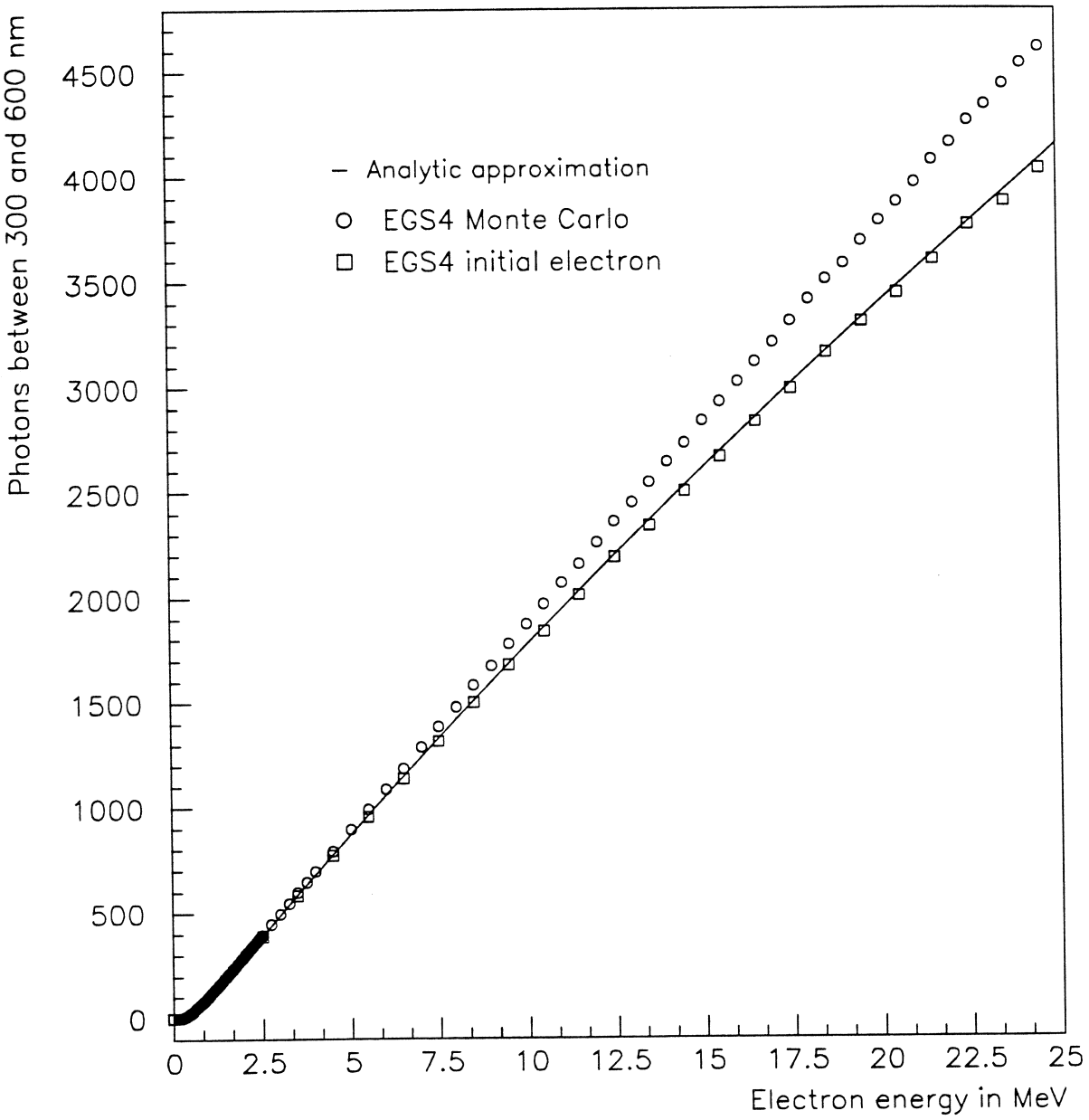

Figure 3.4: The Čerenkov yield in acrylic from intermediate energy electrons. The EGS4 data are shown as crosses for the full yield and circles for the initial electron only. The solid curve shows the analytic approximation.

experimental results. ESTEPE is seen to have a significant effect on the predictions of the multiple scattering of electrons.

The simulations presented here, which seek to predict the Čerenkov yield, are relatively insensitive to ESTEPE, but depend critically on the electron stopping powers. There are surprisingly few reliable experimental measurements of the stopping powers of electrons at low energies to compare with the predictions of EGS4 and the values quoted in the ICRU tables. Paul and Reich [74] have measured the stopping power of several low Z materials at electron energies of 2.8 MeV and 4.7 MeV. Their experimental data suggest that the ICRU predictions of the stopping powers of various materials at 2.8 MeV are systematically higher than experimental values by about 3%. According to the data presented, the disagreement can be established with high (97%) statistical confidence. However, it is felt that there is insufficient justification on the basis of these results at one energy to question the predictions of EGS4. In fact agreement at the 3% level is quite reasonable when the difficulty of performing the experiment at the 1% level is considered. Henceforth the EGS4 code and the stopping powers are separately assigned a conservative error estimate of about 2% each.

Chapter 4

Čerenkov sources

In this chapter the simulation and construction of Čerenkov sources, based on the encapsulation of a radioactive beta source inside a sphere of transparent material, are described. These sources are required to have several properties which enable them to be used as 'calibration sources', for both the SNO detector and for the measurement of photomultiplier photon counting efficiency, described in the following chapter.

An important requirement of such a source is that it must be constructed in a way which enables a reliable estimate of its light output to be made via simulation. If the source is to be used for calibration then it should not deviate with time from the computed intensity. As with most radioactive calibration sources, it is required to be robust and to have minimal surface contamination. If the source is to be used to calibrate the response of photomultipliers in the SNO detector, these latter constraints would become critical. The source must also radiate light of appropriate intensity so that the photomultipliers which detect the photons count at an acceptable rate. In practice this is achieved by altering the amount of beta decay activity in the source.

When using a Čerenkov source with a photomultiplier, the rate of production of photoelectrons by the cathode should be greater than the noise rate of the photomultiplier, to minimize errors when subtracting this background signal. Hence the noise rate of the photomultiplier tubes provides a lower limit for the activity of the sources described in this work. The 200 mm photomultipliers of the type used in the SNO detector typically have noise rates of order several kHz[1]. If the source is too intense, the photomultiplier cathode will liberate photoelectrons separated by a time interval which is short compared with the duration of the current pulse along the dynode stack, typically 20 ns. If a reliable measurement is to be taken, the chance of pulses overlapping must be small and thus the rate of counting photoelectrons must be much less than 50 MHz.

This scheme is complicated by the fact that the Čerenkov radiation is produced in 'pulses',

[1]The use of frequency units for describing the counting rate of photomultiplier is not strictly valid as the signals are not periodic. However Hz are used in this work, with this caveat.

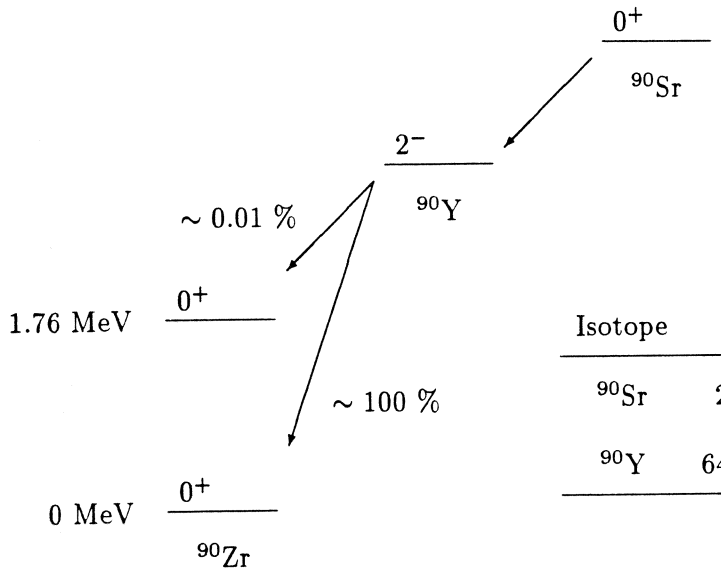

Isotope	Half-life	End-point (MeV)
^{90}Sr	28.6 ± 0.3 y	0.546 ± 0.001
^{90}Y	64.07 ± 0.16 h	2.2792 ± 0.003

Figure 4.1: The beta decays of ^{90}Sr and ^{90}Y.

when a beta decay event occurs. Now the limitation on the maximum activity used is extended to exclude a significant probability of more than one photoelectron being produced by a single beta decay. This extra constraint provides a limit on how closely a photomultiplier and a source can be placed together. It should be stressed that this condition is independent of the amount of radioactivity used in the source. For the ^{90}Sr used in this work, the minimum distance is about 0.5 m, when using a 200 mm bialkali cathode photomultiplier.

The work of Anderson and Belcher, reported in [75], has demonstrated that Čerenkov sources based on radioactive beta decay encapsulated in a transparent phial (Anderson and Belcher used cylindrical glass phials) are capable of satisfying the above conditions. The choice of radioisotope is principally dictated by the requirements of long half-life and no γ-ray transitions. Furthermore the radioisotope should be available in an appropriate chemical form not only for encapsulation, but also to enable an accurate determination of its specific activity to be made. Anderson and Belcher used three isotopes, namely ^{204}Tl, ^{90}Sr, and ^{32}P. The phosphorus isotope is rejected because its half-life is only 14.3 days, and ^{204}Tl is also unsuitable as the beta decay electrons have an end-point of only 775 keV. ^{36}Cl, with an end-point energy of 709 keV, is similarly unsuitable, as beta decays with end-point energies of about 700 keV produce an order of magnitude less Čerenkov radiation than ^{90}Sr, for similar amounts of activity.

To improve the accuracy of a Čerenkov source simulation, it is important to consider the ease of computation of the beta decay spectra of candidate isotopes, and also to select decay nuclei that do not have associated γ-ray transitions. With modern simulation techniques, such as the EGS4 Monte Carlo, this restriction is not quite so critical as the Čerenkov yield

from energetic electrons from Compton scattering can be estimated. However, this would make the simulation more complex, and for reasons of radiation safety, decays producing a significant γ-ray flux are unsuitable. Counting of photons from a source producing γ-rays with a photomultiplier is further complicated as these γ-rays generates signals in the photomultiplier glass. For these reasons the isotope ^{90}Sr is used in all the sources described in this work. ^{90}Sr, and its daughter ^{90}Y, both have beta decay transitions which are free from γ-rays, and their first-forbidden beta spectra are relatively easy to calculate. The decay scheme is shown in Figure 4.1. The end-point of the ^{90}Y beta spectrum is quite high, 2.28 MeV, and therefore the yield of Čerenkov radiation per beta decay is relatively high. For 4π solid angle counting an average beta decay electron from a ^{90}Y decay produces about 10^2 photoelectrons from a bialkali photocathode. Also the half-life of ^{90}Sr is conveniently long, being approximately 28 years.

4.1 Encapsulation materials

In this section the optical and physical properties of the materials used to encapsulate the ^{90}Sr are described. For the purposes of simulation, the density, refractive index and optical transmission of the encapsulation material should be known accurately. These properties are significant as the material used to construct a source serves not only for encapsulation, but also as the Čerenkov medium for the stopping electrons. The optical transmission of all the media used should be measured, so that a reliable estimate of the spectral luminance of the source can be made. (Since the spectrum of Čerenkov photons $n(\lambda) \sim 1/\lambda^2$ rises sharply at short wavelengths, the optical transmission is particular important in this region.) The materials used for encapsulation were borosilicate glass, and several grades of glassy acrylic. In some sources the radioactive nuclide was dissolved in solution with high-purity water.

These materials usually have a pronounced short wavelength cut-off, which is often quite sharp, but it is inevitable that the bulk attenuation length is reduced for larger wavelengths before the cut-off point. This introduces a source of error into simulations of the spectral intensity of the Čerenkov sources used. The approach taken in this work is to accept that this is inevitable and to use only the unambiguous wavelength region, i.e. those not dependant on the transmission at short wavelengths. In Chapter 5 an experimental procedure is described which greatly reduces the sensitivity of the photomultiplier measurements to the source luminance at wavelengths shorter than about 370 nm. This is achieved by filtering the light from a source using a sheet of 'uv-stabilized' acrylic[2] of well known optical transmission. As a result of this technique, the experimental measurements described in this thesis are not sensitive to uncertainties of optical transmission at wavelengths shorter than 370 nm.

[2]This has additives which impede the transmission of ultra-violet photons.

However, it is still vital to measure the transmission properties of these materials, so that the cut-off wavelength can be determined, and the transmission at longer wavelengths can be verified. The measurement of optical transmission was performed used a Perkin-Elmer Lambda-9 spectrophotometer[3], which can measure transmission over the range of wavelengths of interest, between about 300 and 700 nm. Several samples of glass and many of acrylic have been tested, and some typical raw data, uncorrected for (Fresnel) boundary reflections, are shown in Figure 4.2.

The triangles of Figure 4.2 show the transmission of a 4 mm thick sample of high-purity grade borosilicate glass known as Schott 8246. This glass has special significance since it has been used to manufacture bulbs for the Hamamatsu R1408 photomultipliers for the SNO detector, and the curve represents a short wavelength limit on the quantum efficiency of these photomultipliers. Several of the photomultipliers tested in this study were made from Schott 8246. A Čerenkov source was constructed with a borosilicate glass bulb, and its transmission curve is similar to that shown in Figure 4.2.

The squares in the figure show the transmission of a sample of ICI 'Perspex' acrylic, of thickness 12.7 mm (1/2 inch). This material has had an uv-stabilizer added to the monomer to ensure that the acrylic is not damaged by ultra-violet radiation. The effect of this additive is to attenuate ultra-violet light with wavelengths shorter than about 370 nm. This material was used not only to construct some sources with well-defined spectral intensity, but also to provide filtration when using sources with unknown spectral intensity at short wavelengths.

The circles in the figure show the transmission of a 51.0 mm thick sample of 'Polycast'[4] acrylic, which is free from the uv-stabilizer described above. The data clearly show that there is evidence of deviation from the 92% transmission (from 4% Fresnel reflection at each acrylic/air interface). This could be caused by scattering of light due to surface imperfections, but bulk attenuation cannot be ruled out from these data. For more detailed treatment see Davidson *et al.* [57]. Acrylic without uv-stabilizer is to be used for the acrylic vessel in SNO, and one may expect its transmission to be similar to this sample. Some sources were made using this Polycast material, but they were not found to be satisfactory; details are given in the next section.

It should be noted that only the bulk attenuation length is of interest in the Čerenkov sources described here, as Fresnel reflections do not reduce the light output from a source. A photon reflected at one boundary will traverse the source and, given no bulk attenuation, have a similar probability of transmission on the opposite side. Since the sources described in this work are (approximately) spherically symmetric, this process is equally likely at all angles, and hence interface reflections may be ignored. This symmetry argument also implies that

[3]Thanks are due to C. Goodwin for his assistance with the operation of the spectrophotometer.
[4]Supplied by the Polycast Technology Corporation.

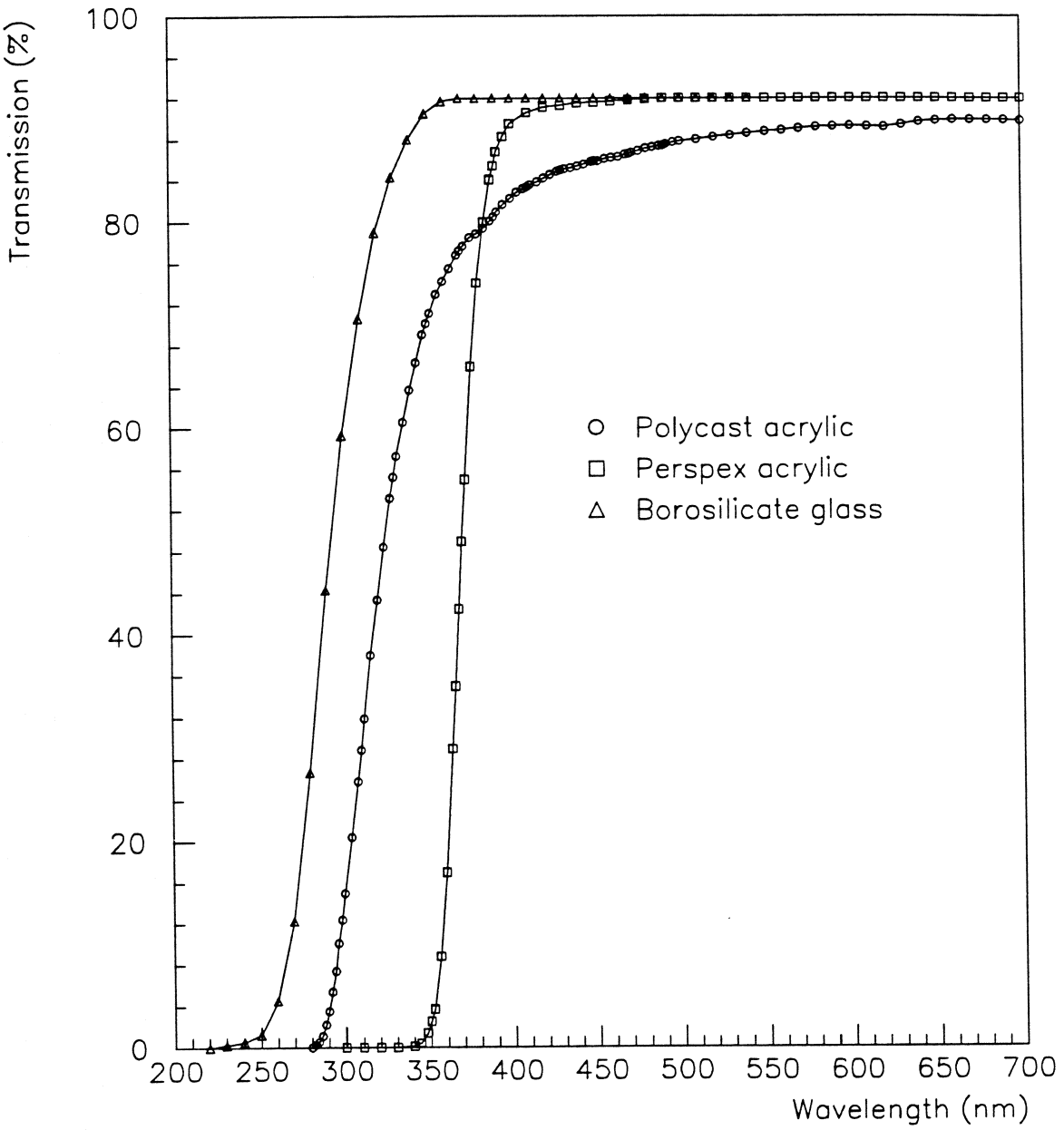

Figure 4.2: The optical transmission of encapsulation materials. The triangles represents Schott 8246 glass, the circles represents uv-stabilized acrylic, and the squares represents high purity non-stabilized acrylic.

Material	Density (at 20°)	Refractive index (at 404 nm)	Čerenkov threshold
Acrylic	1.181	1.505	173 keV
Water	1.000	1.343	255 keV
Glass	$\simeq 2.5$	$\simeq 1.51$	$\simeq 171$ keV

Table 4.1: The properties of some Čerenkov media.

Rayleigh scattering within the bulk material of the source can be ignored.

The refractive index of the electron stopping medium is clearly important to the simulation of Čerenkov radiation, as both the threshold and rate of photon production are affected by the refractive index. It is quite common to assume that the refractive index of media such as water and acrylic are constant over the range of wavelengths to which bialkali cathode photomultipliers are sensitive; between 300 and 700 nm. This is a satisfactory approximation in most cases because the refractive index of such materials changes slowly in this range of wavelengths. However, the effects of the increase of refractive index with decreasing wavelengths are assessed in this study.

Fortunately there are many reports of accurate measurements of the refractive index of acrylic and water. Detailed measurements of the refractive index of a sample of non-stabilized acrylic, of similar density to that of the Polycast acrylic, have been made by Roehm Limited. Their refractive index data are believed to have random errors of about 0.01%, and this study uses their data set. A simple attempt, using a travelling optical microscope, was made to verify that their data was appropriate for this acrylic sample at one wavelength, the sodium D line. The result was $n_D = 1.4956 \pm 0.008$, compared to the Roehm result of $n_D = 1.49031 \pm 0.0002$. The results are consistent, with a difference of about two-thirds of one standard deviation. The effort to improve significantly on the accuracy of this simple check was considered to be unjustified, particularly because these errors are small compared to the change in refractive index with wavelength. In this study it is most important to evaluate the refractive index at the appropriate wavelength, corresponding to that which most photons are counted by a photomultiplier with a bialkali photocathode. As demonstrated in the next section, this is about 400 nm. The data set is shown in Figure 4.3, along with a 7^{th} order fit to the data made for computation purposes. For comparison, the refractive index of water is shown in the figure, denoted by the boxes, from data taken from Kaye and Laby [76]. All data are measured at 20°C.

The density of the Polycast acrylic used was measured and was found to be $\rho = 1.181 \pm$

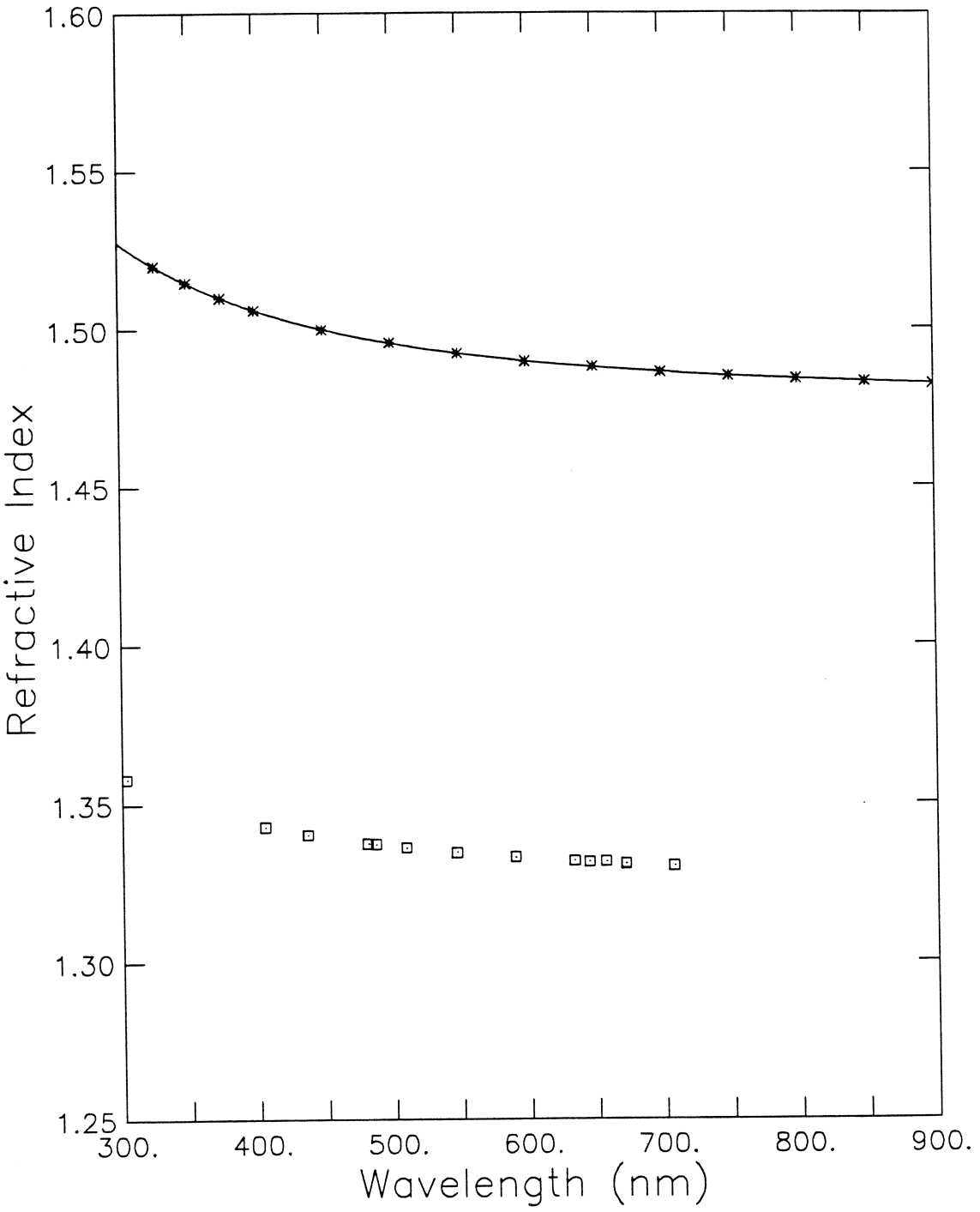

Figure 4.3: The refractive index of acrylic and water. The points denoted by an * show the refractive index of a Roehm acrylic without uv-stabilizer, see text for details. The continuous line shows a 7^{th} order fit to the Roehm data. The boxes indicate the refractive index of water.

Source number	I	II	III	IV(h)	V(h)	VI(h)
Activity (kBq)	130.5	125.2	120.4	140.3	149.0	160.1

Table 4.2: The activity of ^{90}Sr in Mark 1 sources on September 15, 1989.

0.004 g/cm^3 at 20°C. It should be noted that the reproducibility of such measurements is limited, as acrylic is known to absorb water vapour from the air, which increases its density. The value assumed henceforth is $\rho = 1.181$ g/cm^3, with an error estimate of 0.5%. Since the amount of total Čerenkov radiation produced from a stopping electron is inversely proportional to the density of the medium, for a known stopping power, this will translate into a systematic error of 0.5% in the light output. The values of refractive index and density used in the simulations are shown in Table 4.1. Approximate values of these quantities for borosilicate glass are shown in the table. Again all quantities are measured at 20°C and the refractive indices refer to 400 nm light.

4.2 Source construction

In this section the methods used to construct and fill the sources are described. Sources of three main types were constructed, with some variations within each category. The first type of sources were prototypes made from ICI 'Perspex' uv-stabilized acrylic, three of which were spherical and three hemispherical; the latter were used for transit time spread measurements, as the flat face enables better optical coupling to a monitor photomultiplier. For the purposes of calibration, however, only the spherical ones will be considered, as they are easier to simulate. These sources have an outer diameter of 30 mm and a hollow spherical centre of diameter 10 mm. The inner and outer surfaces are polished, and appear smooth.

The hollow centre is achieved by machining out a cylinder from the spherical piece, and the end of this cylinder is machined to a hemisphere of diameter 10 mm. The cylinder is then filled with a 'plug' of the same acrylic grade and diameter whose end is machined to a concave hemisphere. The diameter of this cylindrical plug is chosen to be slightly larger than the hole, and is cooled with liquid nitrogen before insertion. Upon insertion, its temperature rises and the plug expands to fill the hole. The bond thus formed is very strong, and is optically transparent. A hole of diameter 0.85 mm was pre-drilled in the plug to allow the injection of radioactive solution.

A known activity of ^{90}Sr solution was injected into the sphere in the form of a weak (0.1M) hydrochloric acid solution. The mass of solution injected was measured by weighing the syringe (with sheath) before and after injection, and also weighing the acrylic sphere before and after

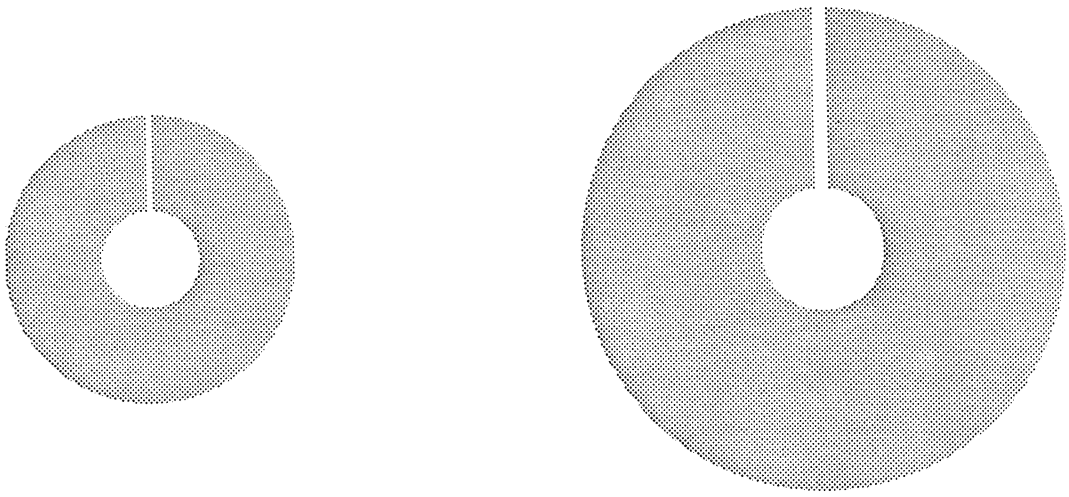

Mark 1 source

Mark 2 source

Figure 4.4: A section view of the Mark 1 and Mark 2 sources.

injection. An Oertling R20 balance, with a resolution of 0.1 mg, was used to weigh the sphere and syringe. After injection the liquid was allowed to evaporate, leaving the ^{90}Sr behind, and the sphere was then sealed with a small brass screw (12 BA). There was a slight trace of solid material left in the sphere after the liquid had evaporated. This was presumably the ^{90}Sr plus the carrier material. All the ^{90}Sr was assumed to remain in the source during evaporation. This assumption was checked by unsealing a source, refilling with water and evaporating to dryness again. The relative yield of Čerenkov radiation was measured using a photomultiplier before and after this refill and no difference was detected at the 1% level. The fact that the ratio of Čerenkov light yield to activity was indistinguishable for the spherical sources of the same type is also reassurance of no ^{90}Sr loss. The anisotropy of the water filled was estimated by counting at various orientations. No anisotropy was found at the 2% level.

The concentration of the ^{90}Sr solution used, 458 kBq per gram of solution, is quoted by the supplier[5] to an accuracy of $\pm$ 1.2% (systematic) $\pm$ 0.3% (random). This measurement is made using a liquid scintillation counter with 4π efficiency, and the measurement technique is accredited by the National Measurement Accreditation Service. The only other radionuclide present in the solution at a significant level (apart from the yttrium daughter) is ^{137}Cs, which represents 14 ppm of the total activity. The specific activity quoted by the supplier is used to deduce the activity in each sphere, with corrections for decay using a half-life of 28.6 $\pm$ 0.3 years. The activities deduced for the Mark 1 sources are shown in Table 4.2, where the (h) label indicates a hemispherical source.

[5]Amersham International plc.

Source number	VII	VIII	IX	X
Activity (kBq)	787.8	877.3	825.9	427.0

Table 4.3: The activity of ^{90}Sr in Mark 2 sources on July 15, 1991.

One possible problem with the Mark 1 sources is that it is possible to have total internal reflection for some Čerenkov photons generated at a distance r/n or further from the origin, where r is the outer radius and n the refractive index. Moreover, any Čerenkov photon suffering total internal reflection will do so again at each intersection with the outer acrylic surface, thereby trapping it until it is absorbed. The second set of sources, Mark 2, make an attempt to avoid this problem by increasing the size of the source, see Figure 4.4, and also to improve signal counting backgrounds by having greater enclosed activity.

The most energetic electrons from a ^{90}Y decay can emit Čerenkov radiation for a distance of about $R_c \simeq 9.3$ mm along their track length [67]. If total internal reflection is to be forbidden, then the radii must satisfy

$$r > n_{12}(R_c + r_i)\,, \tag{4.1}$$

where n_{12} is the ratio of the refractive index of acrylic to that of the surrounding medium. For Mark 2 sources the inner radius was set at $r_i = 6.35$ mm, in order to accommodate enough radioactive solution in the cavity. The outer radius was chosen to be $r = 25.14$ mm, so that relation (4.1) is satisfied for any external medium.

An identical method of construction and filling was used for Mark 2 sources, except more activity was injected into each. Table 4.3 shows the activity enclosed in the Mark 2 sources. Source X used the same batch of radioactive solution as the Mark 1 sources, whereas sources VII, VIII and IX used another batch. A systematic check was performed to check the variation of the specific activity of each batch by comparing the Čerenkov light yield per unit activity from source X to that from the other sources. No significant difference was found at the 1% level.

One possible objection to the Mark 2 source is that the transmission of the acrylic used in its construction is not sufficiently well known for wavelengths in the range 370 $\rightarrow$ 450 nm. The transmission data presented in Figure 4.2 were unable to eliminate the possibility of significant attenuation in this region and the light intensity could be reduced at the several percent level. Indeed the Mark 3 source described below produced 3% more light than those of the Mark 2 type. For this reason the Mark 2 was not used for absolute efficiency measurements.

The Mark 3 source, constructed from borosilicate glass, proved to be the most successful source. The source was made from a spherical glass bulb of mean diameter 51.14 mm, and av-

Outer diameter	Wall thickness	Volume of solution	Activity (kBq)
51 mm (avg)	$\simeq$ 5 mm	36.5 ml	1129.67

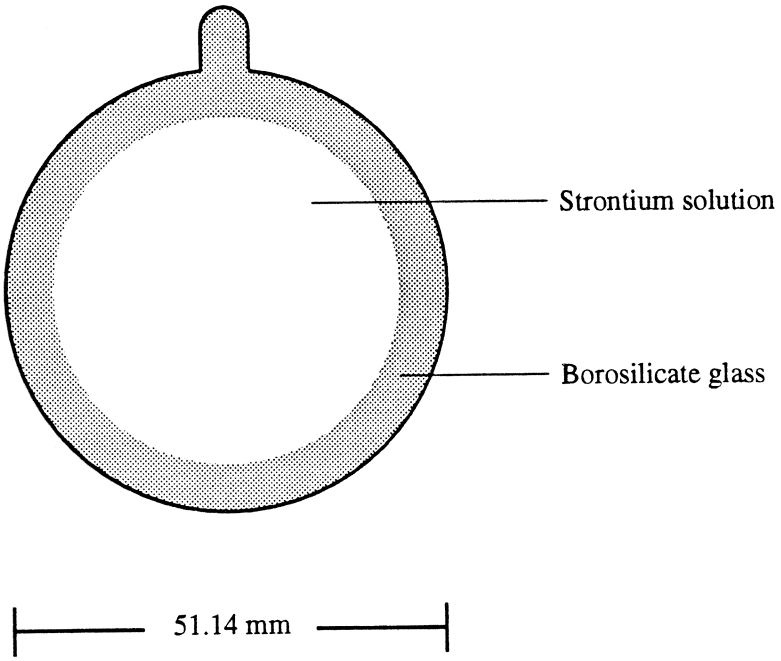

Figure 4.5: The Mark 3 source. The activity of ^{90}Sr is quoted on January 8, 1992.

erage wall thickness approximately 5.0 mm. The source was partially filled with ^{90}Sr dissolved in 0.1 molar hydrochloric acid, and then filled with high-purity water so that air was excluded from the bulb. The source and its construction parameters are shown in Figure 4.5. After filling, the neck of the bulb was sealed by melting the glass near the neck, and the neck was then cut off to leave a spherical bulb. The advantages of this source over the previous ones are that it will incur less radiation damage and it has no significant attenuation of photons for wavelengths longer than about 320 nm. The use of water as a stopping medium ensures no scintillation light (as does acrylic). The activity of ^{90}Sr is over 1 MBq and thus better signal to noise ratios can be achieved in photomultiplier calibration experiments than the previous sources. Since the ^{90}Sr plus carrier materials are left in solution, their optical screening effects are reduced. The main simulation results for this source are shown in the rest of the chapter. The Mark 3 source forms the basis for the most accurate determination of the measurement of photomultiplier counting efficiency reported in this thesis.

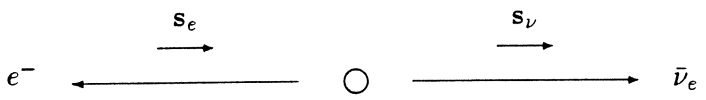

$$\mathbf{S} = \mathbf{s}_e + \mathbf{s}_\nu = 1\,, \mathbf{L} = \mathbf{l}_e + \mathbf{l}_\nu = 1\,, \mathbf{J} = \mathbf{j}_e + \mathbf{j}_\nu = 2$$

Figure 4.6: The vector model of lepton spin coupling for a unique first-forbidden beta decay.

4.3 Beta decay of ^{90}Sr and ^{90}Y

At the beginning of this chapter the motivation for choosing ^{90}Sr was described, and the beta decay properties of ^{90}Sr were illustrated in Figure 4.1. The choice of a γ free decay was made in order to avoid complication of the simulations, and also the radiation hazards of such a source. The transitions shown in Figure 4.1 are essentially free from gamma ray transitions. The largest of these is caused by a $\simeq 0.01\%$ branch of the beta decay of ^{90}Y to a 0^+ level in ^{90}Zr, 1761 keV above the ground state. The nucleus then decays via internal conversion to the ground state with a half life of 61.3 ns. This represents such a tiny fraction of the total transitions that it will be neglected henceforth.

The requirement that the isotope is both long-lived and that the beta decay is energetic are only consistent with the restrictions of increasing phase space at high energies if either the beta decay is strongly forbidden, or that the decay nucleus is a daughter of a longer lived nucleus. For precise work, a strongly suppressed decay is not favoured as the computation of the beta decay spectrum becomes more difficult. Moreover, since no such nuclei with very strongly suppressed high energy beta decays have been found, a long-lived cascade decay is the only possibility. The ^{90}Sr and ^{90}Y beta decays both have first-forbidden spectra which, although not as well known as allowed decays, can be simply computed. This is required in order to compute the light output of Čerenkov sources, and the beta spectra of these decays are described in this section.

An important feature of both ^{90}Sr and ^{90}Y decays is that both transitions have $\Delta J = 2$, in units of $\hbar$, and a parity change in the nuclear wavefunctions. Thus both transitions are forbidden by the selection rules for allowed decays, as the antineutrino-electron pair must carry away at least one unit of angular momentum. The spins of the two final-state leptons are parallel and one of them is in a $p_{3/2}$ state, with angular momentum $l = 1$, and the other is in a $s_{1/2}$ state[6]. This type of beta decay, in which the two final-state leptons have parallel spins, is called 'Gamow-Teller'.

[6]This view is not strictly valid relativistically, when the components of the Dirac spinors have opposite parity for each eigenstate of $\mathbf{j}$. Thus an expansion in terms of the eigenstates of $\mathbf{j}$ is required, see [77].

Since p-wave states have vanishing amplitude at the origin, the matrix element for a transition in which the final leptons carry away angular momentum l is reduced. This can be demonstrated by considering an expansion of the plane-wave approximation of either lepton wavefunction $e^{i\mathbf{k}\cdot\mathbf{r}}$, where $\mathbf{r}$ is the position vector of the lepton and $\hbar\mathbf{k}$ its momentum, see Appendix C. In the case of ^{90}Sr and ^{90}Y, the overlap of the $l = 0$ term vanishes identically, in order to conserve angular momentum. Even for an energetic decay such as ^{90}Y, a typical value of $\mathbf{k}\cdot\mathbf{r}$ is about 0.01, and so decays with final-state leptons with orbital angular momentum $l > 1$ are strongly suppressed. Hence the decay with the spins of both leptons parallel, and the leptons in an $s_{1/2}$ state and $p_{3/2}$ state respectively, is strongly favoured, see Figure 4.6. The contributions from higher order transitions are neglected henceforth, and the computation of the 'first-forbidden' beta-spectrum is thus simplified by the fact that only one matrix element contributes. The spectrum is therefore referred to as unique. In this study only the relative probability density of the decays is required, as the known decay rate is used to normalise the spectrum.

Defining γ to be the total energy of the emitted electron in units of its rest mass energy $m_e c^2$, the relative probability density function $P(\gamma)$ can be expressed as

$$P(\gamma) \sim \gamma' S(\gamma) F(Z,\gamma') (\gamma'^2 - 1)^{1/2} (\gamma_0 - \gamma)^2 , \text{ where } \gamma' = \gamma + \frac{< V >}{m_e c^2} , \qquad (4.2)$$

where γ_0 is the value of γ at the endpoint, $F(Z,\gamma')$ is the correction[7] for the effects of the nuclear Coulomb field. The corrections for the effects of atomic screening on the emitted electron, see Rose [78], are included by correcting γ to γ' by adding the electrostatic screening potential term. An estimate of the average potential $< V >$ can be made from

$$\frac{< V >}{m_e c^2} \simeq \zeta \alpha^2 Z^{4/3} , \qquad (4.3)$$

where Z is the atomic number of the daughter nucleus, and ζ is a model dependent parameter with approximate numerical value of $\zeta = 1.45$, see Durand [79]. For the decay of ^{90}Y, the relevant screening potential $< V >$ is about 5.4 keV, and so γ is increased by about 0.01.

$S(\gamma)$ is the shape correction factor for the unique first-forbidden spectra. For a discussion of the shape factor, see Wu and Moszkowski [80] and the remarks in Appendix C. The form of S can be deduced quite simply for unique decays, as only one matrix element contributes, and always does so via a Gamow-Teller interaction. $S(\gamma)$ can be expressed as

$$S(\gamma) = (\gamma'^2 - 1) + (\gamma_0 - \gamma)^2 . \qquad (4.4)$$

To complete the gross features of the decay spectrum, the relativistic Fermi function is used to correct for the effects of the Coulomb field, see Schopper [81], with the usual form

$$F(Z,\gamma') \sim (1+\delta) (\beta\gamma')^{2(\delta-1)} e^{\pi\nu} \frac{|\Gamma(\delta + i\nu)|^2}{|\Gamma(1+2\delta)|^2} , \qquad (4.5)$$

[7] Often referred to as the Fermi function.

where $\delta^2 = 1 - \alpha^2 Z^2$ and $\nu = Z\alpha/\beta$ where the electron velocity is βc. The complex gamma function is evaluated using the relation

$$|\Gamma(\delta + i\nu)| = \left| \int_0^\infty e^{-\xi}\, \xi^{(\delta+i\nu)-1}\, d\xi \right| = \frac{\Gamma(1+\delta)}{\delta} \prod_{n=0}^{\infty} \left[1 + \frac{\nu^2}{(\delta+n)^2} \right]^{-1/2} . \qquad (4.6)$$

For simplicity the Fermi function (4.5) excludes some factors which do not depend on energy. Note that the Fermi function is valid for unique first-forbidden decays, see Wu and Moszkowski [80] and the remarks in Appendix C. The probability density function of Equation (4.2) can now be computed and a plot of the electron kinetic energy distribution of the beta decay of ^{90}Y is shown in Figure 4.7. A similar spectrum can be computed for the decay of ^{90}Sr, with the relevant endpoint and atomic number.

These probability distributions are sampled in Monte Carlo simulations using the following method. A normalised integral probability function $N(\gamma)$ is generated by integrating the probability density of Equation (4.2)

$$N(\gamma) = \frac{\int_1^\gamma P(\zeta)\, d\zeta}{\int_1^{\gamma_0} P(\zeta)\, d\zeta} . \qquad (4.7)$$

The spectrum is then sampled by inverting Equation (4.7) to find γ for random values of N between zero and one.

Several interactions which affect the shape of the spectrum have been omitted from the simple form of Equation (4.4). In particular the effects of higher-order ($l > 1$) contributions to the spectrum are thought to be small because the expansion $e^{i\mathbf{k}\cdot\mathbf{r}}$ converges quickly. Since second-forbidden transitions do not satisfy the selection rule that the parity of the nuclear wavefunction must not change, third-order corrections are the next (non-vanishing) term in the expansion. Hence the higher-order corrections are suppressed by at least a factor $(\mathbf{k}\cdot\mathbf{r})^2 < 10^{-3}$. The effects of external radiative corrections[8], such as inner bremsstrahlung[9] alter the shape of the beta spectra, but these corrections are believed to be small ($< 1\%$). There are many residual effects caused by interactions with atomic electrons, such as shake-up and shake-off, for a review see Freedman [82]. These too are believed to be negligible as the total shaking probability for the beta decay of ^{90}Y is only 6×10^{-4} per decay.

4.4 Simulation results

Simulations were performed for all three types of source, using both the EGS4 Monte Carlo and an analytic integration method of the type shown in Equation (3.4). However, since the Mark

[8] 'Internal' radiative corrections do not depend on the lepton energies. Only 'external' radiative corrections are dependent on the lepton energies.

[9] Note that inner bremsstrahlung photons also contribute to the flux of ultra-violet photons emitted from the source, but this flux is treated separately from the distortion of the beta spectrum.

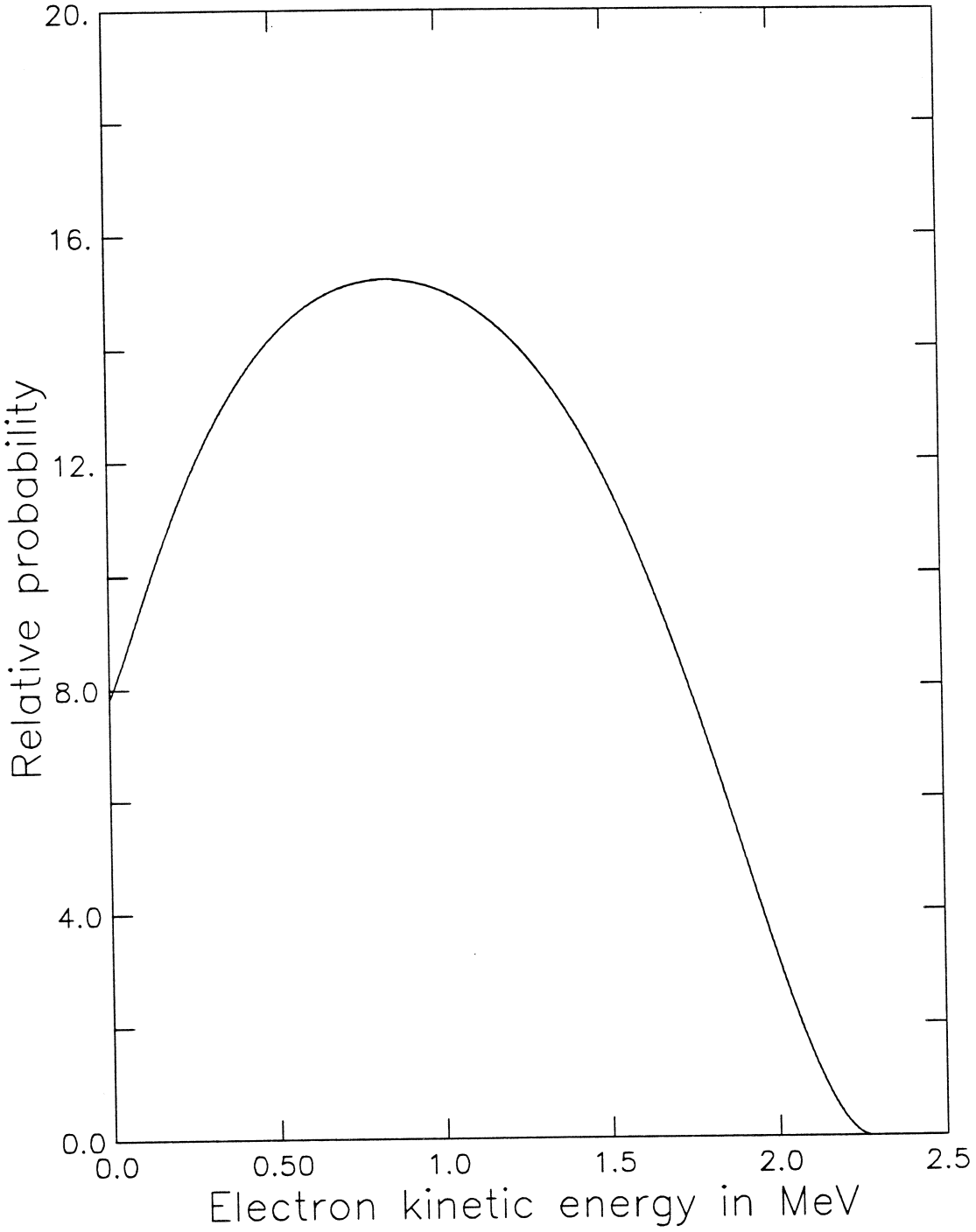

Figure 4.7: The electron kinetic energy spectrum of the unique first-forbidden beta decay of ^{90}Y. Note that this spectrum is sometimes plotted as a function of momentum, in which case the peak is towards the right side of the plot, and the curve passes through the origin.

Decays	$Y \times 10^{14}$	$dY/dn_w \times Y^{-1}$	Mean e^- energy	f_{Sr}
300,000	1.317 ± 0.004	3.30 ± 0.01	572 ± 1 keV	1.4 %

Table 4.4: Results of the Monte Carlo simulation of the Mark 3 source.

3 source has two Čerenkov media, the spatial propagation of the electron is no longer trivial, and simulations of the Mark 3 source can only be computed using the Monte Carlo method. Since the Mark 3 source was used to provided the most reliable estimate of photomultiplier efficiency, and is likely to be adopted as the design for a SNO calibration source, only the simulation results of the Mark 3 source are reported here. The simulation results of the Mark 2 sources are reported in [83].

The Monte Carlo analysis presented here does not explicitly deal with the systematic effects of the variation of refractive index with photon frequency. This approach greatly decreases the execution time and complexity of the computer code. For Čerenkov photons, a non-constant refractive index alters the shape of the Čerenkov spectrum from being constant with respect to frequency to one which rises slowly with frequency. This effect is not negligible for the sources described in this thesis, and if the effect is ignored by choosing an inappropriate frequency at which to evaluate the refractive index, errors of several percent are generated. In the report [83] the spectrum of Čerenkov photons is calculated analytically using a refractive index as a function of photon frequency. It has been found that by evaluating the refractive index at a wavelength of about 400 nm, the errors introduced by a constant refractive index are made sufficiently small (in comparison with other systematic errors). This can be demonstrated qualitatively by observing that both the Čerenkov spectrum and the quantum efficiency of photomultipliers rise sharply towards the short wavelength range of the spectrum of interest here[10]. The value used for the simulation of the Mark 3 source is a value reported in Kaye and Laby [76], which is n = 1.342742, at a wavelength of 404.66 nm. See Figure 4.3. Since less than 10% of the Čerenkov radiation is generated in the glass, its refractive index is not critical to an accurate calculation of the light yield. The value 1.51 ± 0.01 is used.

The results of the simulation predicts the mean yield $Y(\omega)$ of Čerenkov radiation per beta decay electron using Equation (3.3), from beta decays of ^{90}Sr and ^{90}Y in solution within the sphere. Table 4.4 shows the results of the simulation for 300,000 radioactive beta electrons sampled randomly from the ^{90}Sr and ^{90}Y beta spectra, as the two isotopes are assumed to be in equilibrium. Column 3 of the table shows the sensitivity of the yield to the refractive index

[10]Note that the photon spectrum is cut off by a filter at about 370 nm.

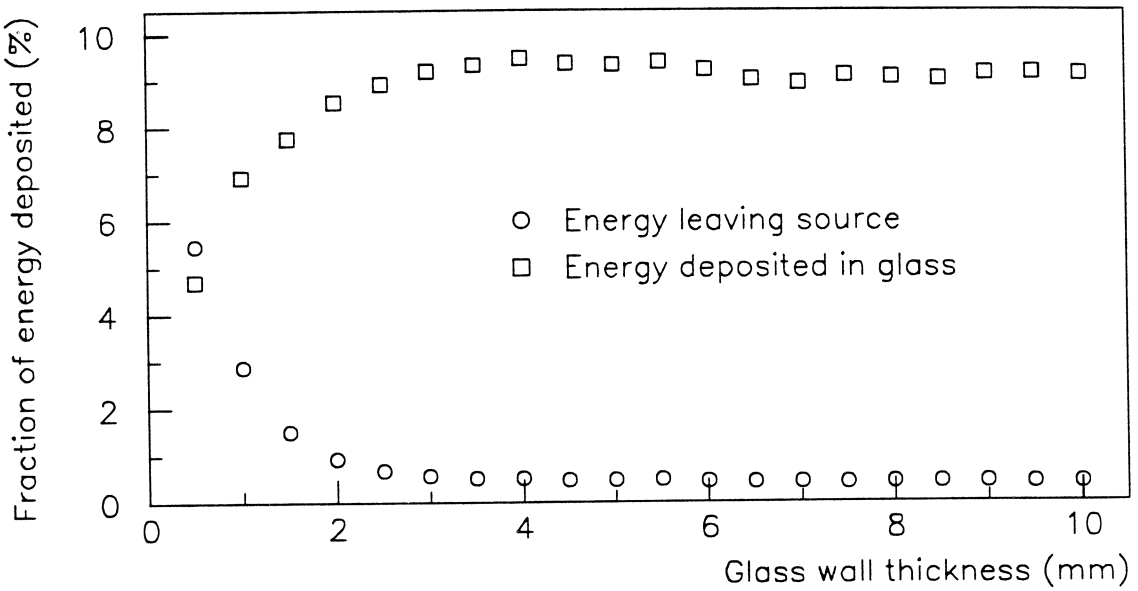

Figure 4.8: Monte Carlo prediction of the radioactive energy deposition.

of water n_w. The fourth column shows the mean electron energy of all the 300,000 decays in the Monte Carlo. The final column shows the fraction of the total Čerenkov radiation which originates from the decays of ^{90}Sr.

In order to address the question of radiation safety, the energy flux of γ-rays leaving the sphere was computed in the simulation. The mean energy leaving the sphere (as electrons or γ-rays) was found to be about 2.5 keV per beta decay. However this value is quite sensitive to the internal parameters used in EGS4 and the proper implementation of the Elwert correction factor, and therefore should be taken as an order of magnitude estimate only. The Monte Carlo code predicts that about 9% of the beta decay energy is deposited in the glass walls of the source. Figure 4.8 shows the mean fraction of the total electron energy that is deposited in the walls of the glass sphere and the fraction that escapes from the sphere as a function of the glass wall thickness. The energy deposition of electrons and bremsstrahlung are both included. It shows that there is no advantage gained from making the glass walls of the source slightly thinner. From the Monte Carlo prediction the radiation dose incurred by the glass can be calculated, and for the Mark 3 source described here the dose is about 50 rads per month.

The study of Adams *et al.* [84] shows the effects of radiation damage (in the range 10^3 to 10^6 rads deposited in one hour) on lead glass. The paper also includes a study of the yield of photoelectrons as a function of exposure to a glass sample between the cathode and a source of Čerenkov radiation. This study indicates that precise work leads to consideration of doses of only a hundred rads, although their experiment was more sensitive to changes in transmission because they used 10 times greater glass thickness than in the Mark 3 source. The lead glass used by Adams *et al.* may also be more susceptible to radiation damage than

Activity	Refractive indices	EGS4	Stopping power	^{90}Y spectrum	Damage	Total
1.5 %	0.5 %	1 %	2 %	1 %	2% (?)	3.5 %

Table 4.5: Contributions to the uncertainty of the Čerenkov light yield from the Mark 3 source.

the borosilicate glass used in the manufacture of the Mark 3 source. From these data one may estimate that radiation damage is not significant for a source made within several months of use. An experimental limit for the optical degradation of less than 1% per month of operation has been established by monitoring the Mark 3 source with a photomultiplier.

The sources of error associated with the final computation of the light output are then listed in Table 4.5. As the values shown are not deduced from the distribution of experimental values there will inevitably be some estimation of the likely uncertainties and most values shown are considered estimates. The activity error comes from the value reported by the manufactures calibration certificate as discussed earlier. The error due to changes in the refractive index over the spectrum is small (0.5 %) as the refractive index used was that corresponding to 404 nm light in water. The EGS4 error figure refers to the total uncertainties from the choice of internal parameters and statistical processes in the Monte Carlo calculation. The error labelled ^{90}Y spectrum refers to the uncertainties in the shape of the spectrum and its end point energy. The figure for the error in light yield due to radiation damage is a (conservative) estimate for a time of 2 months based on the data of Adams *et al.*

The estimate of the total uncertainty assumes that the errors listed in the table are randomly distributed with respect to one another and that other errors are small. The conclusion of this simulation is that the absolute value of the yield of Čerenkov radiation from the Mark 3 source can be computed to about 3.5 % accuracy. Some systematic error will be caused by deviations from true spherical symmetry of the glass bulb of the Mark 3 source. The experimental significance of this effect will depend on the refractive index of the external medium and the counting geometry. In water, where the glass/water refraction is small, the anisotropy of the source is believed to be less than 1%.

The graphs in Figure 4.9 show a sample of electron energies used in the Monte Carlo, and the yield of Čerenkov radiation produced as they stop in the solution and/or the glass envelope. Figure 4.10 shows a two dimensional projection of the paths of beta decay electrons in the source.

The small contribution to the photon spectrum from internal bremsstrahlung can be ap-

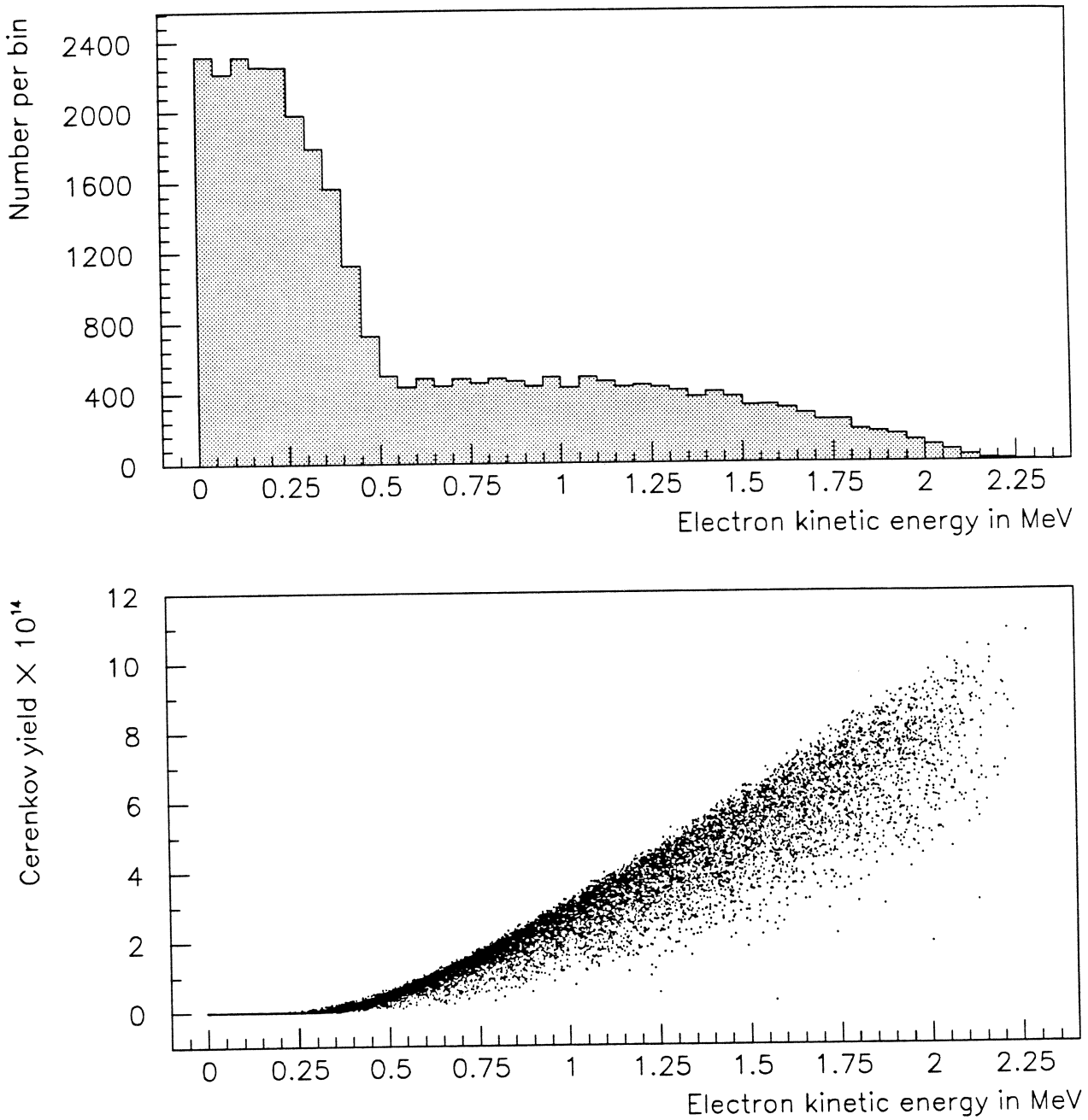

Figure 4.9: The upper histogram shows a spectrum of initial electron kinetic energies from the beta spectra of ^{90}Sr and ^{90}Y. The scatter plot shows the yield of Čerenkov radiation from electrons of various energies.

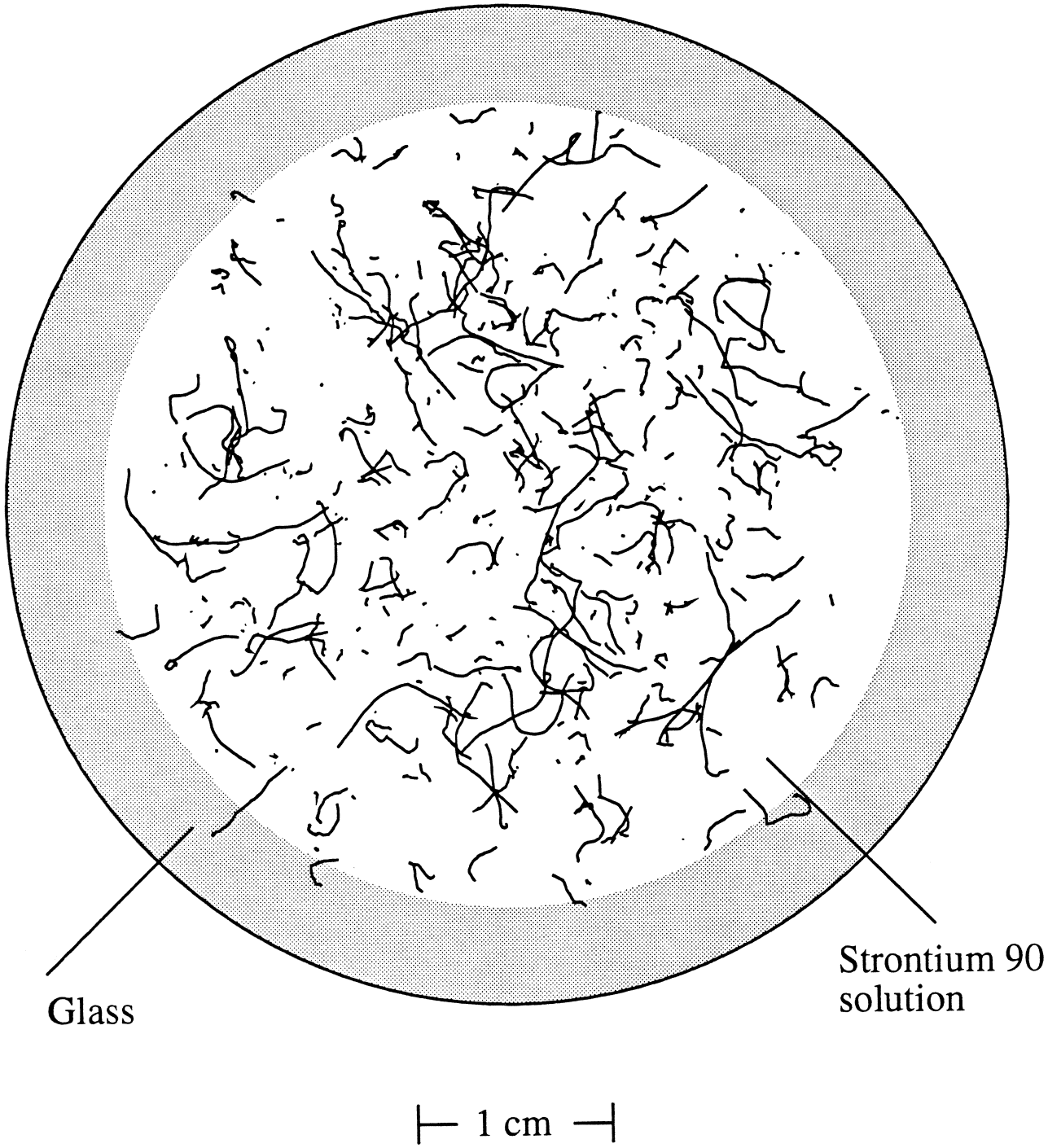

Figure 4.10: Projection of beta decay electron trajectories in the Mark 3 source.

proximated by

$$\frac{dN}{d\omega}(\beta,\omega) = \frac{\alpha}{\pi\omega} f(\beta) , \tag{4.8}$$

where $f(\beta)$ is a model dependent function of the initial electron velocity βc. This function $f(\beta)$ is of order unity for relativistic beta decays, and vanishes as $\beta \rightarrow 0$. At wavelengths in the ultra-violet region, the contribution from the internal bremsstrahlung photon spectrum is about 4 orders of magnitude below the Čerenkov light output shown in Table 4.4, and so no correction is made. In a similar manner the photon flux from external bremsstrahlung can be shown to be negligible for these sources.

Chapter 5

Photomultiplier efficiency

To achieve agreement between the experimental energy calibration of the response of the SNO detector with a Monte Carlo prediction requires that the net efficiency of the photomultipliers for detecting photons is known. The efficiency of a photomultiplier can be factorised into two distinct quantities, according to the physical processes by which the photomultiplier works. The probability that an incident photon will liberate a photoelectron is known as the Quantum Efficiency of the photocathode. The quantum efficiency is widely quoted as a measure of photomultiplier efficiency, largely because it is comparatively easy to measure. However the efficiency of counting these single photoelectrons by the rest of the photomultiplier and associated electronics is not widely quoted as it is rather difficult to measure. This latter efficiency is dependent on the photoelectron collection efficiency of the first dynode and the fraction of anode pulses above a chosen discriminator level. The work presented in this chapter includes measurements of both the quantum efficiency and photoelectron counting efficiency of photomultipliers.

The quantum efficiency is defined as the probability that a photon incident on the photocathode will scatter an electron into an unbound continuum state and that this photoelectron will leave the photocathode[1]. The quantum efficiency is comparatively easy to measure as relatively intense illumination from a filament or discharge lamp can be used. Typically a photocathode surface is illuminated by about 0.1 mW and this liberates photoelectric currents between 10 and 100 μA/mW for visible light. The method of measuring the quantum efficiency is simply to measure the photoelectric current produced from incident light of known intensity and wavelength. The principal difficulty associated with this measurement is the estimation of the intensity of the incident light.

The efficiency of counting single photoelectrons is difficult to measure as calibrated light sources of low enough intensity are not commonly available. Several different approaches

[1]For a discussion of the experimental properties of the photoelectric effect see the remarks in Appendix D, and the comprehensive discussion by Sommer [85]. The latter covers the K_2CsSb bialkali photocathode which is used in the photomultipliers discussed in this thesis. The optical properties of this photocathode have been measured by Moorhead and Tanner [86].

to resolving this problem have been made; for example measuring the cathode photoelectric current with the photomultiplier close to a light source, and then pulse-counting with the photomultiplier far from the source assuming an inverse square dependence of the intensity as a function of distance. A related method is to use neutral density filters to achieve the same attenuation. The former method is rejected here as the angles of incidence on the photocathode of light from the source are rather different at different distances. The latter is rejected as the attenuation of the light source, by a factor 10^9, must be known at all wavelengths of interest at the few percent level. Also the difficulty of measuring very small photoelectric currents led some early workers in the field to deduce (incorrectly) small values of the single photoelectron counting efficiency.

Clearly this latter measurement is non-trivial, but several authors [87, 88, 89] claim to have achieved accurate results with this technique. They deduce single photoelectron counting efficiencies in the range 60-80%, although the precise value depends on the operating conditions of the photomultiplier and the discriminator level. It should be noted that these methods (unlike the one described below) do have the attractive feature that the quantum efficiency is not required.

If a low intensity light source is available then efficiencies can be estimated provided that the intensity of the source is well known at all wavelengths of interest. Two such approaches are used; one is to use Čerenkov radiation using the techniques described in the previous chapter. The other is to use the well-known black body radiation spectrum from a hot object. This latter approach is most often used at standards laboratories. The black body spectrum is given by the Planck formula

$$\frac{dN}{d\omega}(\omega) = \frac{\omega^2}{\pi^2 c^3 \left(e^{\hbar\omega/kT} - 1\right)}, \tag{5.1}$$

where N is the photon number density produced by a black body of absolute temperature T. The maximum value of this photon spectrum occurs when $\hbar\omega/kT \simeq 1.59$. This implies that a rather high temperature (10^4 Kelvin) is required if the spectrum is to be matched to the response of a bialkali photocathode which peaks in the ultra-violet. Furthermore, the light output is usually far too intense for photomultipliers to count single photons. However, this technique is often used to calibrate quantum efficiency measurements.

The technique used in this work is to predict a count rate based on the measured quantum efficiency of the photocathode and the known intensity of the Čerenkov radiation source described in the previous chapter. The ratio of the predicted count rate to that observed experimentally is then a measure of the counting efficiency of the photomultiplier and its associated electronics. For any given photomultiplier this efficiency η will be a function of the voltages applied to the dynodes (and hence the gain), the discriminator threshold, and the area of illumination of the photocathode. The efficiency parameter η is then interpreted as

the probability that a single photoelectron will be registered as a count. With this in mind, the count rate R will then be

$$R = 2\pi\eta c A\Omega \int_{300\text{ nm}}^{700\text{ nm}} Q(\lambda)T(\lambda)\left(\frac{dN}{d\omega}\right)\frac{d\lambda}{\lambda^2}, \tag{5.2}$$

where Ω is the solid angle subtended by the photocathode at the source, A is the source activity, and $dN/d\omega$ is the mean source intensity per beta decay. The factor $2\pi c$ arises from the transformation of the source intensity from a function of frequency to wavelength. The quantum efficiency of the photocathode is labelled as $Q(\lambda)$. In order to define the short wavelength cutoff of the source, a piece of acrylic of known transmission $T(\lambda)$ is placed between the source and photocathode, and so its attenuation must be accounted for. In the rest of this chapter the complementary measurements of both the quantum efficiency and photoelectron counting efficiency of several photomultipliers, similar to those to be used in the SNO detector, are described. These quantum efficiency experiments were carried out by the author at the Thorn EMI research and development facility in Ruislip, Middlesex and the photoelectron counting experiments were performed in Oxford.

5.1 Quantum efficiency measurements

The apparatus at Thorn EMI Ruislip uses two photosensitive devices which are calibrated annually by the National Physical Laboratory over the wavelength range 240 nm to 1100 nm to provide the appropriate normalization. These two devices are; a 50 mm photomultiplier, for shorter wavelength light, and a photodiode for longer wavelength measurements. These devices are calibrated using a mercury discharge line at 546.1 nm with a standard deviation of 0.8%. The calibration at other wavelengths is relative with a 1.0% standard deviation (2.0% above 1040 nm). These errors will give systematic uncertainties in any quantum efficiency measurements made relative to these standards.

The apparatus is based on two discharge lamps as the sources of light, a monochromator, and two calibrated photodiodes. The experimental method consists of estimating the photoelectric current incident on the dynode stack and relating it to the estimate of the radiation incident on the photocathode. It is assumed that all liberated photoelectrons are detected with this measurement. The photomultiplier is wired so that the cathode is maintained at -360 volts relative to the dynode stack, which is kept grounded so that the anode current can be measured easily.

For measurements with wavelengths of 360 nm and above, a Tungsten filament lamp is used; below 360 nm a Deuterium discharge lamp is used. A computer is used to control the experiment and take the relevant data. A source blocker is used to measure the background, which is then subtracted. The quantum efficiency is estimated in percentage terms at intervals

Source of error	Type of error	1 σ error
Calibration for $\lambda < 1040$ nm	Systematic	1%
Ammeter and photodiode calibration	Systematic	$\simeq 1$ %
Current measurements	Random	1%

Table 5.1: Uncertainties in the quantum efficiency measurements.

of 10 nm between 240 nm and 1040 nm. In practise 700 nm is the upper limit for any useful measurements for bialkali photocathodes. There is no magnetic field compensation or shielding employed in this apparatus, but it is argued that since all photoelectrons are collected by virtue of the counting technique, none is necessary anyway. This assumption is consistent with the results shown here.

A brief summary of the uncertainties in the EMI method is shown in the Table 5.1. The errors quoted in this table refer to the percentage of the measured efficiency and, if the systematic errors are not correlated, the total systematic error is about 1.4% per data point. The contribution from the random measurement errors is likely to be negligible when computing the integral in Equation (5.2), as many points are included. Inconsistencies between measurements can be introduced by the choice of position and size of the light spot incident on the photocathode. These are not necessarily errors since the quantum efficiency may not be constant over the photocathode, and the angle of incidence is a function of position. Thus any results should be interpreted as an average over the illuminated area. This is the largest source of discrepancy between the results that appear in this section. For the purposes of quantum efficiency measurements the collection efficiency of the photoelectrons is taken to be 100%. The electron collecting surfaces are not only the first few dynodes, but also the metal surfaces surrounding the dynodes. Any deviations from this assumption will tend to reduce the measured quantum efficiency. One method of estimating the error associated with loss of photoelectrons is to alter the potential between cathode and dynode stack.

Six measurements of quantum efficiency of an EMI 9351 photomultiplier were taken to investigate both random and systematic effects. They consist of a series of measurements of the quantum efficiency as a function of wavelength in the appropriate range for the source used. Table 5.2 gives a summary of the quantum efficiency measurements of this photomultiplier, serial number 1019, which has a borosilicate glass front window coated with a bialkali photocathode.

The results of these measurements are shown in Figure 5.1. They clearly show the small

Run No	Source	Spot size	Volts K-D1	Test aim
1	Tungsten	150 mm	360	Normal test conditions
2	Deuterium	150 mm	360	Short wavelength test
3	Deuterium	150 mm	360	Repeat of Run 2 for random fluctuations
4	Tungsten	150 mm	360	Repeat of Run 1 for random fluctuations
5	Tungsten	150 mm	540	Electron collection effects
6	Tungsten	115 mm	360	Spot size variation

Table 5.2: Quantum efficiency measurements of an EMI 9351 photomultiplier (S/N 1019).

nature of the random errors. The data from the two sources are consistent at the cross-over wavelength of 360 nm. The cutoff in quantum efficiency at about 300 nm is due to the transmission of the glass of the front window of the photomultiplier. The potential between the cathode and the first dynode seems to have little effect at the level of the 1% random errors, although there is marginal evidence that the quantum efficiency deduced from Run 5 is slightly higher than previous runs. However, the data were consistent with the assumption that a very large fraction of the photoelectrons are counted. The spot sizes and positions were not changed during Runs 1 to 5, but the spot size was made smaller for Run 6. Run 6 shows a significant decrease (about 2%) in the measured values of quantum efficiency at all wavelengths. This is interpreted as the variation of the quantum efficiency over different parts of the photocathode.

The quantum efficiency results for the various photomultipliers tested for efficiency in this thesis are shown in Figure 5.2. These data were subsequently used to compute the integral in Equation (5.2) separately for each photomultiplier. Two Hamamatsu photomultipliers from a pre-production batch, made from borosilicate glass, are shown in the upper graphs of Figure 5.2. (Note that photomultiplier manufacturers use a type number to identify a family of similar but not identical photomultipliers.) Clearly the quantum efficiency, shown in the lower left graph, has improved in photomultiplier CB0274, which is of the type to be used in the SNO detector. This photomultiplier has a Schott 8246 glass bulb. For comparison an EMI 9350 photomultiplier, similar to those used in the MACRO experiment [90], is shown in the lower right graph.

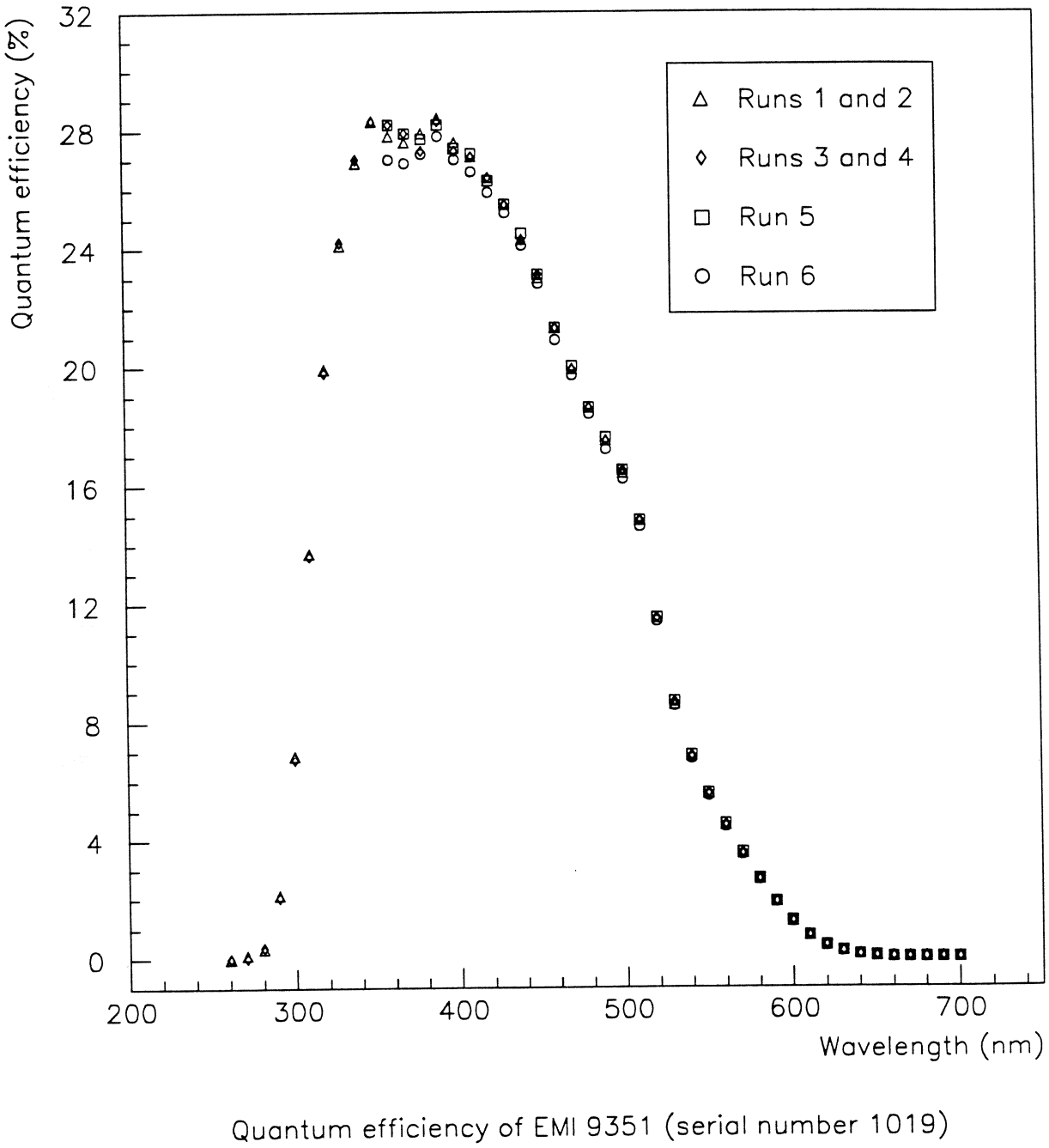

Figure 5.1: Quantum efficiency measurements of an EMI 9351 photomultiplier, serial number 1019. The six runs look for variations due to random and systematic effects. Details are given in the text.

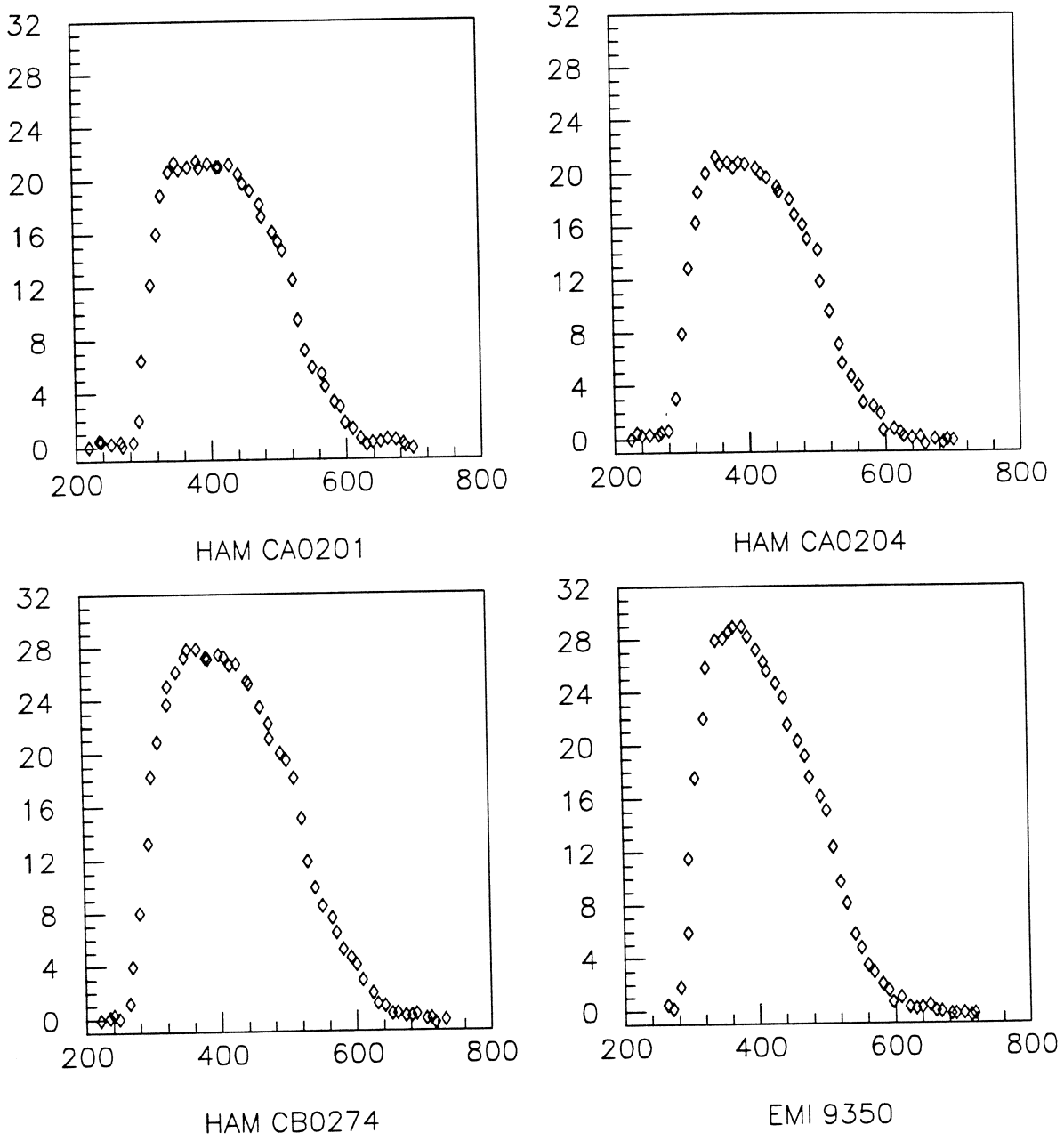

Figure 5.2: The upper two graphs show the quantum efficiency (%) of two pre-production Hamamatsu SNO photomultipliers. The lower left shows a Hamamatsu production SNO photomultiplier made with a Schott 8246 glass bulb. An EMI 9350 is shown on the lower right for comparison.

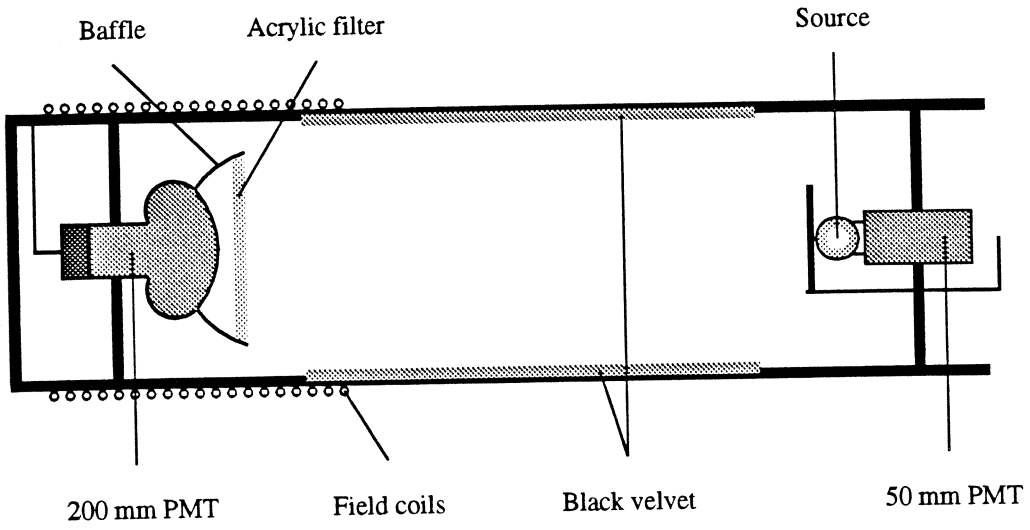

Figure 5.3: The Mortar apparatus (not to scale).

5.2 The Mortar experiment

The absolute efficiency measurement of a photomultiplier requires that the flux of photons arriving at the photocathode is known accurately in the experimental arrangement employed. Not only should the source brightness be well known, but also the fraction that hits the photocathode, either directly or via reflections. The approach taken in this work is to ensure that only direct (not reflected) photons are counted. An apparatus, known as the 'Mortar', was constructed to satisfy these conditions and allow a measurement of the rate of counting of single photoelectrons from a source of known brightness.

The Mortar is based on a Tufnol cylinder of internal diameter 405 mm, which is coated inside and out with matt black electrically conductive paint to reduce radiofrequency interference. At one end of the Mortar the 200 mm photomultiplier is mounted with a matt black baffle, which serves to shield the photocathode from reflected light. The baffle also serves to define the area, and hence the solid angle subtended by the photocathode to the light source. The diameter of the baffle at the photocathode is 186.5 ± 0.1 mm, and the distance from this diameter to the centre of the source is typically 1.5 m, depending on the photomultiplier used. The baffle also holds an acrylic panel which serves to filter out short wavelength photons ($\lambda < 370$ nm) emitted from the source. The correction for the reflections from the photocathode and subsequently back from the acrylic filter increases the signal by about $\simeq 1\%$, and this is subtracted. A simplified picture of the Mortar is shown in Figure 5.3.

The Mark 3 source described previously is mounted on a Hamamatsu R1828-01 photomul-

tiplier at the other end of the Mortar[2]. When performing absolute efficiency measurements a layer of black velvet is placed between the source and this monitor photomultiplier to avoid unwanted reflections. Black velvet is also used to line the central section of the Mortar, and other vulnerable regions, where reflections are particularly problematic. The velvet used is found to have particularly low reflectivity when the fibres (known as the nap) are brushed towards the light source, and so the velvet was brushed away from the 200 mm photomultiplier prior to installation in the Mortar. The source blocker, also lined with black velvet, is used to block the light when measuring the background noise signal from the photomultiplier. The source blocker is designed so that only photons travelling directly from the source to the photocathode are blocked. Hence any light which arrives at the photocathode by reflections is subtracted away as background.

The Mortar was wound with field coils passing a known d.c. current to cancel the local magnetic field. The coils extend 62 cm along the length of the Mortar and are centred on the region between the cathode and first dynode of the Hamamatsu R1408 photomultiplier. Cancellation of the local magnetic field achieved by orienting the Mortar along the line of the local field and then adjusting the current in the coils so that the field in the region of the large photomultiplier was cancelled. A fluxgate magnetometer was used to aid both the orientation of the Mortar and the adjustment of the current in the field coils. The current in the field coils was 420 mA and was monitored continually throughout the data taking period. The residual fields in the region of the large photomultiplier were of order 0.3 μT. It was difficult to reduce these further due to the inhomogeneities of the field from the coils, principally from edge effects. However, this reduction factor is adequate to ensure that magnetic fields have a negligible effect on the photomultiplier counting rate. The low sensitivity of the photomultiplier count rate to changes in the current in the field coils, and hence magnetic field, is demonstrated in the following chapter.

The electronic hardware used for counting of single photoelectron pulses from a photomultiplier under test is shown in Figure 5.4. As in the SNO detector a single cable was used for both the high voltage supply to the photomultiplier and to transmit the charge pulses from photoelectrons. The signals were filtered from the high voltage supply by a simple resistor/capacitor circuit and then amplified.

A LeCroy 612A amplifier, with a bandwidth of about $\simeq$ 200 MHz and a charge amplification factor of 9.9$\pm$0.1, was used. The amplifier is known to be quite linear provided that the internal rail voltage (5V) is not exceeded. In practice output pulses should not exceed about 4.5 volts

[2]The Hamamatsu R1828-01 is a 12 stage device with a bialkali photocathode of 51 mm diameter coated onto borosilicate glass. The dynodes are also coated with bialkali and are arranged in a linear focus design. The monitor photomultiplier is encased in its own magnetic shield (Hamamatsu case number H1949). The transit time spread of signals from the R1828-01 is about 0.25 ns (1 standard deviation) according to the manufacturer. This claim is backed up by experimental TDC data showing a peak consistent with this width.

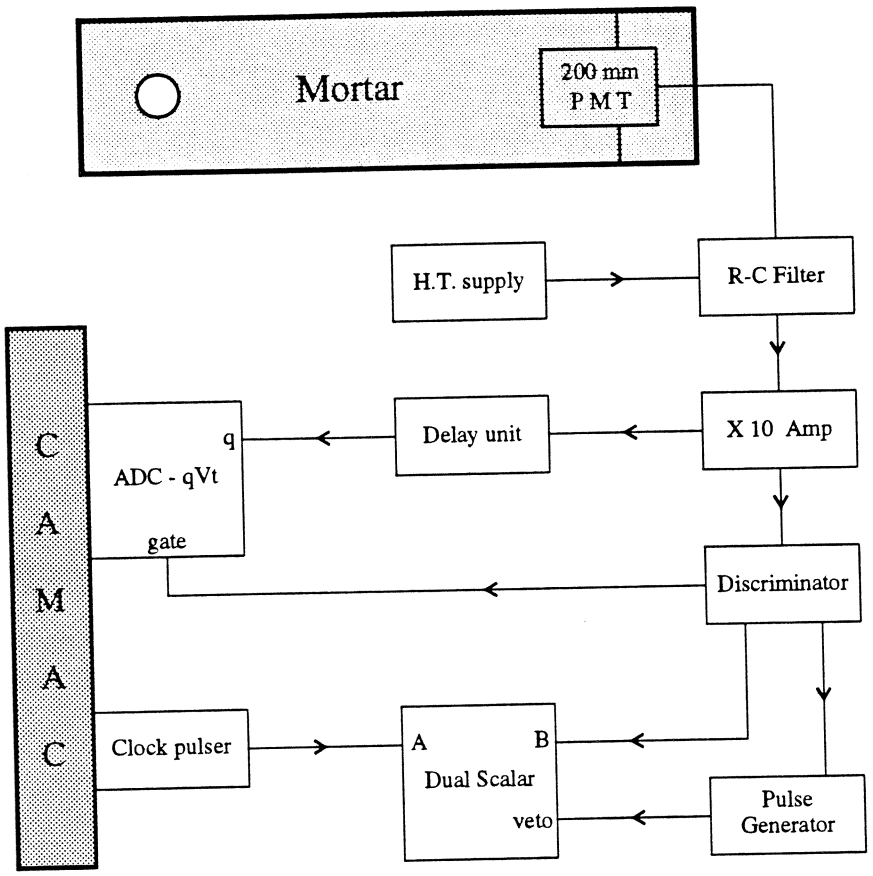

Figure 5.4: The Mortar electronics for single photoelectron counting.

if the linearity of the amplifier is to be relied upon. It was found that the output of the amplifier contained a positive d.c. offset voltage of several mV which was filtered so that the discriminator input was not biased. Each amplifier channel had a fan-out to two independent outputs. One output of the amplifier triggered an EG&G Ortec Constant Fraction Differential Discriminator, model 583. This discriminator was required for measurements of transit time spread, which are discussed in the following chapter.

The charge spectrum of pulses from the photomultiplier was measured by an analogue-to-digital converter (ADC) which is fed from the second amplifier output. The ADC used was a LeCroy 3001 Multichannel Analyzer, commonly known as a qVt. Linearity at the $\simeq$ 1% level was verified by a simple test of applying a constant voltage to the charge input and varying the time of integration. It was found that the pedestal charge varied according to the duration of the integration time (probably due to an input bias current in the ADC preamplifier), but once this was allowed for good linearity was restored. Thus the pedestal channel of the ADC was measured before any charge spectrum was taken[3]. The ADC was interfaced via a CAMAC dataway (IEEE-583) to a VAX 4300 computer for analysis of the

[3]This was done by connecting a 50 Ω termination to the ADC input and noting the count channel.

data. The monitoring by the ADC of those signals which triggered the discriminator provided an accurate and independent measurement of the discriminator charge threshold as well as the charge deposited by a photomultiplier signal.

The charge distribution usually has a single pronounced maximum, which is referred to as the 'single photoelectron peak'. Depending on the material used to coat the first dynode, this peak can be quite sharp. The origin of this effect is probably the statistical fluctuations of the number of secondary electrons emitted by the first dynode, and so a photomultiplier with higher first dynode multiplication usually has good charge resolution. A convenient expression of the sharpness of the peak is to quote the ratio of counts in the peak channel to that of the trough on the low charge side of the peak. This peak-to-valley ratio can be as high as 3:1 for gallium phosphide coated dynodes, although 2.5:1 is more typical for dynodes coated with caesiated antimony (CsSb), and 1.5:1 for oxidised beryllium copper (BeCu). The quantity of interest is the amount of charge deposited by a single photoelectron, and not produced by a noise pulse. The latter can be avoided by counting in coincidence with a small photomultiplier. In this work the modal charge per photoelectron is quoted, although in other work the mean charge is sometimes quoted. These precise definitions lead to slightly different deduced gain values, typically 10% different. This effect should be kept in mind when comparing results.

In the SNO detector, only prompt photomultiplier signals (within 100 ns) from a relativistic electron will be interpreted as being Čerenkov photons and thus analyzed by the event fitting routine. Any following time-correlated signals, known as afterpulses, must be ignored, and so these must be subtracted from the signal rate observed in the Mortar counting experiment. The afterpulsing phenomenon is discussed in greater detail in the following chapter. There are two ways of making the percent level correction for afterpulsing, either by subtraction after the count, or by a hardware veto. The latter approach is used here by turning off both scalers (clock and photomultiplier pulse counting) for a fixed period which is short compared to the interval between pulses (200 μs) and long compared to the afterpulse time (1 μs). A time of 30 μs was chosen.

The net count rate of a photomultiplier was deduced by a series of 10 second counts with the source OFF, ON, ON and OFF. This series is repeated about 20 times at each discriminator setting. This procedure has several advantages over a lesser number of longer runs. Firstly the noise subtraction is effectively done throughout the experiment, rather than at the end or beginning. Secondly the distribution of the net signals from these series of counts provides statistical information about the reliability of the result. This procedure was used to obtain the data on the single photoelectron counting efficiency shown in the following section.

Component	R1	R2	R3-R11	R12	R13	R14	R15	C1-C3	C4
Value	5M	3M	1M	500R	200R	50R	100K	10n	4n7

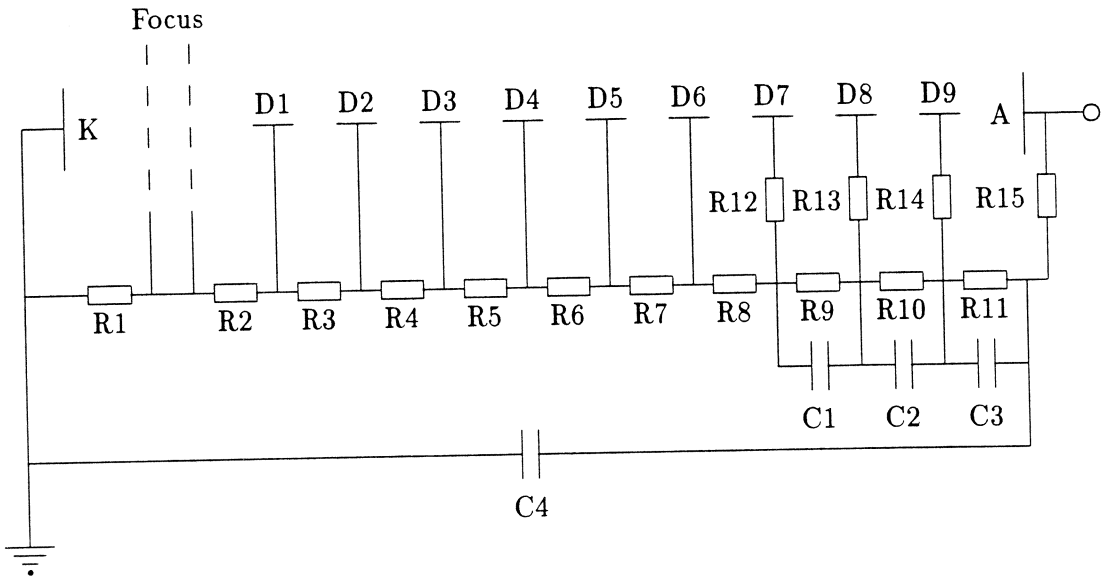

Figure 5.5: The circuit diagram for the SNO photomultiplier base.

5.3 Single photoelectron counting efficiency

The single photoelectron counting efficiency of a photomultiplier, as defined by η in Equation (5.2), is deduced from the results of measurements in the Mortar apparatus. The results are presented in this section, but several remarks on the interpretation of these results should be made. Firstly it is unwise to extrapolate the data to other conditions, for example to a different photocathode area, discriminator levels or gain. The photoelectron collection efficiency is weighted by the Čerenkov spectrum of the source used, and may depend on the incident photon wavelength. Secondly, this measurement should not depend on the quantum efficiency as that is divided out using Equation (5.2). Errors in the measured quantum efficiency will affect the results thereby obtained, but the *product* of the quantum efficiency and photoelectron counting efficiency is invariant of errors in the overall normalization of the quantum efficiency measurement.

The first single photoelectron counting efficiency experiment was performed on a Hamamatsu R1408 photomultiplier, serial number CB0274, with the current SNO voltage divider base. The base circuit is shown in Figure 5.5. The photomultiplier was used at a similar operating point (gain and dynode voltage distribution) as it is expected to be in the SNO detector. The discriminator level was determined from an ADC spectrum of the charge deposited by

those pulses which triggered the discriminator, and a separate spectrum was taken for each discriminator setting. The results of a typical ADC spectrum are displayed in Figure 5.6, along with the single photoelectron counting efficiency as a function of discriminator level. The ADC spectrum shows the number of counts per channel, where the charge sensitivity is 0.25 pC/channel, and the offset is +1 channel. The ×10 amplifier is included so that the peak of the spectrum corresponds to a photomultiplier gain of 10^7, as in the SNO detector. The points plotted in the lower graph of Figure 5.6 show the single photoelectron counting efficiency as a function of the discriminator level, expressed as a fraction of the single photoelectron peak in the charge spectrum. The error bars on the lower plot show the random errors deduced from the experiment, but there is an overall systematic error of about 3.5% from the Čerenkov source, and about 1.4% from the quantum efficiency measurement.

This deduced single photoelectron counting efficiency is quite low, however this photomultiplier was optimized to have small transit time spread. Like many other photomultipliers in this class, this is believed to have been achieved by a reduction in the size of the first dynode, and hence electron collection is reduced. Also this photomultiplier does not have good charge resolution and so the fraction of small pulses below the discriminator level will be significant. This should now be compared to a result from a photomultiplier designed for maximum single photoelectron collection which has good charge resolution. In the next experiment the gain and voltage between cathode and first dynode was allowed to vary, and the discriminator level was reduced, in an attempt to maximize the signal. This will put a useful experimental lower limit on the source light output by assuming that the photoelectron counting efficiency η cannot exceed 100%.

The second single photoelectron counting efficiency experiment was performed on an EMI 9350 photomultiplier, serial number 6460. This photomultiplier has 14 dynodes coated with CsSb arranged in a linear focus design. The charge spectrum of pulses from the photomultiplier was recorded as a function of gain and voltage between cathode and first dynode but the results are discussed in detail in the next chapter. This photomultiplier was optimized for the MACRO cosmic ray air shower experiment which required high efficiency and good linearity. The charge resolution of the device is quite good, and a typical ADC spectrum is shown in Figure 5.7, with the discriminator level set at about channel 5. In order to maximize the counting efficiency the discriminator was set to the lowest possible value of about 1/16 of a single photoelectron charge. This case is particularly interesting as the discriminator approaches unit efficiency for counting signals from the photomultiplier, and so the deduced counting efficiency reflects the ability of the photomultiplier to count single photoelectrons. Increasing the gain has a similar effect to decreasing the discriminator level, but the former was chosen for reasons of stability and convenience.

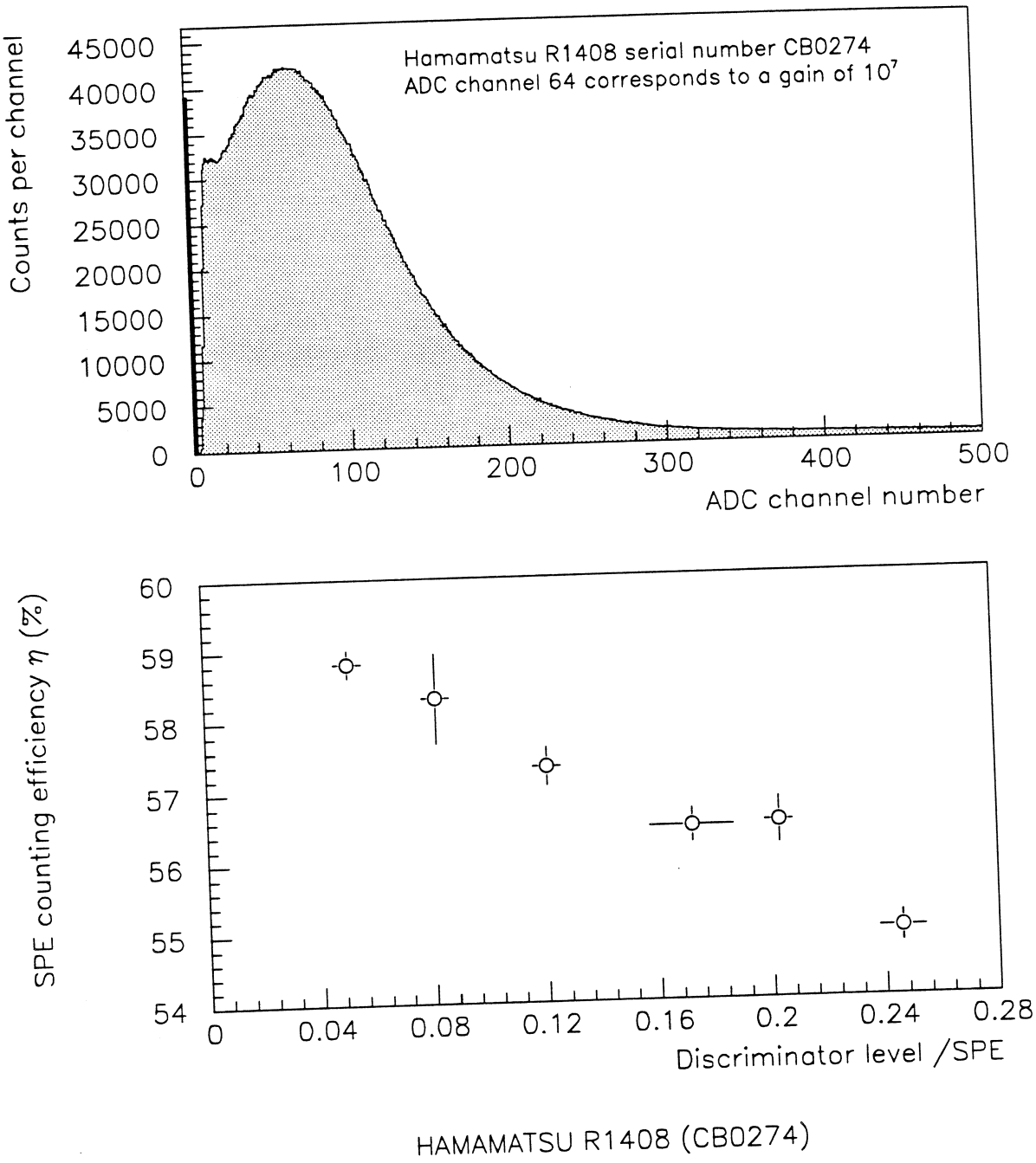

Figure 5.6: Hamamatsu R1408 photomultiplier (CB0274). The upper charge spectrum shows the discriminator level at about ADC channel number 5. The lower graph shows the deduced single photoelectron counting efficiency η as a function of discriminator level.

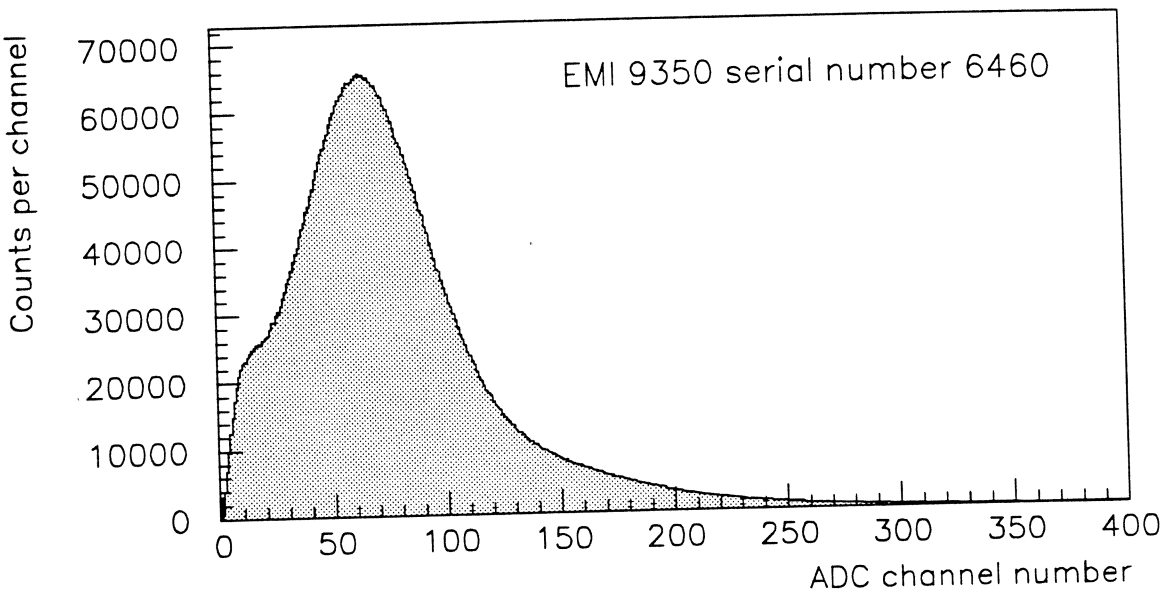

Figure 5.7: The single photoelectron charge spectrum of an EMI 9350 photomultiplier.

The histogram in Figure 5.8 shows the deduced single photoelectron counting efficiency on the vertical axis, with gain shown on the left axis and voltage between cathode and first dynode shown on the right hand axis. The discriminator was fixed at about 1/16 of a single photoelectron charge. The random error on each histogram bin height is of order 1%, and there is an overall normalization error of about 3.5% due to the source intensity, and about 1.4% from the quantum efficiency measurement. The graph clearly shows the monotonic rise of single photoelectron counting efficiency with gain and voltage between cathode and first dynode. Increasing the gain of the photomultiplier will certainly increase the number of counts above the fixed discriminator level, but the effects of increasing the voltage between cathode and first dynode can only be attributed to the collection efficiency of the first dynode and the statistics of secondary multiplication at the first dynode. The largest efficiency recorded here, about 87 $\pm$ 4%, sets a useful lower limit on the light output of the Mark 3 source.

The values of photoelectron counting efficiency reported here are dependent on the discriminator threshold when compared with the average charge deposited by an anode pulse. It is clear that the photoelectron counting efficiency of a photomultiplier is also dependent on the operating conditions used. Despite these variations, the range of values reported in this thesis is consistent with most other measurements, although the values for the photoelectron counting efficiency of the Hamamatsu R1408 are lower than expected.

Foord *et al.* [91] have reported small values of the single photoelectron collection efficiency η. Their values for two photomultipliers, 29% and 18%, have been challenged by several authors, for example Young [92], and it is now accepted that their measurement of the very small photocathode current was incorrectly interpreted as being solely photoelectric in origin.

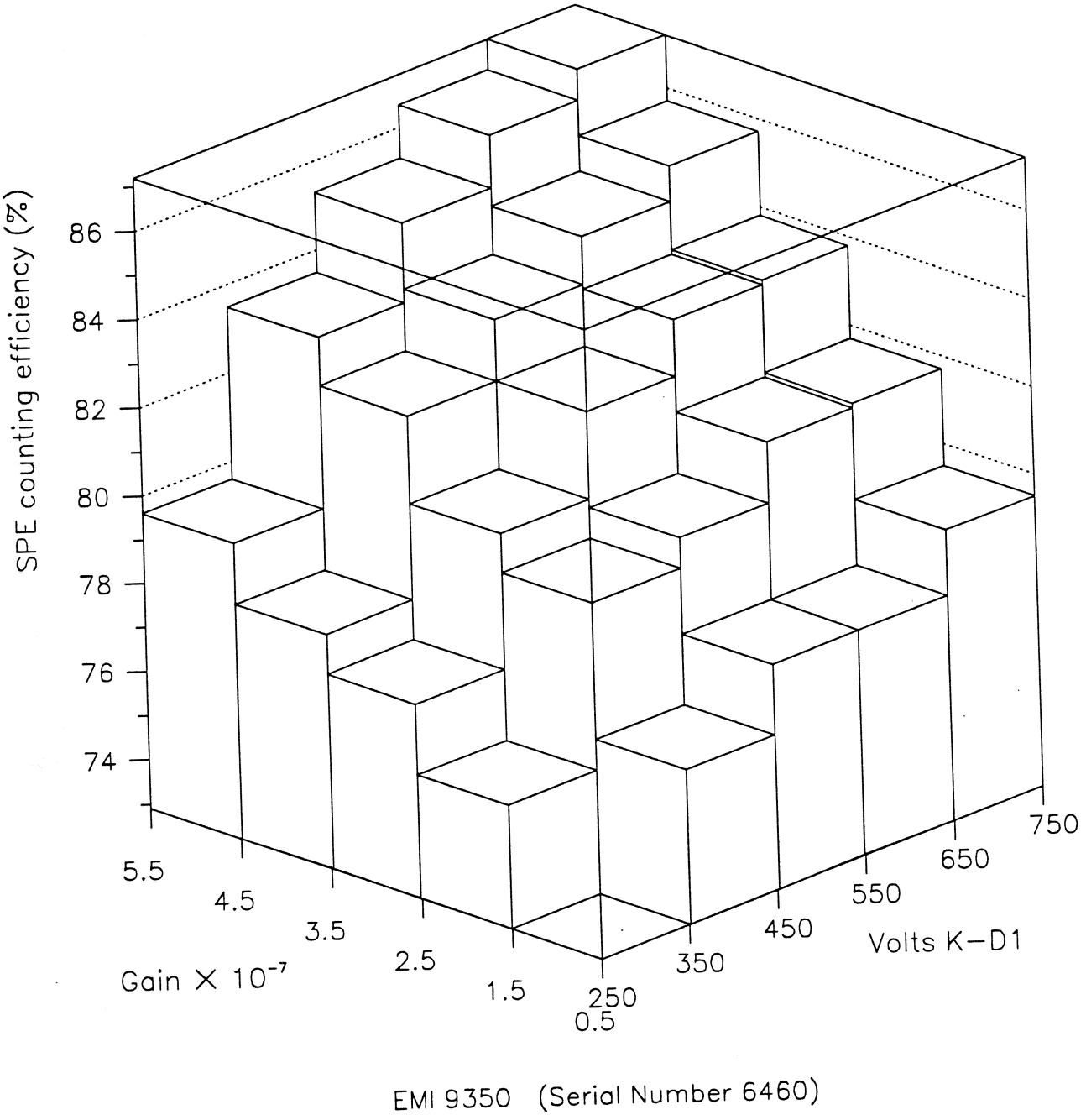

Figure 5.8: The single photoelectron counting efficiency η (%) of an EMI 9350 photomultiplier (serial number 6460) is shown on the vertical axis. Gain is plotted on the left hand axis in units of 10^7 and the voltage between the cathode and first dynode is shown on the right hand axis.

Group	Method	Photomultiplier	η
Foord *et al.* [91]	Signal/noise-in-signal	EMI 9658	0.29
		ITT FW130	0.18
Lakes and Poultney [87]	Optical attenuators	RCA C31000E/F	0.75 ±0.22
		EMI 9558	0.80 ±0.22
		Amperex 56TVP	0.71 ±0.3
Young and Schild [88]	Optical attenuators	EMI 9558	0.75 ±0.10
Birenbaum and Scarl [89]	Optical attenuators	RCA C31000F	0.61 ±0.10

Table 5.3: Other reported values of photoelectron collection efficiency.

The difficulty of measuring very high pulse count rates and very low photocathode currents both increase the opportunities for error, see the comments of Young and Schild [88].

A summary of some of the early results is given in Table 5.3. The values of η in the table refer to the authors estimates of the counting efficiency of single photoelectrons. In most cases only the counts above a discriminator level are recorded, and most authors do not discuss in detail the effects of their discriminator thresholds. In several cases there is some doubt as to whether the authors have corrected for the fraction of pulses below the discriminator level, despite referring to their results as 'collection efficiencies'. However Young and Schild are careful to present their results as a function of the discriminator level used and the value they report is an extrapolation to a zero discriminator level which they refer to as the photoelectron collection efficiency.

The two reported results for the RCA C31000F photomultiplier are consistent within the reported errors, but Birenbaum and Scarl [89] have used a rather high discriminator level which is 45% of the peak in the pulse charge spectrum. An examination of their data suggests that this effect would reduce their deduced value by an amount consistent with the ratio of their results to those of Lakes and Poultney [87]. The latter paper reports photoelectron collection efficiencies of about 75% not only for the RCA C31000F photomultiplier but also for the EMI 9558 and Amperex 56TVP photomultipliers.

Chapter 6

Photomultiplier properties

This chapter presents a summary of various photomultiplier properties which have an impact on the design of, and results from, the SNO detector. The sensitivity of photomultiplier efficiency, deduced in the previous chapter, to residual magnetic fields along the axis of the photomultiplier was measured. This measurement is important for several reasons. Firstly the sensitivity of the measured efficiency to residual axial magnetic fields should be shown to be small enough to give confidence that the values presented in the previous chapter are reliable. Also the magnetic field cancellation in the SNO detector should be shown to be adequate to ensure that the efficiency of the photomultipliers in the detector are not significantly reduced and that the field does not introduce a dependence of their efficiency to their position within the detector.

The reconstruction of an event vertex from the Čerenkov radiation requires that the spread of the transit time of each photomultiplier is as small as possible. Although there are several effects which degrade the resolution of an event vertex, the intrinsic transit time spread (TTS) of the photomultipliers is a major influence on the net resolution. The TTS was measured as a function of the first dynode voltage for a SNO photomultiplier, and its impact on the event vertex reconstruction is discussed. The vertex resolution is minimized by a compromise between low photomultiplier noise and small TTS.

The problems caused by afterpulsing are not believed to be critical to the SNO detector, but a brief description of the phenomenon, with some experimental data[1], is given in the first section of this chapter. These data are discussed, and are found to be consistent with the conventional view of the origin of afterpulsing. The work presented here is intended to illustrate the problem of afterpulsing; for a more detailed description see Morton *et al.* [94], Paske [95] or Williams *et al.* [96]. A brief description can be found in the RCA Photomultiplier Handbook [97].

[1]These measurements were made when the author was given an opportunity to use a Fourier Transform Spectrometer at the Thorn EMI research laboratory at Ruislip, Middlesex, England.

6.1 Afterpulsing

The temporal nature of the signals from a photomultiplier is not truly random; one observes an enhanced probability of counting a signal immediately after its predecessor. This phenomenon is known as afterpulsing, and is an undesirable feature of photomultiplier behaviour. Several mechanisms for generating afterpulses exist; principally gas ionization and optical feedback. The latter is not usually a major problem in modern photomultiplier designs. However the former can be a problem when using a photomultiplier in pulse counting mode to monitor processes with durations of order 1 μs; for example the decay of the muon.

In order to investigate time-correlated effects a Malvern Digital Autocorrelator was used to measure both the time correlation of input signals and the probability density of the number of signals in a time interval. The time correlation measurement system is free from deadtime[2] and the results are equivalent to a Fourier transform of the power spectrum of the incident signal pulse train. The time interval is set by the user and is subdivided into 64 equally spaced bins (6 bit resolution). Hence the first bin contains all the afterpulses within the first 1/64 of the total time interval and so on. The total interval time should be chosen to be larger than, but not much larger than, the coherence time of the signal pulses. Unfortunately there was no opportunity to attempt a time calibration of the autocorrelator, but the absolute time scale is thought to be reliable.

For a 200 mm photomultiplier the pulse correlation, or afterpulsing, has two distinct time scales. Firstly the optical feedback time, which is typically the transit time of the photomultiplier, here about 60 ns. The mechanism for this feedback is that light is generated by the dynode multipliers which is subsequently detected by the photocathode of the photomultiplier. Modern photomultipliers are designed to minimize this cause of afterpulsing, and it is not a problem for the photomultipliers considered in this work. This prompt afterpulsing was not studied in this work.

The second coherence time is that resulting from the passage of ionized gas molecules from the dynode stack to the cathode. In this case the feedback mechanism is that the current pulse along the dynode ionizes some free molecule or atom (possibly from the residual gas) inside the photomultiplier and subsequently this ion is accelerated towards the photocathode. On impact with the photocathode the ion causes secondary ionization and in doing so liberates electrons from the cathode itself. Depending on the mass of the ion and its charge, the time scale for this process is typically in the range 0.5 μs to 10 μs for 200 mm photomultipliers.

[2]The operation manual for the autocorrelator states that 'The time correlation measurements are done by integrating the signals arriving between two sample time clock pulses. Thus every pulse is counted with no dead time between samples, therefore no information is lost. This technique offers the additional advantage of integrating out noise components which have a time dependence fast compared with the sampling time. This removes aliassing problems which could be severe in other correlators when analysing low frequency effects.'.

Run No.	Source	Count rate	Sample time	Comments
1 and 2	Lamp	130 kHz	1 μs	Good statistics.
3 to 7	Lamp	130 kHz	50 ns	Poor statistics hence 5 runs.
8	None	1 kHz	1 μs	Dark counts only.

Table 6.1: Time correlation measurements.

The ionic afterpulse mechanism is the most significant source of afterpulsing, as it contributes the largest fraction to the total integrated afterpulse probability. This consideration leads to typical window times in the range 3 μs to 60 μs in this study.

The EMI 9351 photomultiplier (serial number 1019) described in the previous chapter was used. The photomultiplier was illuminated using a lamp giving single photoelectron count rates up to several MHz and was operated at 750 volts between cathode and first dynode with 1500 volts in total. The overall gain is quite important in afterpulse work as the probability of an afterpulse increases with the gain of the photomultiplier. This may be because larger electron pulses along the dynodes give enhanced probability of ionizing a gas molecule, and producing an afterpulse. This effect is well known and is not subject to any investigation here. The gain was kept constant at 10^7. The discriminator threshold was kept constant; equivalent to 1/4 of a single photoelectron charge.

Several runs were performed to investigate the effects of light intensity, sample time, radioactivity and statistical variations on the afterpulse distribution. These are summarized in Table 6.1. The data from Runs 3 to 7 were statistically poor, and so an average was taken. This is plotted in the upper graph of Figure 6.1, along with the average data from Runs 1 and 2. The afterpulse probability is plotted on the ordinate axis and is expressed as the percentage probability (per unit time) of an afterpulse occurring as a function of a time delay following the initial pulse. Figure 6.1 clearly shows three peaks at times of 0.5 μs, 2 μs, and 6 μs following a pulse.

It is possible that these peaks could be due to different residual gases in the photomultiplier bulb or due to the creation of the ions at different places. It is most likely that the ions were singly charged. A phenomenological model in which a gas molecule is ionized near the dynode stack and is accelerated towards the photocathode, gives an afterpulse time t of order

$$t \sim \eta l \left(\frac{m}{qV}\right)^{1/2} . \tag{6.1}$$

Here l is the path length between the point of ionization to cathode, m is the mass of the ion, q its charge and V is the electric potential difference between the creation point and the

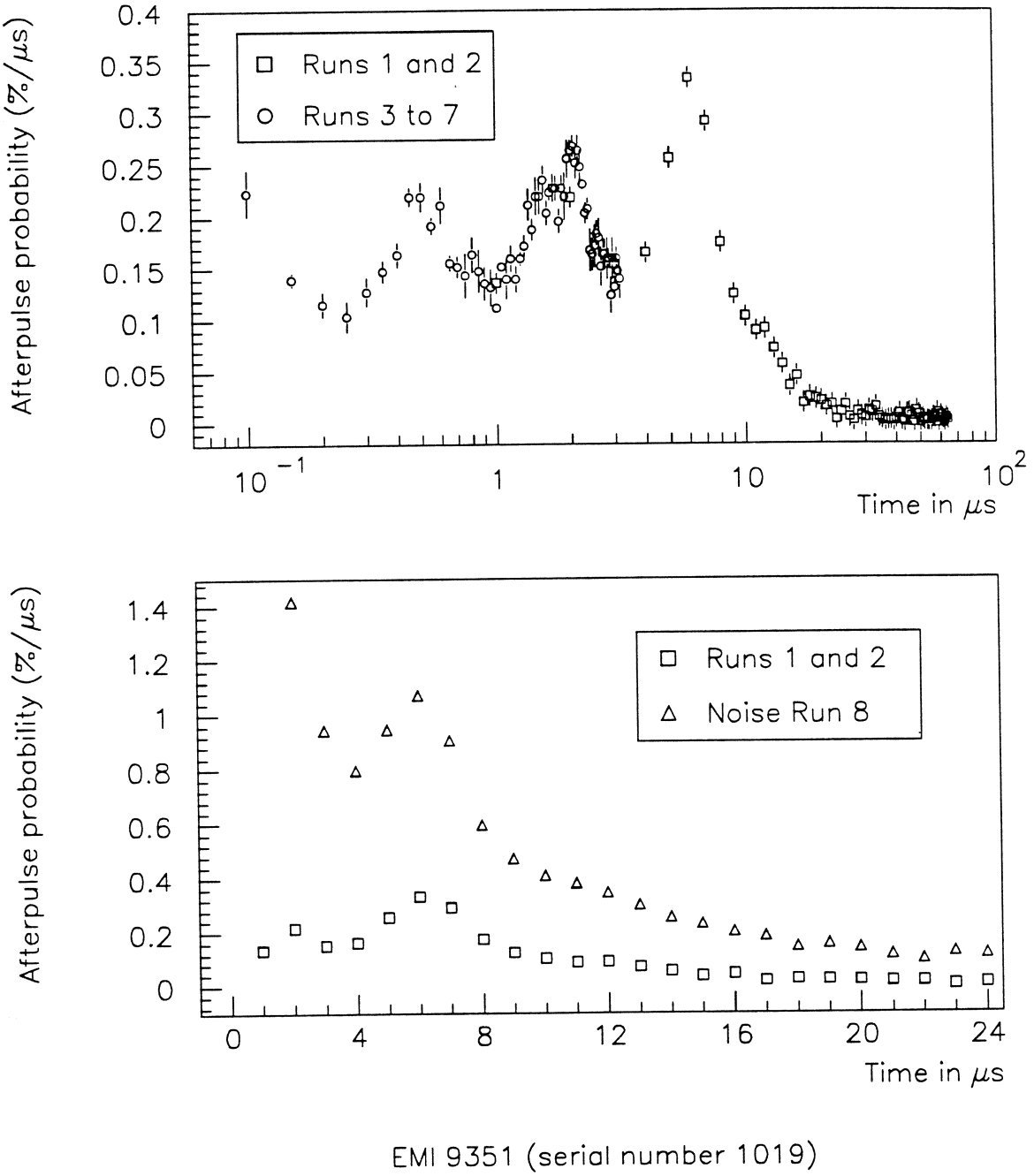

Figure 6.1: The Fourier Transform of the pulse train from an EMI 9351 photomultiplier. The upper plot clearly shows the afterpulse peaks at 0.5 μs, 2 μs and 6 μs. The lower plot compares this data with that from a dark noise spectrum Run 8.

cathode. η is a dimensionless parameter whose value depends on the geometry and the field shape inside the photomultiplier. Two suggested mechanisms for creating such an ion are: ionization of a gas molecule by electron scattering, and liberation of an ion from a dynode surface by electron impact, particularly at the anode and first dynode. Qualitatively, both these mechanisms will give afterpulse probabilities increasing with gain, and both are consistent with the above model.

For a singly charged ion of atomic mass M, this model predicts that the time in microseconds is of order $\simeq 0.5\sqrt{M}$. Thus the model gives the correct time scales for afterpulsing. By conjecture the peaks could be due to light, intermediate and heavy ions respectively, but in the absence of any other distinguishing features, the molecular origin of each peak is probably a matter for speculation only. The absence of any calibration of the afterpulse time scale for any molecule prevents any more quantitative analysis. This technique could be calibrated by allowing contaminant gas into a bulb, and investigating the induced peak. Morton *et al.* [94] summarize the work of J. S. Allen, then of the Los Alamos National Laboratory, New Mexico who succeeded in introducing such test gases into photomultipliers without destroying the photocathode. Allen was then able to demonstrate that the afterpulse time varied with the ionic transit time between the dynodes and the cathode.

The lower graph of Figure 6.1 shows the data from Run 8 in which no illumination was provided and only the noise of the photomultiplier was counted. This is compared to the data from Runs 1 and 2. It is apparent that the afterpulse probability of dark counts is significantly larger than those of optical origin. The explanation of this result could be that some dark counts are caused by radioactivity and cosmic radiation, which can cause large pulses associated with many photoelectrons. These large pulses would then have a high afterpulse probability as they produce large current pulses along the dynode multiplier stack. These events, although relatively infrequent, cause many afterpulses and could account for a significant fraction of the noise by this mechanism. Another way of illustrating this behaviour is to measure the number distribution of number of pulses arriving within a time window.

The probability density function is defined as the probability $P(r)$ of counting r pulses within a preset time window. It is measured by averaging the counts from many such time windows to achieve statistical accuracy. These data are then normalised by dividing by the total number of counts to ensure that the integrated probability is unity. For this measurement the time window is chosen to be less than the typical noise interval time, here 1 ms, but greater than any afterpulse time. The chosen time was 100 μs.

If the hypothesis that glass radioactivity causes some of the time correlated noise signal is correct, then the addition of a radioactive source to the photomultiplier should cause a significant distortion of the probability density function. If the interval between decays from

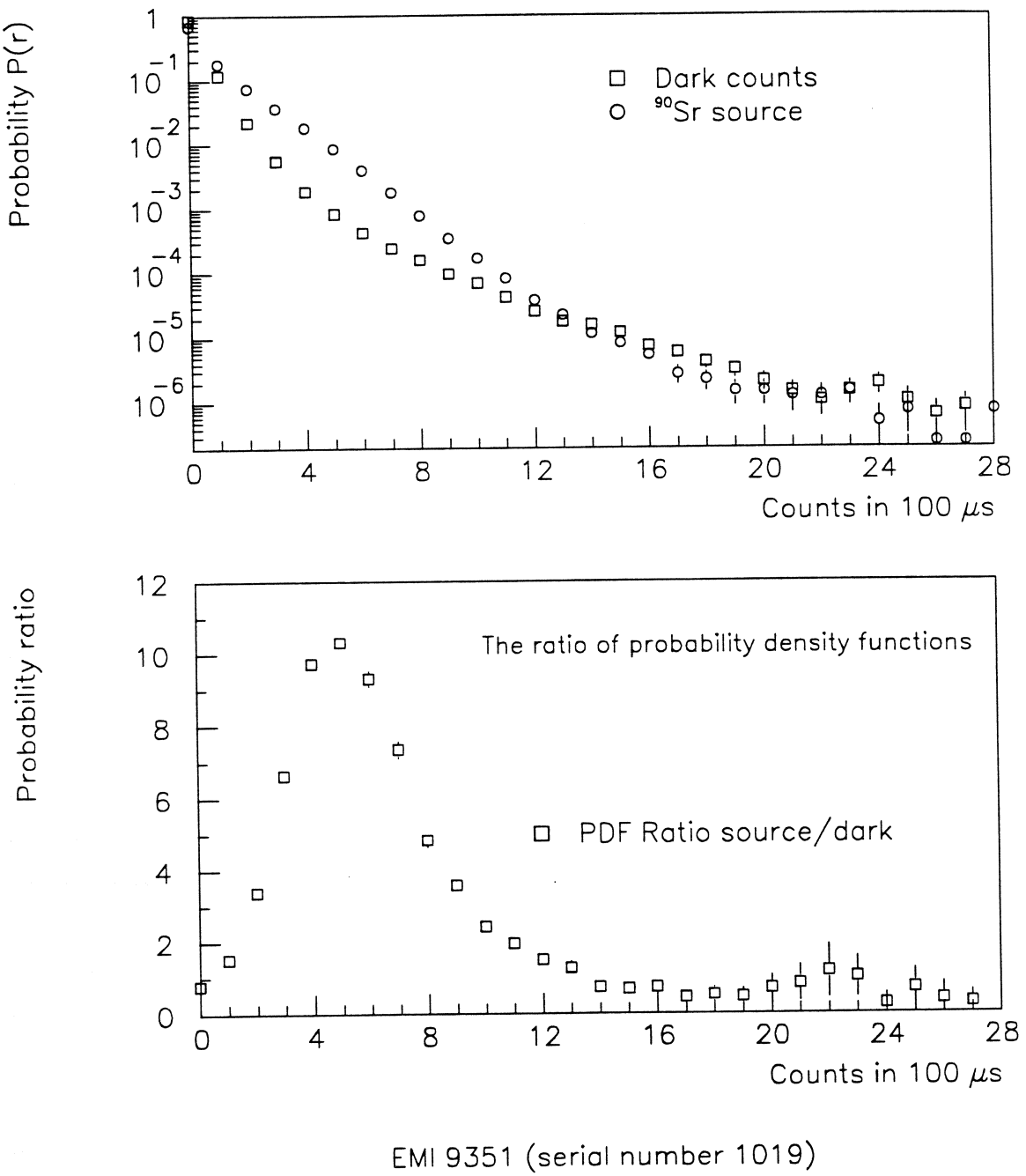

Figure 6.2: The upper plot shows the probability of obtaining r counts in a 100 μs window with and without a ^{90}Sr source. The lower plot shows the ratio of these data and the enhancement for about 5 counts in 100 μs.

such a source were small compared to the time window, then any change of the probability of observing large numbers of counts in 100 μs must be due to an enhanced afterpulse probability from large signal. This effect was investigated by the use of a ^{90}Sr source placed on the photocathode of the photomultiplier. The source used had a very thin window between it and the photocathode, but had an aluminium back plate so that it will also emit backscattered electrons. This ensures that Čerenkov radiation will be generated in the glass (window) near the photocathode and large pulses are thereby generated. It should be stressed that a single decay can produce many photoelectrons, but these will be counted as a single large pulse, as Čerenkov photons from a single decay will be coincident on the time scale of a signal pulse width.

With a weak source mounted on the photocathode, the count rate of the photomultiplier was seen to increase by about 1 kHz. This means that the expected number of counts in a 100 μs window is small, about 0.1. If we compare the probability density function with and without the ^{90}Sr source, we expect an enhancement of the probability of a single count in the time window due to the higher count rate. However the probability of (say) 5 beta decays counted in a 100 μs interval is very small $\sim 10^{-7}$, and this random chance would be overwhelmed by the contribution from the noise. So if an enhancement were seen its origin would therefore be attributed to multiple afterpulsing caused by the large pulse.

Figure 6.2 shows the probability density function expressed as the probability $P(r)$ of counting r signals in a 100 μs window. The data show a clear enhancement of the probability of obtaining about 5 counts in the time 100 μs. If this were simply due to a higher count rate, the enhancement factor, plotted in the lower graph of Figure 6.2, would increase monotonically with the number of counts in the time interval. Hence this effect is due to the presence of the radioactive source, and the nature of the large pulse heights that its decays induce.

If this peak is caused by afterpulsing from large pulses, we can conclude that an average beta decay electron produces about 5 afterpulses in this situation. This can be related to the observation that the time correlated noise is associated with processes which occur about 10 times per second. Using these crude data we would predict about 50 Hz of the dark noise rate in such a 200 mm photomultiplier is due to internal radioactivity. This is consistent with the observation that the afterpulse filter described in the previous chapter removes about 20% of the noise counts in a dark adapted photomultiplier. It seems likely that the other sources of noise such as the long lived components of the glass scintillation and thermionic emission will behave in a similar way to optical pulses, and have the low afterpulse probabilities associated with single photoelectron pulses.

6.2 Magnetic field sensitivity

The magnetic term $q(\mathbf{v} \wedge \mathbf{B})$ of the Lorentz force on a particle of charge q with velocity $\mathbf{v}$ in a magnetic field $\mathbf{B}$ implies that the electron optics inside a photomultiplier are sensitive to local magnetic fields. The electron optics in a photomultiplier are optimized for use in a field free region, and so any field will alter (and usually destroy) this optimization. Generally all aspects of the performance of a photomultiplier are degraded with increasing magnetic field. In particular the SNO detector requires that the efficiency and TTS are optimized to improve energy resolution and to improve the vertex reconstruction accuracy respectively.

The smallest field that can be tolerated is an important criterion not only for the photomultipliers in the SNO detector, but also for the efficiency determination in Chapter 5. It was demonstrated in the previous chapter that by adjusting the position of the Mortar and a suitable choice of field coil current magnetic fields could be reduced to about 0.3 μT. Any deviation from the coil current of 420 mA would lead to a magnetic field along the axis of the photomultiplier. Therefore a simple test was conducted to determine the effect of different field coil currents on the absolute efficiency of the photomultiplier.

The Hamamatsu R1408 photomultiplier (serial number CB0274) used in Chapter 5 was used in this study under the same conditions as in the SNO detector. The current in the coils was varied between -1200 mA and $+2000$ mA. At each coil current four count rate measurements were taken with the source ON, OFF, OFF, ON respectively, to reduce systematic noise effects as described previously. The discriminator level was set at about 1/5 of a single photoelectron charge. The results are then expressed in terms of the photoelectron counting efficiency of the photomultiplier in percent. These results are plotted in Figure 6.3; note the suppressed zero on the ordinate.

Two features of this graph require comment. Firstly the data are consistent with the photoelectron counting efficiency of about 55.5% (with a discriminator level of about 1/5 of a single photoelectron charge and field coil current of 420 mA) which was reported in Figure 5.6. The change in the efficiency values is very small for changes in current of order 100 mA, so that the efficiency values reported previously are the optimal ones. Secondly the photomultiplier is surprisingly insensitive to typical terrestrial magnetic fields of order 50 μT. This is principally due to the high voltage from cathode to first dynode, but is also due to the fact that the residual magnetic field was applied parallel to the axis of the photomultiplier. Most photoelectrons between the cathode and first dynode have a velocity vector which has a relatively small angle θ to the axis of the photomultiplier along much of the trajectory. Hence magnetic fields parallel to this axis will lead to a small Lorentz force $qvB\sin\theta$ in the plane normal to the axis of the photomultiplier. Thus the effect of a field parallel to the photomultiplier axis is small.

The experimental observation reported here is in agreement with the computer simulations

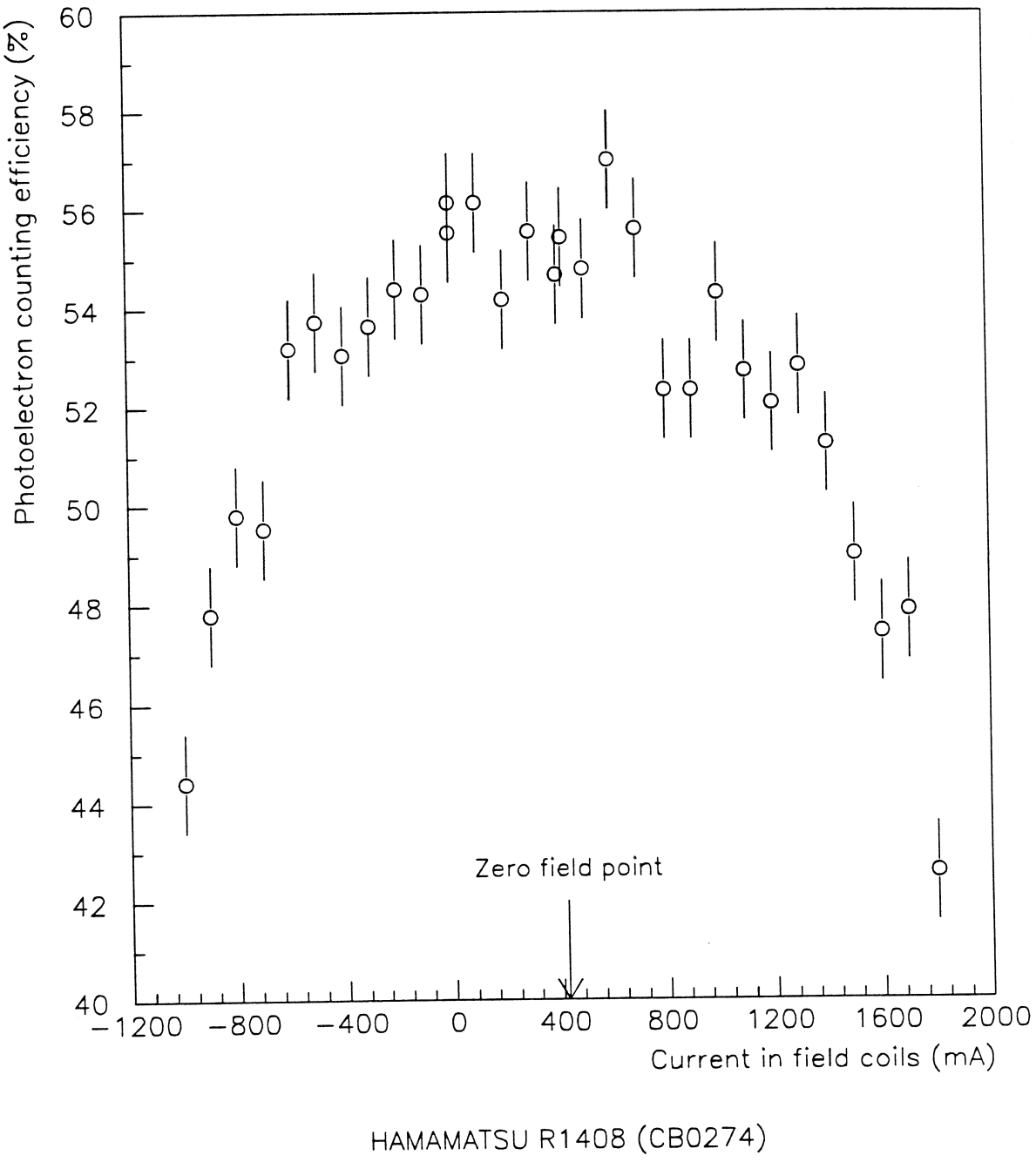

Figure 6.3: The single photoelectron counting efficiency of a Hamamatsu R1408 SNO photomultiplier as a function of the current in the field coils of the Mortar. The magnetic fields are parallel to the axis of the photomultiplier.

Field strength	**B** $\perp$ to D1 vein	**B** $\parallel$ to D1 vein
0 μT	1.00 ± 0.02	1.00 ± 0.02
16 μT	0.97 ± 0.02	0.97 ± 0.02
32 μT	0.91 ± 0.02	0.95 ± 0.02
48 μT	0.81 ± 0.02	0.87 ± 0.02

Table 6.2: Relative counting efficiency of Hamamatsu R1408 number ZW262.

reported in the SNO report [98], which show that magnetic fields of less than 40 μT have 'no effect on the photoelectron detection efficiency'. This report also describes experimental work to determine the sensitivity of counting efficiency and TTS to magnetic fields perpendicular to the photomultiplier axis. A summary of the data presented in the report [98] is shown in Table 6.2. The data shows that although the photomultipliers are more sensitive to fields perpendicular to the photomultiplier axis, only a modest reduction of the terrestrial field is necessary to ensure optimal efficiency.

The SNO report [99] describes measurements of the local magnetic field at the Sudbury site which find about 55 μT in the vertical direction and about 15 μT along the horizontal direction. After a series of computer calculations it was decided that only cancellation of the vertical component of the local field was necessary. With a series of horizontal coils around the detector with suitable currents, it was calculated that the maximum residual field is about 16 μT, and the consequential reduction in photomultiplier efficiency should be very small.

6.3 Transit time spread

The reconstruction of event vertices from neutrino interactions in the SNO detector is reliant on the TTS of the photomultipliers being small compared to the light transit time across the detector. For the elastic scattering and charged-current interactions which produce a relativistic electron in the final state the fraction of photons emitted into the backward hemisphere (with respect to the initial direction of the electron) is small, see [70]. The reconstructed distance along this axis of the initial direction is covariant with the TTS and direction of these few photons, and so the effective number of photomultipliers from which sensitive information can be extracted can be quite small. For a summary of the Monte Carlo studies performed to investigate the effects of TTS and scattered light, see SNO report [100], and the references therein.

The TTS of the photomultipliers used will be measured *in situ* in the SNO detector using

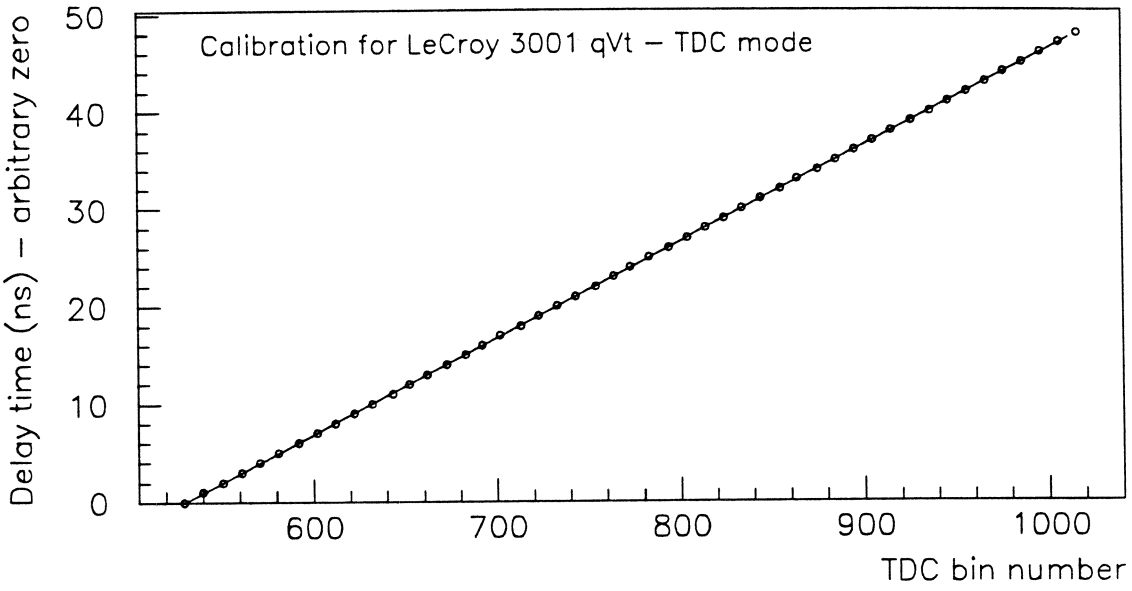

Figure 6.4: Calibration data for the LeCroy 3001 qVt in TDC mode.

optical calibration sources. These are discussed in Chapter 8. In the work presented here the TTS of the Hamamatsu R1408 photomultiplier CB0274 was measured using the standard SNO photomultiplier base operating at standard operating voltages described in Chapter 5. In addition the TTS was measured for some lower voltages between cathode and first dynode, and also in the presence of small axial magnetic fields.

The experiment to measure the TTS was performed in the Mortar with the Mark 3 source mounted on the front window of the 50 mm monitor photomultiplier. The pulse counting electronics was similar to that shown in Figure 5.4, but with the addition of another channel for the monitor photomultiplier. Ortec 583 constant fraction discriminators were used on both channels and the walk potential was set to ground in both cases. The external shaping delay to minimise discriminator walk is about $1.1t_r - 0.7$ ns where the 0.7 ns comes from the internal delay and t_r is the risetime of the anode pulses. Empirically it was found that an external cable delay of 1 ns and 3 ns minimised the walk for signals from the monitor (R1828-01) photomultiplier and the R1408 photomultiplier respectively.

The signals from the monitor photomultiplier were delayed after the discriminator so that the signals from the large 200 mm photomultiplier were used to start a Time-to-Digital Converter (TDC). This configuration was preferred to reduce the deadtime of the TDC. A LeCroy 3001 qVt multichannel analyzer was used in 't' mode to act as a TDC, with 10 bit resolution giving 1024 channels. Each channel has a $2^{16} = 65536$ count capacity and the time interval is nominally 0.1 ns per channel.

Unlike the charge measurements performed with the qVt used in Chapter 5, the calibration of the qVt in time mode is important for the TTS measurements. A simple calibration of the

TDC was performed by injecting identical signals into both discriminators with an adjustable delay between the channels. The delay was provided by NIM rack-mounted delay units, which provide delays of various lengths in steps of 1 ns. The delay length was altered so that the TDC was calibrated in the range of channels (500-1000) that was used in the TTS experiments. The TDC channel which counted, for various delays, was noted and the results are plotted in Figure 6.4. The best-fit line through these data has a gradient of 0.0988 ± 0.0002 ns/channel, where the quoted error refers to statistical uncertainties only.

This attempt to calibrate the TDC could be refuted on the grounds that the delay lines may not be exactly spaced by 1 ns, and also that introducing delay may change the shape of the NIM signal and could therefore change the walk of the discriminator inside the TDC. Both factors could give rise to small deviations, and with this in mind the calibration shows that the TDC is linear and accurately calibrated at the level of one percent.

A larger correction is that to be made for the TTS of the monitor (R1828-01) photomultiplier, which has a time resolution of about 0.25 ns (1 standard deviation) at the voltage used[3]. As the photomultiplier is used within 100 mm of the centre of the source, it is likely that several photoelectrons per beta decay will be produced in the cathode of the monitor photomultiplier. This may affect the transit time spread from this photomultiplier, and so a small uncertainty is introduced when the correction for the small photomultiplier TTS is made. This small correction is made by simply subtracting in quadrature the 0.25 ns TTS from the monitor photomultiplier from the experimentally observed TTS.

It was found that the transit time spectrum could not be well characterized by a simple Gaussian fit to the data. A satisfactory fit was obtained with a skewed kurtosoidal Gaussian of the form

$$p(t) = B + A \exp\left[-\frac{1}{2}\left|\frac{t-\tau}{\sigma - s(t-\tau)}\right|^{\gamma}\right], \tag{6.2}$$

where the parameters A and B represent the peak height and background. The centroid parameter τ depends only on the delay between the signals from the two photomultipliers. The degree of 'skewness' and kurtosis[4] are described by the parameters s and γ respectively. A fit of this form produces a satisfactory fit, although the assumption of a constant background increases the χ^2 of the fit to about 10 per degree of freedom.

The detailed shape of the background was not well known (see following discussion) and provided an obstacle to an improved fit. However it seems likely that the background is different (almost certainly greater) for a late signal from the 200 mm photomultiplier compared

[3]The transit time spread of the Hamamatsu R1828 photomultiplier has been measured by the manufacturer, and the value quoted here is deduced from their data. It applies for single photoelectrons only.

[4]Kurtosis is a measure of the degree of sharpness of the peak.

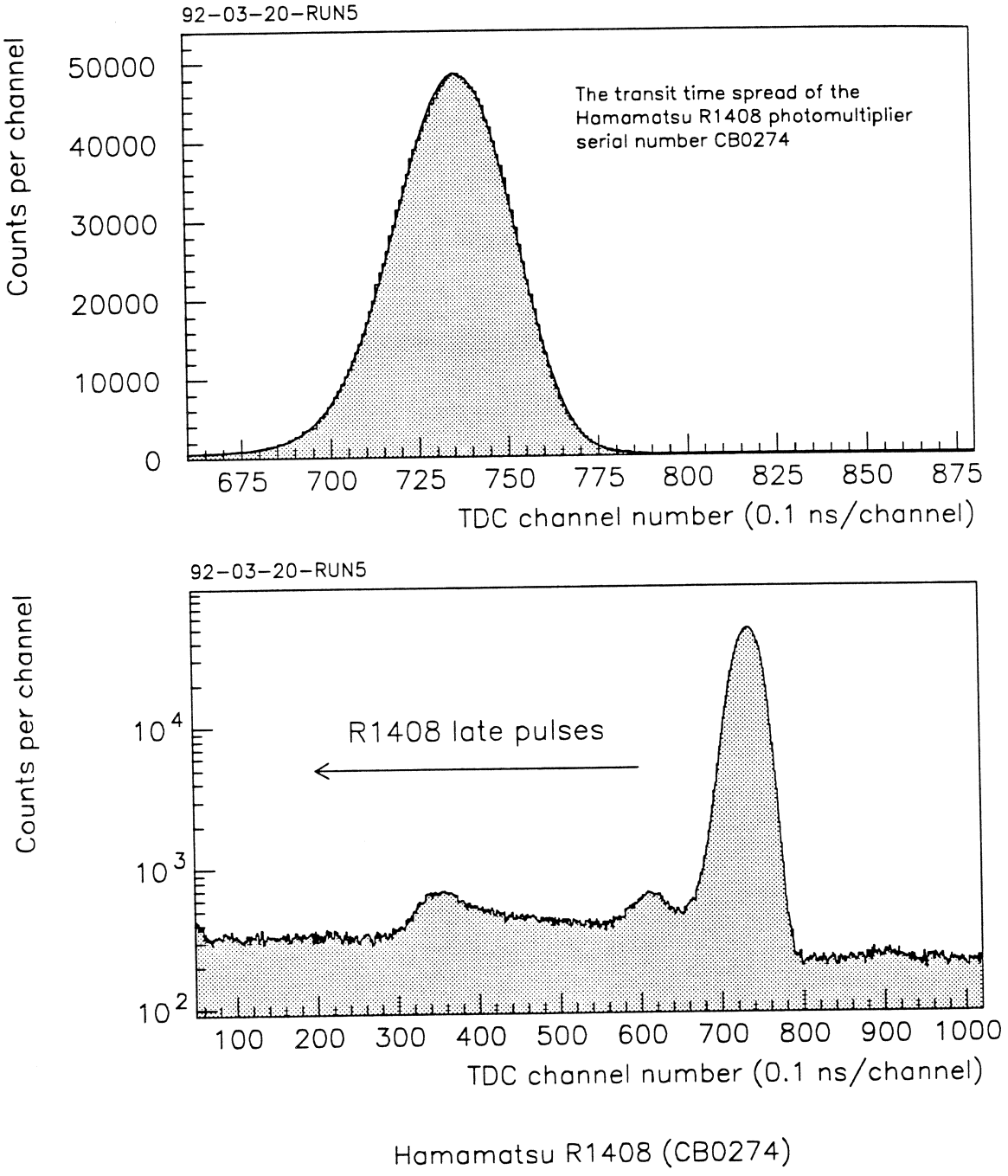

Figure 6.5: The upper plot shows the TTS peak and fitted curve over the fit interval for a Hamamatsu R1408 photomultiplier used under SNO conditions. The lower plot shows the entire TDC spectrum including the 'late' background peaks; note the logarithmic scale.

Description	Voltage		Fit parameters				TTS
of Run	K-D1	K-A	χ^2/DOF	σ	s	γ	(ns)
Standard SNO base	1031	2075	4.01	16.6	0.053	2.10	1.64
No field cancellation	1031	2075	4.96	17.0	0.049	2.17	1.68
Zener diode base	750	1835	4.02	18.3	0.059	2.18	1.81
Zener diode base	600	1700	4.52	19.5	0.071	2.17	1.93

Table 6.3: TTS measurements on Hamamatsu R1408 photomultiplier CB0274.

to early ones. For this reason a modified background fit of the type

$$B(t) = \begin{cases} \alpha & \text{if pulse is early } (t > \tau) \\ \alpha + \beta & \text{if pulse is late } (t < \tau) \end{cases} \tag{6.3}$$

was tried with constant parameters α and β, note that late pulses have $t < \tau$, as the 200 mm photomultiplier starts the TDC. The parameter α is then interpreted as the random coincidence background, and β is a parameter describing the additional 'background' following a pulse. Despite the covariance introduced between the background and the centroid, the fits thereby obtained were more satisfactory and the χ^2 was reduced to about 4 per degree of freedom. This procedure altered the value of sigma by only about 0.5%. In the absence of more information about the background and the parent distribution from which the data are sampled, it is difficult to improve the χ^2 of the fit much further.

The fit parameters are shown in Table 6.3 for four data sets. For illustration the first TDC spectrum obtained from the Hamamatsu R1408 photomultiplier (CB0274) discussed previously is shown in Figure 6.5. The peaks at channels 610 and 350 occur 12.5 ns and 38.5 ns late respectively. These are attributed to light emitted from the monitor photomultiplier when an electron pulse hits the first dynode and the anode respectively within the 50 mm photomultiplier. The peaks are not consistent with afterpulsing within the R1408 photomultiplier. The fits for the main peak were performed using the CERN Program Library routine MINUIT [101] which finds parameters to minimize the χ^2 of the fit. In each run the fit was made over 220 channels of the TDC data, as shown in Figure 6.5. The errors associated with the fit parameters are estimated by the routine, but these are statistical parameters deduced from the sensitivity of the fit quality to changes in their values. These errors do not reflect the effects of uncertainties in the background and the lack of knowledge of the parent distribution. These were estimated (see below) by trial of various forms for the background, and different

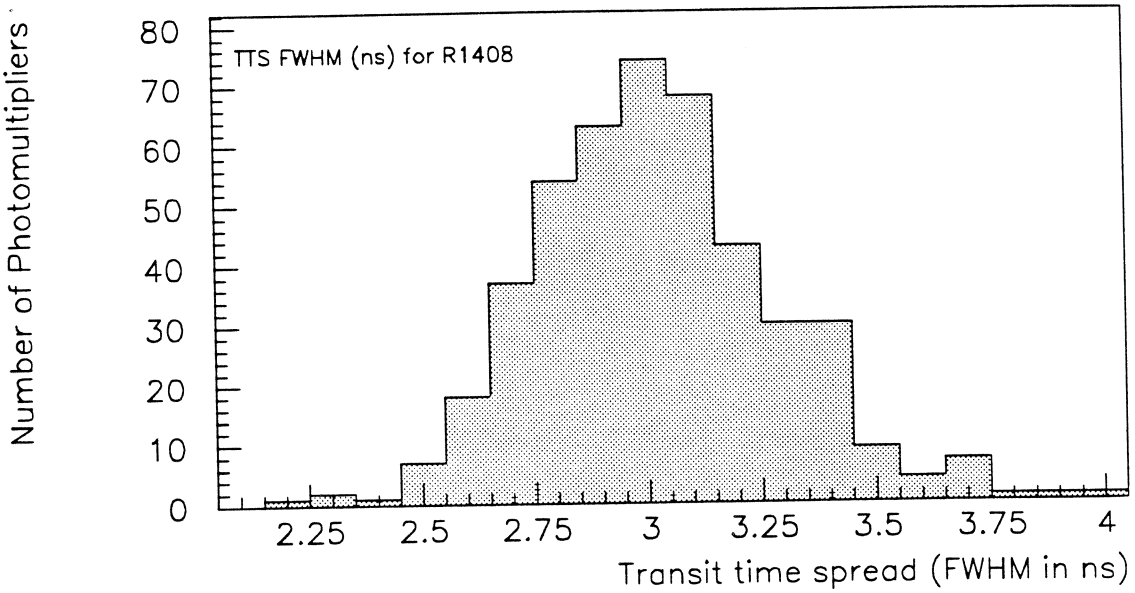

Figure 6.6: The distribution of the TTS of SNO photomultipliers.

data set under identical experimental conditions. Naturally there are additional systematic errors due to the TDC calibration etc.

The last column in Table 6.3 shows the deduced TTS of the 200 mm photomultiplier after correction for the TTS of the monitor photomultiplier, made by quadratic subtraction of 0.25 ns. The runs at reduced voltages between cathode and first dynode show an increased TTS, as does the run with an axial magnetic field present. The random and statistical errors for these values of TTS are both about 0.02 ns. This value can be compared to measurements made on the first batch of photomultipliers supplied to the SNO collaboration[5]. The TTS distribution of a sample of 458 photomultipliers is shown in Figure 6.6; note that the full width at half maximum (FWHM) of the transit time spread is quoted. For the near Gaussian shape of the transit time distribution a conversion factor of about 2.4 applies between the σ parameter and the full width at half maximum. The increase of the TTS with decreasing the voltage between cathode and first dynode can be further demonstrated by plotting this distribution as a function of total applied voltage to achieve a gain of 10^7. These data are shown in Figure 6.7, and indicate that most photomultipliers with low TTS require high total voltages and visa versa.

[5]These data were kindly supplied in a private communication from R. G. H. Robertson, Los Alamos National Laboratory, New Mexico.

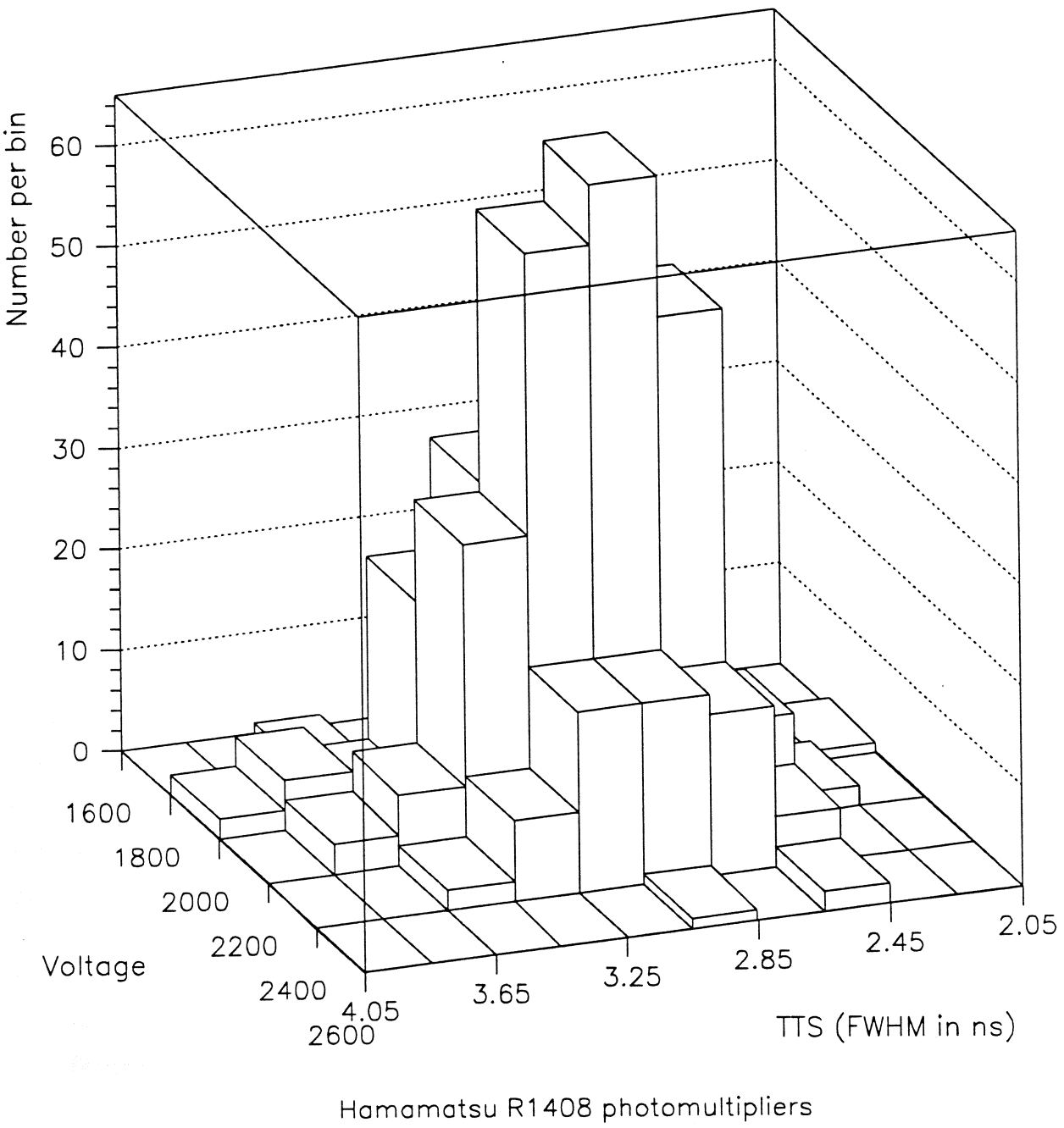

Figure 6.7: The distribution of number of Hamamatsu R1408 photomultipliers as a function of TTS (right hand axis in ns) and total applied voltage (left hand axis in volts).

Chapter 7

The photocathode area of the Hamamatsu R1408 photomultiplier

The principal aim of the work[1] described in this chapter is to determine the relative photon counting efficiency, as a function of position on the photocathode, of the SNO photomultipliers. The manufacture of the reflectors for the photomultipliers requires knowledge of the relative sensitivity of the photocathode (including photoelectron collection efficiency) as a function of the position of impact of an incident photon, particularly in the region near the boundary of the photocathode. This is required so that the diameter of the smaller aperture of the reflector can be determined and should be made as large as possible in order to maximize the Čerenkov radiation collection from neutrino interactions. However, if the reflector covers an area larger than that of the photocathode, the optics of the reflector are compromised, and the efficiency of recording photons which originated at the centre of the detector is reduced. For this reason the cylindrical polar radius of the boundary of the photocathode must be known.

The Hamamatsu R1408 photomultipliers used here are those made using the Schott 8246 low background glass, and are identical with those to be installed in the SNO detector. The photocathode diameter is nominally 200 mm. The photomultipliers were measured using identical bases and operating conditions as those to be used in the detector, except that the tests were performed in air rather than water. The absence of water will not alter the deduced photocathode area. The 5 photomultipliers used in this study were taken at random from a sample of 20 (SNO) Hamamatsu R1408 photomultipliers, and the Queens University spot scan apparatus was used to measure the relative efficiency as a function of position on the photocathode. In addition to the scan data, systematic checks were made to measure the positional accuracy and resolution of the apparatus. These parameters were found to be consistent with the expected values.

For brevity, only a summary of the photocathode spot scan apparatus is given below. A

[1]This chapter describes the main work of the author at Queens University, Ontario, Canada from 24^{th} September 1991 to 5^{th} October 1991.

source of Čerenkov radiation (^{90}Sr in acrylic) was used to provide illumination, which was collimated to a beam with a divergence of about 15° (full width half maximum). The exit aperture of the source had a length of about 10 mm and a slit width of about 2 mm, and the source was always used to scan the photomultiplier in a direction normal to the long axis of the slit. Hence the 2 mm width represents the smallest resolution possible with this apparatus. This source is rotated on a circle of radius 126 mm, and its position is monitored with an external pointer to indicate the angle of the source with respect to the axis of the photomultiplier. The direction of the scan with respect to the vein (direction of the wires of the mesh) of the first dynode was chosen at random for the photomultipliers tested in this study[2].

Using the Hamamatsu R1408 photomultiplier, this geometry ensures that the source traverses the surface of the photomultiplier front window for angles smaller than the transition angle θ_t (about 40°). For angles larger than this the source moves off the surface of the photomultiplier by a short distance, thus degrading the resolution. The R1408 photomultiplier under test was aligned between four posts, which centre the photomultiplier about the 0° position of the source. The photomultiplier is mounted so that the source just touches the photomultiplier in the 0° position. This alignment is accurate at the level 1 mm as confirmed by the deduced position of a test mask, see below. Also the observation of symmetry of response about the 0° position gives additional confidence that the alignment was accurate.

The Čerenkov source is monitored by a smaller Hamamatsu photomultiplier, type R1635, serial number WA1781, to provide a coincidence condition for the detection of Čerenkov photons. The coincidence rate was typically 40 Hz. The housing for the apparatus is a large copper box which a acts as an electromagnetic shield to attenuate radio-frequency interference. This box is surrounded by two magnetic field coils oriented to cancel the local magnetic field. The operation of these coils was verified using a flux probe in the position of the test photomultiplier. The residual magnetic field in the region of the photomultiplier was always less than 1 μT. This condition required a current of 304 mA in the coils, and this current was monitored throughout the experiment.

The photomultipliers were used with the standard SNO photomultiplier base which was described in Chapter 5. M.H.V. cables were used, with intrinsic impedance 75 Ω. A simple R-C filter was used as a signal 'pick-off' to separate the high voltage D.C. supply from the photomultiplier signals. These signals (from test and monitor photomultipliers) are then used to trigger Constant Fraction Discriminators and then Coincidence, ADC and TDC camac modules. The ADC was found to have a 'off-set' or pedestal charge and this was found by the procedure described in 5, resulting in a pedestal of +16 channels. Both the TDC and

[2]This approach was used as the data were to be applied to the reflector design which requires some 'average' over azimuthal angles.

ADC channel sensitivity and linearity had been calibrated previously, and were found to be 0.23 ps/channel and 0.25 pC/channel respectively, with negligible non-linearity.

A scaler was used to count both coincidence rates and the 'singles' rates from the photomultipliers. The coincidence resolving time $\tau = \tau_1 + \tau_2$ was chosen to be 100 ns, so that no signals were lost to photomultiplier transit time spread (TTS), and also that reflections from large signals do not re-trigger the coincidence unit. The discriminator level for the test photomultiplier was set to about 1/4 of a single photoelectron signal, which was estimated from the peak of the pulse height distribution (i.e. the modal charge deposited). This discriminator level was monitored throughout the experiment using the ADC and by measuring the level-test voltage from the discriminator itself. The discriminator for the monitor photomultiplier was kept at a very small fraction (about 1/10) of the charge deposited by a single photoelectron, which was monitored in a similar manner. With such monitoring it was possible to make a comparison between the efficiency of different photomultipliers, as well as different points on a single photocathode.

After a photomultiplier was installed in the apparatus and the latter made light-tight, the photomultiplier was allowed to operate at full voltage in order to reduce the noise count. This ageing is usually substantially complete after several hours. After ageing overnight, all the photomultipliers tested here had dark noise rates of less than 4 kHz. Once the normal operation of the photomultiplier had been established by the measurement of parameters such as TTS, dark noise and gain, the photocathode was scanned with the Čerenkov source. In an attempt to reduce systematic error, the order of measurement of the angles was determined randomly in advance of the experiment. The pointer which adjusts the angle of the source with respect to the photomultipliers was always moved in the same direction (from negative angles to positive) to avoid backlash errors. However the setting of the position of the source did not suffer from significant backlash.

The coincident noise background was continually measured during the data taking. The background was estimated by moving the source to the $-90°$ position[3], at which the photocathode was not illuminated. This was used as a 'source off' position. The coincidence noise rates observed were always verified to be consistent with those predicted from the random coincidence formula, $C = n_1 n_2 \tau$, for independent noise rates n_1 and n_2 and resolving time τ. No significant cross-talk was observed. An estimate of the efficiency of the photomultiplier and discriminator to detect photons was made by taking four counts at positions OFF, ON, ON, OFF, where the ON position is the angle of interest. This order was chosen so that drift in the random noise rate of the photomultiplier cancels to first order (linear). Since the noise drifts observed were extremely small, this procedure was more than adequate. All counts referred

[3]Note that this angle refers to that between the source and the axis of the R1408 photomultiplier.

to in this experiment were based on a 100 second time interval.

7.1 Resolution and uncertainties

There are several sources of systematic uncertainty associated with the geometry of the source and photomultiplier arrangements. In particular, the measured efficiency as a function of position is the actual efficiency convoluted with the resolution function which describes the width of the light 'spot' on the photocathode. A black tape mask of width 18 mm was fixed to the photocathode (of photomultiplier GG3077) to estimate the width of this resolution function and to confirm that the translation between angle measured and position was consistent. The position of the tape was chosen so that one edge of the mask was near the transition angle $\theta_t \simeq 39.56°$ where the radius of curvature changes from about 126 mm to about 60 mm. The other side of the tape mask lies at an angle of about 50°, in the region of particular interest for reflector design. As before, angles are measured with respect to the axis of the photomultiplier. The position of the black mask is shown in Figure 7.1.

Figure 7.2 shows the data obtained from a scan of photomultiplier GG3077 with the black mask in place, and the lower graph in Figure 7.2 shows an enlargement of the region near the mask. From these data the position of the source cut-off can be deduced and corresponds to that of the mask edges to within uncertainties (a couple of mm). The principal limitation of this test is the measurement of the position of the mask in relation to the meridian of the photomultiplier. The width of the resolution function can be determined crudely from the slope of the intensity/angle at the edge of the mask. Hence we may deduce that the full width at half maximum of the resolution function is about 2 mm at 42° and about 4 mm at 50°. As expected the width of the resolution function increases at large angles (greater than θ_t) as the source moves off the surface of the photomultiplier. The width of the resolution function will increase in the region up to the aluminised layer. The width could be as wide as 7 or 8 mm in the direction tangential to the surface of the photomultiplier bulb.

Random fluctuations influence both the accuracy to which the angle pointer can be adjusted and read, and also the number of counts observed at each angle. An estimate of the setting accuracy of the source position can be deduced from the steep fall of count rate with decreasing angle at $-42°$ with the black mask in place. The total setting accuracy is consistent with a standard deviation of about 0.5° or about 1 mm along the surface of the photomultiplier. Since the signals recorded are always the result of coincidence from two photomultipliers, time-correlated signals (such as afterpulsing) from each photomultiplier are not important and therefore Poisson statistics should provide a good estimate of the error of the total observed count rate. On this basis, the typical standard error would be of order of 50 counts in 100 seconds, i.e. about 1% of the signal. A test was devised which would estimate this standard

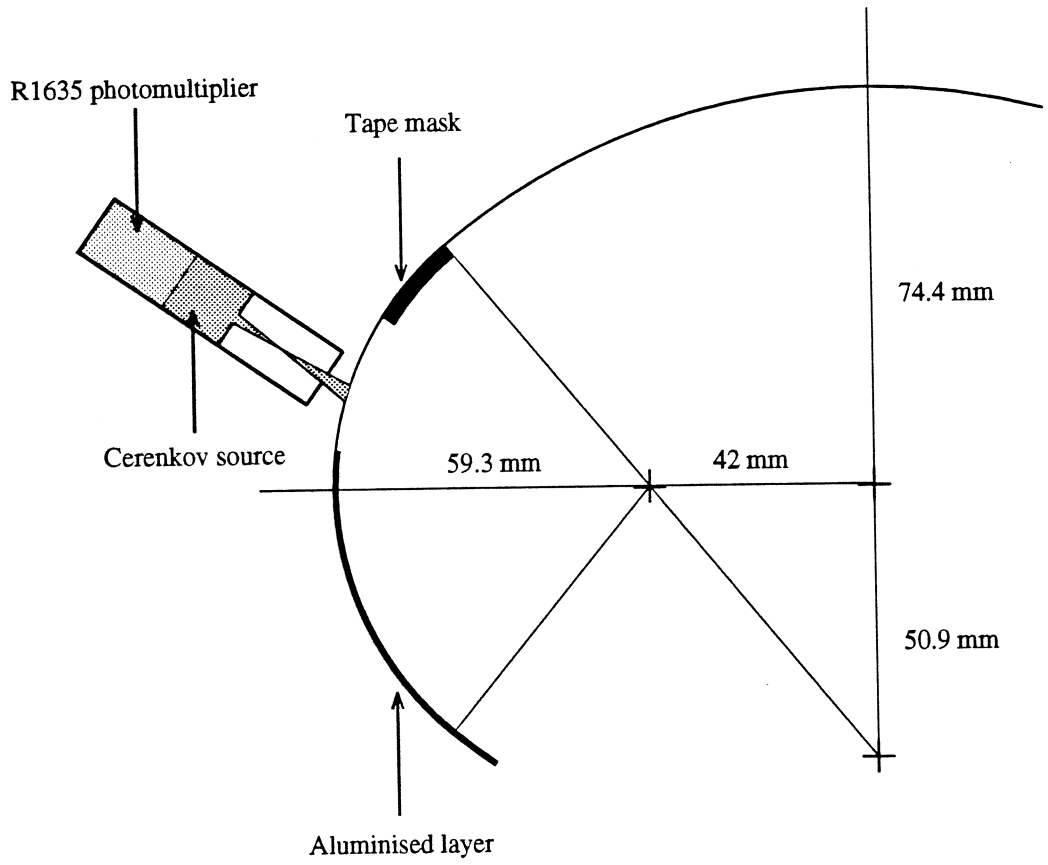

Figure 7.1: Shape of the Hamamatsu R1408 photomultiplier bulb. The approximate position of the black mask used on photomultiplier GG3077 is shown. The dimensions are those deduced from measurements of the bulb shape.

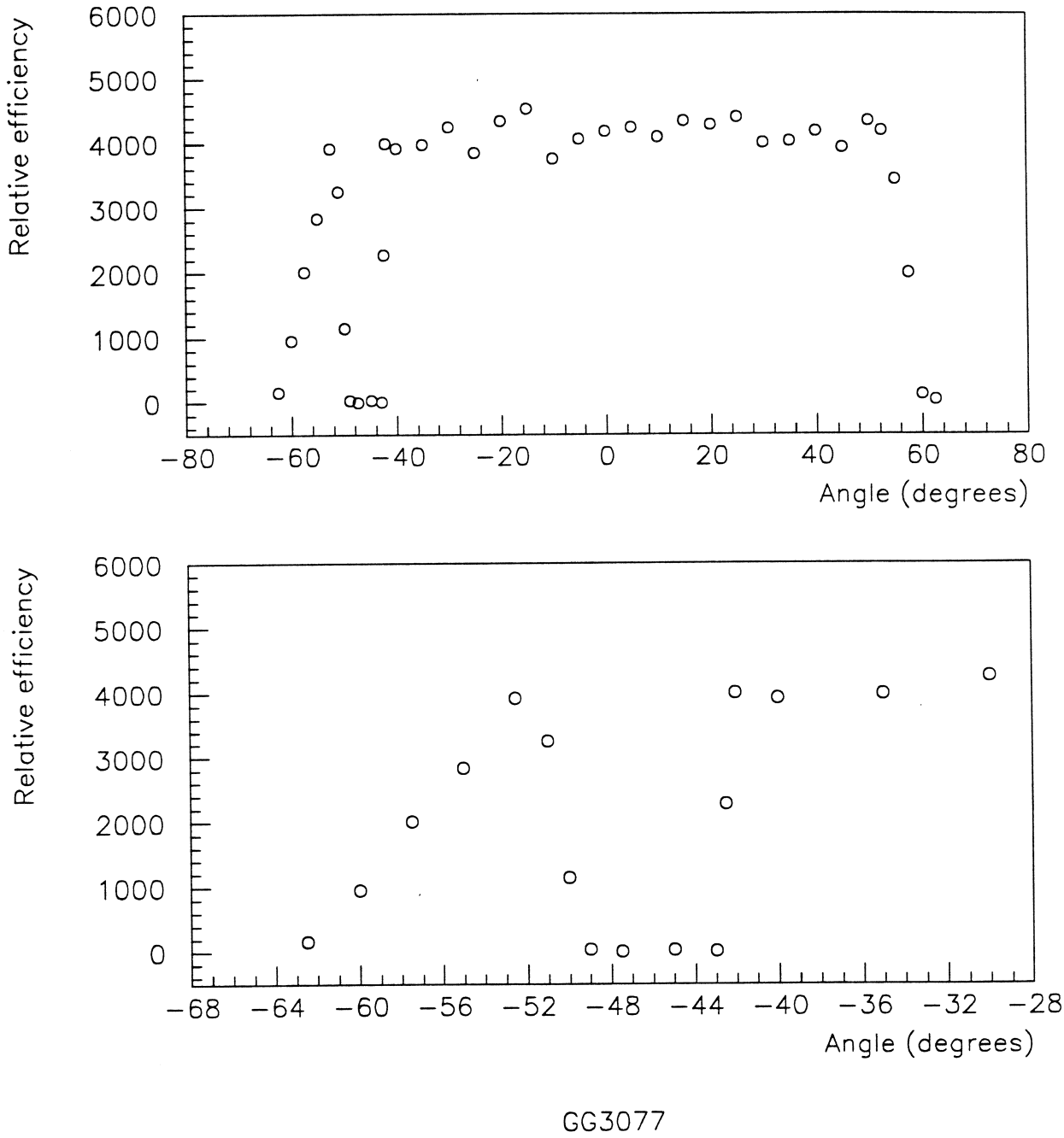

Figure 7.2: Photocathode scan of GG3077. The interval $-50° \rightarrow -42°$ was masked with black tape and the lower graph shows the data in this region. The positional accuracy is good at the level of 2 mm, and the resolution is 2 mm at 42° and 4 mm at 50°.

Start time	Reading number	Net counts in 100 s
11:19 am	8	2719
12:32 pm	16	2768
12:58 pm	19	2889
3:34 pm	35	2820
4:02 pm	38	2852
Estimate of Mean $\bar{x}$		2809.6
$\sigma_{n-1}(x_i)$		60.25
$\sigma_{n-1}(\bar{x})$		30.13

Table 7.1: Random fluctuations of scan measurements.

error with the typical contribution from the error due to angle setting. During the course of measurements of photomultiplier CB0265, five independent measurements of the count rate at an angle of $-55°$ were taken. The count rate changed relatively quickly with position in this region, so that angular setting errors would also influence the observed spread of values. These five measurements were taken using similar procedure as other points, interleaving them with the normal pattern of points at random intervals. The results are shown in Table 7.1. The parameter $\sigma_{n-1}(x_i)$ shows an unbiased estimate of the standard deviation of the single measurement (population) distribution, whereas the parameter $\sigma_{n-1}(\bar{x})$ shows an unbiased estimate of the standard deviation of the mean estimator $\bar{x}$. The single measurement error $\sigma_{n-1}(x_i)$ of about 60 counts in 100 seconds is consistent with the estimated value of 50 counts in 100 seconds.

7.2 Scan results

Before each photomultiplier was scanned using the source, the operating parameters were measured to ensure the tube was operating correctly. With the source spot at 0°, the spot scan parameters were recorded, and these are shown in Table 7.2. Column 3 of the table shows the total voltage applied to the photomultiplier in order to achieve a gain of 10^7, but note that an additional voltage is dropped across the 100 kΩ resistor in the signal pick-off circuit which makes the required power supply voltage greater than the figures quoted in the table. Column 4 shows the full width at half maximum of the transit time spread distribution in nanoseconds,

Experiment date	Serial number	Total volts	TTS (ns)	Noise (kHz)
27th September	CB0270	1700	N/A	3.0
1st October	GG3070	1830	3.04	1.2
2nd October	CB0273	2370	3.11	1.2
3rd October	GG3077	2120	3.04	2.5
4th October	CB0265	2270	2.80	4.0

Table 7.2: Photomultiplier spot scan parameters.

for a spot illumination. Note that the transit time spread times recorded here are smaller than those for total illumination of the photomultiplier front window reported in Chapter 6. The right hand column shows the dark noise rate in kHz after about 16 hours of operation in the dark, although the noise rate could be reduced slightly with further dark operation.

Figure 7.3 show the results of the photocathode scan for these Hamamatsu R1408 photomultipliers with SNO bases. The errors on each point are approximately 60 counts in 100 seconds. It is clear that there are local variations of photocathode sensitivity which are statistically significant. However, it is likely that their nature is random and that the average photomultiplier response will be flat in the region inside the boundary of the photocathode. The determination of the position of the photocathode boundary will be considered further in the next section.

The radial extent of the photocathode has implications for the maximum lower diameter of the reflectors to be used on the SNO photomultipliers. For this reason it is required that the measurements of angle be converted to effective polar radius from the axis of the photomultiplier, and this in turn requires accurate knowledge of the photomultiplier bulb shape[4]. The bulb is made with radius of curvature of 126 mm for $\theta < \theta_t$ and 60 mm for $\theta > \theta_t$, where $\tan\theta_t = a/c$, see Table 7.3. The centre of the smaller circle is given as 42 mm from the axis of the photomultiplier. The bulb is the resulting surface of revolution.

The bulb dimensions used are shown in Table 7.3. Using these values the polar radius $r(\theta)$ may be deduced from the measured angle as follows: For $\theta < \theta_t$ the radius is simply given by $r(\theta) = (c + d)\sin\theta$. For larger angles the polar radius is given by

$$r(\theta) = \frac{(a + c\cot\theta) + [(a + c\cot\theta)^2 - (1 + \cot^2\theta)(a^2 - b^2 + c^2)]^{1/2}}{1 + \cot^2\theta} . \qquad (7.1)$$

Using this relation it is possible to compute the radii as a function of theta for the angles

[4]The photomultiplier bulbs are made by Schott subject to drawing number A5349-00-02d.

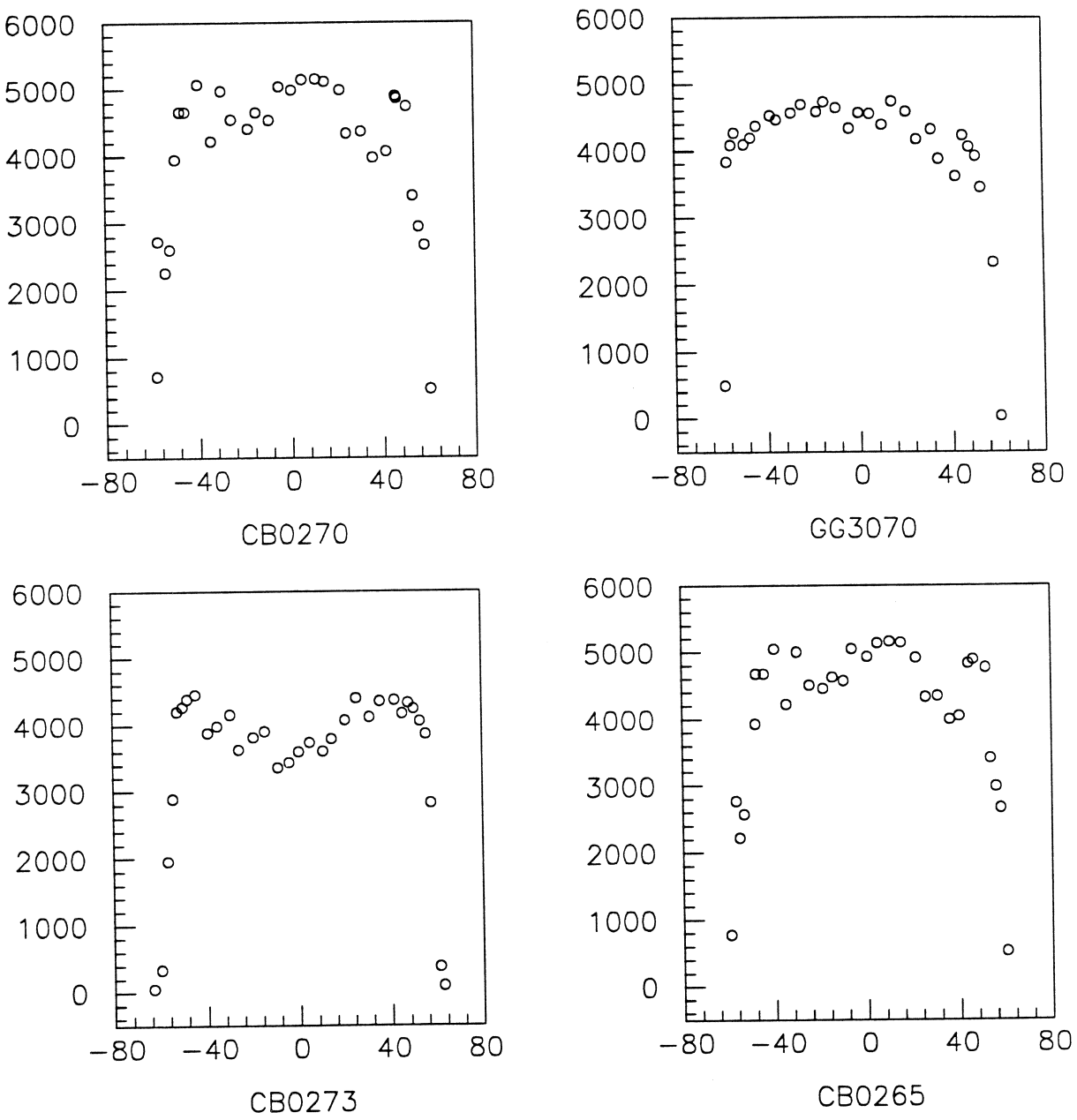

Figure 7.3: The results of the photocathode scans as a function of angle. The relative efficiency is shown on the ordinate axis expressed in terms of the number of counts observed in 100 seconds. The standard deviation of this figure is about 60 counts in 100 seconds.

Shape parameter	Schott value (mm)	Value used (mm)	Label
Radius of curvature ($\theta < \theta_t$)	126	125.3	$c + d$
Radius of curvature ($\theta > \theta_t$)	60	59.3	b
Top of photocathode to equator along the photomultiplier axis	75.1	74.4	d
Distance from photomultiplier axis to centre of curvature for $\theta > \theta_t$	42	42	a

Table 7.3: Hamamatsu R1408 bulb shape parameters.

measured. In order to assess the data from all five photocathode scans, these data sets have been averaged and the results plotted as a function of radial distance from the photomultiplier axis. These data are shown in Figure 7.4. The error bars on the points are estimators of the unbiased standard deviation of the mean number of counts measured in 100 seconds. Of course the single photomultiplier distribution will vary by an amount $\sqrt{5}$ larger than the displayed error bars. Near the edges of the photomultiplier the count rate falls rapidly with increasing polar radius, so enlargements of these regions are shown in Figure 7.4 for negative and positive radii.

These figures clearly show that the photocathode extends almost all the way to the photomultiplier equator. The data are consistent with a photocathode which is quite uniform on average, but has local deviations from this average. It should be noted that the experimental resolution was broadened when the source was not in contact with the photomultiplier. In this case the resolution was about 8 mm multiplied by the cosine of the angle of the normal with respect to the photomultiplier axis, at each point. Near the edge (say $r = 100$ mm) this resolution width was only about 1.5 mm in polar radius. This is consistent with the shape of the observed efficiency near the edge of the photocathode, see Figure 7.4. By considering the impact of the photocathode response for reflector performance, a decision has been made to use an area of the photocathode of diameter 196 mm. The criterion used was that the reflectors should maximize the amount of light collected, but the optical efficiency at the centre of the detector should not be significantly degraded. All of the photomultipliers tested here have a cathode response function which is sufficiently uniform to satisfy this criterion.

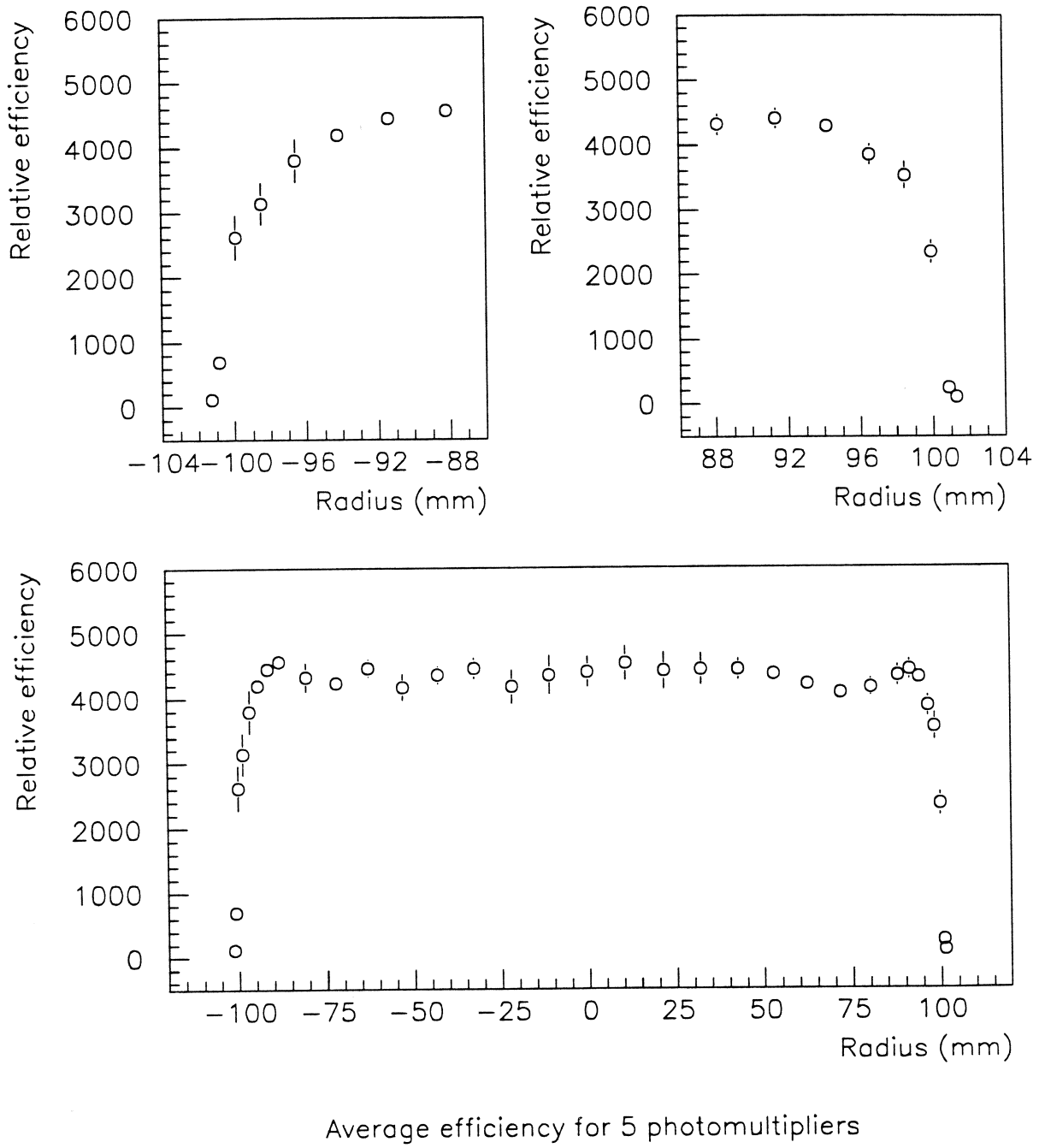

Figure 7.4: The lower plot shows the average of the photocathode scans as a function of cylindrical polar radius. Positive radii correspond to positive angles. The relative efficiency is shown on the ordinate axis. The upper plots show enlargements of the edge regions.

Chapter 8

Calibration of the SNO detector

In order to measure the flux of electron neutrinos from the sun, the response of the SNO detector to electrons and γ-rays as a function of their energy, location and initial direction must be known. To measure the total neutrino flux from the sun via the neutral-current reaction $\nu_x + d \rightarrow n + p + \nu_x$ the efficiency for the detection of neutrons must also be known as a function of position within the detector. These properties are to be measured *in situ* using calibration sources and these data will then be incorporated in the SNO Monte Carlo and Analysis (SNOMAN) software [102]. In this chapter a brief review of SNO calibration methods is given with a description of a prototype scintillator source built by the author. The development work needed before the sources described in this thesis can be used in the SNO detector is described. A review of the prospects for calibration using the techniques described here is also given.

The acute dependence of the inferred neutrino flux on the calibration of the absolute energy scale of signal from the SNO detector requires that this scale is established with small error. The required accuracy is not known precisely, as the energy spectrum of the ^{8}B electron neutrino energy spectrum may be distorted by neutrino flavor oscillations via the MSW mechanism. Indeed the measured neutrino energy spectrum will be used to deduce (or put limits on) the MSW parameters $(\Delta m^2, \sin^2 2\theta)$. It should also be remembered that the variations of the cross-sections of both the deuteron neutrino interactions are more energy dependent than the electron scattering reaction measured in other water Čerenkov detectors such as Kamiokande II. Also the fraction of neutral-current events recorded by virtue of neutron capture is very sensitive to the energy threshold. It is clear from simulation that an absolute energy calibration at the few percent level is required.

As discussed in Chapter 1 many authors have suggested that the data from the Chlorine experiment of Davis *et al.* show a temporal correlation with the sunspot number; presumably via the effects of solar magnetism. SNO will look for such temporal deviations in the measured neutrino flux and this requires that the response of the detector is calibrated regularly. It is

also vital that if the neutral-current signal is measured by frequently alternating the salt concentration, the energy response is recalibrated every time such a change is made.

In order that a source may be used in the detector it must have the following attributes:

1. Every source should be safe and should not introduce contamination into the detector, especially radioactivity. Radioactive sources should be strong, mechanically secure, and reasonably safe to personnel handling them.

2. The source should be constant in intensity, or at least vary in a known way.

3. The source should be made as compact as possible to aid its installation and movement within the detector.

4. Wherever possible a source should not introduce significant deadtime into the detector or otherwise render it unable to detect neutrino interactions from a supernova during calibration. This constraint could be relaxed for sources which need to be in the detector for a negligible time.

5. To measure the TTS of the photomultipliers any 'source' (radioactive or otherwise) must have the shortest possible pulse duration.

The SNO collaboration is also investigating the use of fixed light sources mounted on the photomultiplier support structure which would not be mobile. These sources are more diagnostic tools rather than calibration sources. The next section reviews some proposed calibration sources and techniques.

8.1 Calibration sources

The most satisfactory method of calibration of the response of the SNO detector to Čerenkov radiation would be provided by a source of mono-energetic electrons with constant flux, known variable energy and direction, which could be placed anywhere in the detector volume. Unfortunately the difficulty of placing an electron linac or similar device in the detector forces an alternative approach to be used. Various γ-ray sources (and other light generating sources) will be placed in the detector and the results used to 'calibrate' the SNOMAN Monte Carlo and Analysis code. This is achieved by adjusting the 'internal' parameters of the code so that agreement with the measured angular resolution and Čerenkov yield of the γ-ray shower is restored. The same simulation parameters should yield agreement for all the sources used.

Ideally several γ-ray sources covering the energy range 5 to 25 MeV would be used; a summary of some proposed γ-ray sources in shown in Table 8.1. The lower end of the energy range is provided by several candidate nuclei via radiative thermal neutron capture (n,γ).

Reaction	Ref.	cross-section	γ-ray energy	Initiator
^{3}He(n,γ)^{4}He	[103]	$\approx 50\mu$b	$\simeq$ 22 MeV	Fast neutrons from ^{252}Cf
^{7}Li(α,γ)^{11}B	[104]	25 μb	10.3 MeV	Low energy α from ^{148}Gd
Ni(n,γ)Ni	[105]	4.4 b	6.1 to 9.0 MeV (line spectrum)	Thermal neutron capture
^{35}Cl(n,γ)^{36}Cl	[106]	43 b	8.6 MeV	Thermal neutrons
^{2}H(n,γ)^{3}H	[106]	0.53 mb	6.25 MeV	Thermal neutrons

Table 8.1: Summary of proposed γ-ray sources.

A useful table of the cross-sections and branching ratios of such reactions is given in [106]. Higher energy γ-rays are more difficult, but the fast neutron capture on ^{3}He provides a γ-ray of approximate energy $\approx$ 22 MeV[1]. The basic designs of all these radiative neutron capture sources are similar: neutron capture nuclei are encased with a neutron source (with moderator if necessary) inside a neutron-absorbing outer casing. The neutron source may itself need to be clad in a lead shield to attenuate prompt fission γ-rays. For details see Leslie *et al.* [107].

It is important that neutrons do not escape from the source as these will give rise to ^{2}H(n,γ)^{3}H neutron capture reactions in the heavy water and produce unwanted γ-rays. Naturally, a source of neutrons (such as ^{252}Cf) could be placed in the D_2O providing a test of the neutron transport properties of the detector in addition to a source of 6.25 MeV γ-rays. This neutron transport calibration is complicated by the greater energy of neutrons from a fission source compared to those produced from the neutral-current $\nu_x + d \rightarrow n + p + \nu_x$ reaction with solar neutrinos, but the higher energies can be incorporated into the Monte Carlo simulations. These simulations [55, Annex 1] indicate that it is the behaviour of the neutrons at low energies that is most important for estimating the fraction of neutrons which capture in the D_2O. These calibrations will be done with and without salt (^{35}Cl) added to the heavy water.

Another approach is to use the strong resonance of the radiative α capture reaction ^{7}Li(α,γ)^{11}B for an α energy of about 2.6 MeV. This has the attractive feature that it is below the neutron production threshold of 4.2 MeV from the reaction ^{7}Li(α,n), and so an α particle of intermediate energy would give a γ-ray source free from neutron background[2]. Unfortunately, the cross-section is rather small and a simple calculation shows that only a

[1] If a source of 20 keV protons was available then the isobaric analogue reaction ^{3}H(p,γ)^{4}He would also provide this 22 MeV γ-ray.

[2] Naturally any materials used in the source would also have to have a high (α, n) threshold.

fraction $\simeq 2 \times 10^{-9}$ of the incident α particles would produce a high energy γ-ray. At least 5 MBq of ^{148}Gd would be required to give a useful flux of γ-rays. If using a higher energy α decay and degrader foil is unavoidable, the resulting source could still be useful in the light water region provided that the neutron flux is not too great.

There is a further requirement for other calibration sources which provide a quicker calibration with greater spatial accuracy within the detector. To this end an optical pulser and a ^{241}Am - scintillator source are being built to provide routine calibrations of the detector. The optical pulser will provide a short burst of photons of duration ($\sigma \simeq 0.5$ ns) placed at a known position within the detector. This will enable the relative time shift of each photomultiplier channel to be measured along with the TTS of each photomultiplier. Further, the relative efficiency of the photomultipliers can be measured.

The light source is a Laser Photonics LN120C nitrogen laser pulsed at 60 Hz delivering a $\simeq 70$ μJ burst of 332 nm photons. The wavelength of these photons is slightly too short for the long length of fibre optic cable required to transmit the pulse to a diffusing sphere in the detector without distortion of the pulse shape. This is because the cable is slightly dispersive at these short wavelengths and the time duration of the pulse is thereby increased significantly. Therefore the laser pulse is used to excite a dye laser (LD1C) to act as a wavelength shifter increasing the wavelength to about 400 nm. Leslie *et al.* have demonstrated that when using graded index optical cable with wavelength shifted photons the duration of the light pulse is negligible in comparison to the TTS of the photomultipliers. Finally the pulse amplitude will be variable so that between (say) 10 and 10^7 photoelectrons can be produced in the detector in total to check gain, thresholds and photomultiplier charge resolution. If these tests were to be performed once per week the deadtime for counting solar neutrinos would be a small fraction of 1%.

The optical pulser described above will not be able to monitor any changes in the optical efficiency of the detector with time as the light output of the laser cannot be stabilized to the required level. Thus there is a further requirement for a compact isotropic optical calibration with a source of constant (preferably known) light output. This source should also have a suitable wavelength dependence matched to the Čerenkov λ^{-2} spectrum. Two types of source are suggested to satisfy these requirements, namely an ^{241}Am - scintillator source and an ^{90}Sr - water source. An example of the latter type, the Mark 3 source, was described in Chapter 4. It should be noted that this type of source has the disadvantage over the γ-ray source that single events cannot be reconstructed by the detector as the number of photomultiplier hits will not be above the threshold. Hence the signal will have to be taken from the increase in the noise rate of each photomultiplier. This signal will have to be corrected for the reflections from the photomultipliers and other support structure materials which would normally be excluded

by the 100 ns time window of the electronic trigger system. However it has the advantage over the γ-ray sources that it is more compact and hence could be easily moved around within the detector. The Mark 3 Čerenkov source is also a smaller source from a optical point of view as it does not rely on γ-rays stopping in the water. It will ideal for estimating the attenuation of the acrylic vessel as it can also be used in the light water volume (provided that the optical attenuation of the glas bulb of the source can be made negligible). Unlike the pulsed laser system, both the Mark 3 source and the Alpha - scintillator source have the advantage of being constant in light output. The Mark 3 source has the further advantage of having a Čerenkov λ^{-2} photon spectrum with known intensity.

8.2 Alpha - scintillator source

The motivation behind an alpha - scintillator source is that a routine (i.e. low detector deadtime) calibration light source should be available which has a constant light output over many years. Also this source should produce enough photons (and hence photoelectrons in the photomultipliers) in a single pulse to exceed the hardware data acquisition trigger of the detector. If possible the number of photons emitted per alpha decay should vary as little as possible, given the restriction of statistical chance.

As the range of alpha particles is so short, surface effects dominate the fraction of the track spent in a scintillating medium. In particular, if some material containing the alpha radioactivity was in the form of aggregates (in the scintillating medium) which were not small compared to the track length of an alpha particle, then there would be a large variation in the amount of scintillation light produced by the decays. A similar argument holds for material on the walls of a container of liquid scintillator. These problems lead to the choice of alpha decay isotope dissolved in a scintillator, and hence a liquid scintillator. However, the properties of some liquid scintillators are not constant with time in real sources as either they, or the commonly added wavelength shifters, are vulnerable to oxidative chemical reactions.

For these reasons the choice of which liquid scintillator (with appropriate wavelength shifter) to use is dictated by the following requirements.

1. The scintillator light output per alpha decay should be as stable as possible, and certainly within 1% per year.

2. The scintillation decay time should be as short as possible, and definitely less than 4 ns.

3. The scintillator must have sufficient light yield per alpha decay to always trigger the data acquisition system. The light yield should be equivalent to the Čerenkov radiation from a 10 MeV electron.

Ingredient	Function	Fraction	Composition	M.W.	B.P.	λ_m (nm)
Toluene	Scint.	2/3	C_7H_5	92.14	110.6°	430
Triton X-100	Surfact.	1/3	Ethoxylated Iso-octylphenol	-	> 110.6°	-
PPO	λ Shift.	4 - 7 g/l	$C_{15}H_{11}NO$	221.26	> 360°	365
POPOP	λ Shift.	0.1 - 0.2 g/l	$C_{24}H_{16}N_2O_2$	365.4	high	415

Table 8.2: Ingredients of the KL-402 liquid scintillator cocktail.

4. It should be available in a form which which will dissolve small quantities of weak acid, as nuclides are commonly available in this form.

5. The optical attenuation length of the scintillator should be at least 10 cm for wavelengths of greater than 300 nm. This criterion becomes important if the source is to be used outside the acrylic vessel.

A prototype source was made using a commercially available organic scintillator cocktail manufactured by Koch Light Ltd. The cocktail used, known as KL-402, is based on scintillation grade toluene, to which several wavelength shifters are added. KL-402 also contains a surfactant, Triton X-100, which enables large amounts of aqueous solution to be dissolved in the solution. The constituents of KL-402 are shown in Table 8.2, along with their molecular weights and boiling points. The last column shows the wavelength of the peak light output in the case of the toluene and the peak efficiency in the case of the secondary solutes. The average wavelengths are slightly longer than the peak wavelengths quoted in the table. Toluene is a relatively fast scintillator with a decay time of about 3 ns, and yet has a respectable light yield (about 70% of anthracene); for a comprehensive account see Birks [108]. The spectrum of scintillation light from a Toluene scintillator is shown in Birks, with data about the enhancement of light yield with the addition of wavelength shifters and also the degradation induced by oxidation of the cocktail.

This scintillator was used with a solution of ^{241}Am dissolved in 0.1 M nitric acid. The choice of isotope was dictated by a lack of high energy γ-rays produced in the ^{241}Am alpha decay (only 60 keV γ-rays) and its common availability. A small sample of the solution containing the ^{241}Am was dried on a steel disk and counted in an Ortec 576A alpha spectrometer. Since the energy resolution of the counter is very good (30 keV for FWHM) it was possible to rule out significant contamination with other alpha decay isotopes. The optimum amount of the

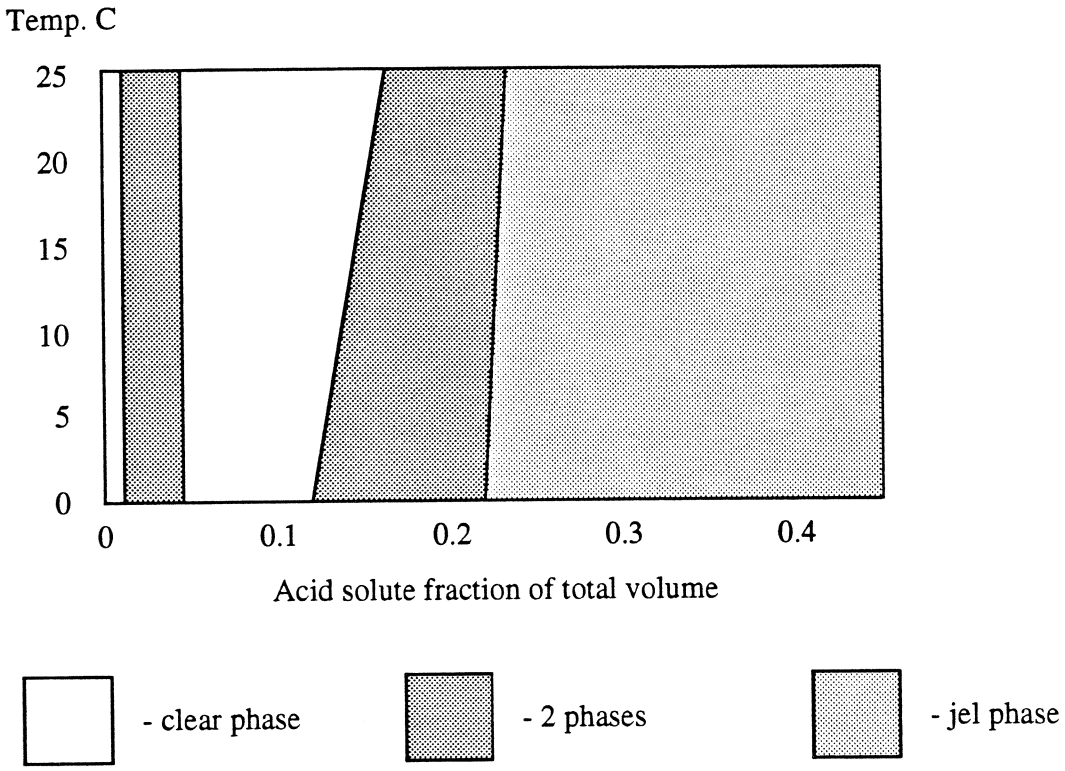

Figure 8.1: The phase diagram for KL-402 for amounts of dissolved 0.1 M acid.

acid solution to be added to the cocktail was determined by the requirement that the resulting solution was in a single clear phase. The phase diagram for the KL-402 cocktail was given by the supplier and this is shown in Figure 8.1 for the case of a 0.1 M nitric acid.

The diagram shows the phase of the mixture/solution as a function of temperature in °C and with the amount of nitric acid added expressed as a fraction of the total. For scintillation counting the large 'clear phase' is required, and so the radioactive solution should form about 10% of the final solution. It may be possible to count in the gel phase, but since the ^{241}Am must be completely dissolved this was not considered to be likely to produce a satisfactory source. Finally it should be noted that the upper end of the clear phase should not be used as the phase change boundary is somewhat temperature dependent and a source to be used in the SNO detector would have to be stable with respect to temperature changes in the range + 5 to + 40°C.

Two pilot sources were made in an attempt to demonstrate that a scintillator source can be made which satisfies all the above criteria. They were made by mixing 4 ml of KL-402 scintillator cocktail with differing amounts of the ^{241}Am solution and de-ionized water to adjust the aqueous sample fraction. A polycarbonate scintillation phial with a air-tight seal was used. Since the exclusion of oxygen is critical to the long term stability of these sources, they were flushed with argon immediately before sealing. The plastic seal end-cap was glued

Source	402	^{241}Am sol.	H_2O	Sample fraction	Comments
1	4 ml	0.25 ml	0.4 ml	0.14	Milky solution - unsuitable
2	4 ml	0.2 ml	0	0.05	Single clear phase - suitable

Table 8.3: Mixing fractions of two pilot ^{241}Am sources.

in place to provide more security to prevent oxygen leaking in or radioactivity leaking out. Finally the phials were sealed in a glass flask for further safety. The contents of the two pilot sources are shown in Table 8.3. At ambient temperature of about 18°C the second source proved to be successful; i.e. a single clear phase. About 20 kBq of ^{241}Am was present in this solution.

If such a scintillation source is to be successful it must produce enough photons in each pulse to simulate the Čerenkov radiation from an electron of order 10 MeV. Furthermore the distribution of the number of photons produced in such decays should be as small as possible; the resolution should be better than 20%. A measurement of the optical pulse height spectrum was done by photon counting the second scintillation source with a photomultiplier tube in near 4π counting geometry. To increase the light collection, an EMI 9350 200 mm photomultiplier with an optical reflector was used. In addition a sheet of the aluminium mirror reflector (similar to that used for the SNO concentrators) was used behind the source to ensure that a large fraction (estimated at about 80%) of the photons were incident on the photocathode. The counting geometry is shown in Figure 8.2. The pulse counting electronics used were similar to those described in Chapter 5. The × 10 amplifier was replaced by a × 0.5 attenuator as the pulses from the photomultiplier produced several volts across a 50 Ω load.

The distribution of pulse heights was recorded by a LeCroy qVt 3001 multichannel analyser used in 'q' mode as an ADC, and this was calibrated in the same way as described previously. The gain of the photomultiplier was measured in single photon counting mode. Hence an estimate was made of the number of photomultiplier hits that would be caused by this source in the SNO detector. The raw data from the pulse height spectrum from the ADC is shown in Figure 8.3 for the second scintillation source. Each channel of the ADC represents 0.25 pC, and the gain of the photomultiplier is such that each photoelectron corresponds to about 3.2 ADC channels. Hence the peak at ADC channel 554 corresponds to about 173 photoelectrons at the gain level used.

It was found that the pulse height spectrum could not be well characterized by a simple Gaussian fit to the data. A satisfactory fit was obtained with a skewed kurtosoidal Gaussian

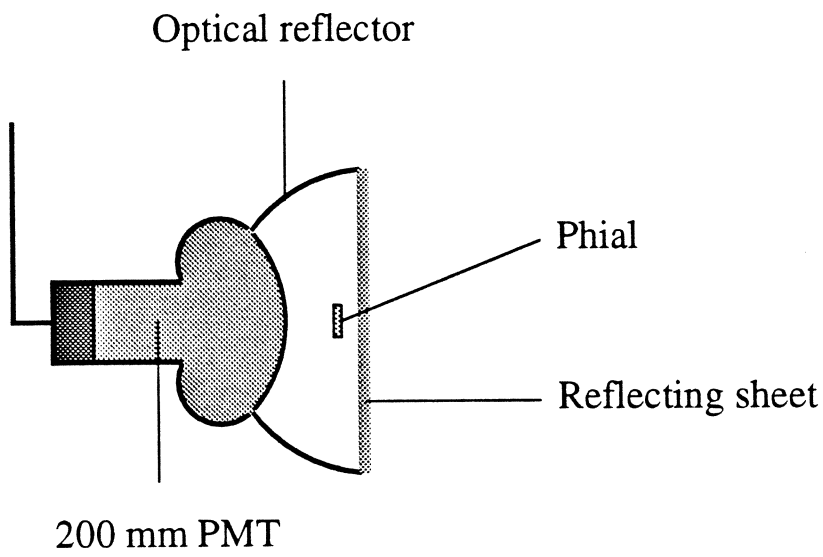

Figure 8.2: The counting geometry for scintillation counting.

similar to that in Chapter 6 of the form

$$h(n) = A \exp\left[-\frac{1}{2}\left|\frac{n-n_0}{\sigma - s(n-n_0)}\right|^{\gamma}\right] + (Bn + C), \tag{8.1}$$

where n is the channel number, A represents the peak height and the term $(Bn + C)$ represents a fit to a linear background. The centroid parameter n_0 depends on the amount of light produced per decay. The width of the peak is expressed by the parameter σ and this should be as small as possible. The degree of 'skewness' and kurtosis are described by the parameters $s = 0.072$ and $\gamma = 1.9$ respectively.

A fit of this form between channels 350 to 800 produces a satisfactory fit, although the ignorance of the backgrounds increases the χ^2 of the fit to about 3 per degree of freedom. It was found that outside this region the shape of the pulse height distribution was not well described by Equation (8.1), particularly on the low energy (low channel number) side of the peak. Some of the peak just above the discriminator channel (10) is caused by noise within the photomultiplier, although this cannot explain the broad valley between channels 80 to 360. It is possible that this may be caused by the production of 60 keV γ-rays in the ^{241}Am decay.

The results of a MINUIT fit in this range was that the centroid parameter was determined to be 553.7 channels, which is equivalent to about 173 photoelectrons. Given that the efficiency of counting photons in this apparatus is thought to be similar to that in the SNO detector, this would produce the same number of photomultiplier hits as a 20 MeV electron in the centre of the heavy water. This represents the top of the equivalent energy range for such a source; as weaker sources (in terms of photons per alpha decay) can be made by diluting the scintillation cocktail with more Triton X-100. Hence a series of such sources could be made with equivalent

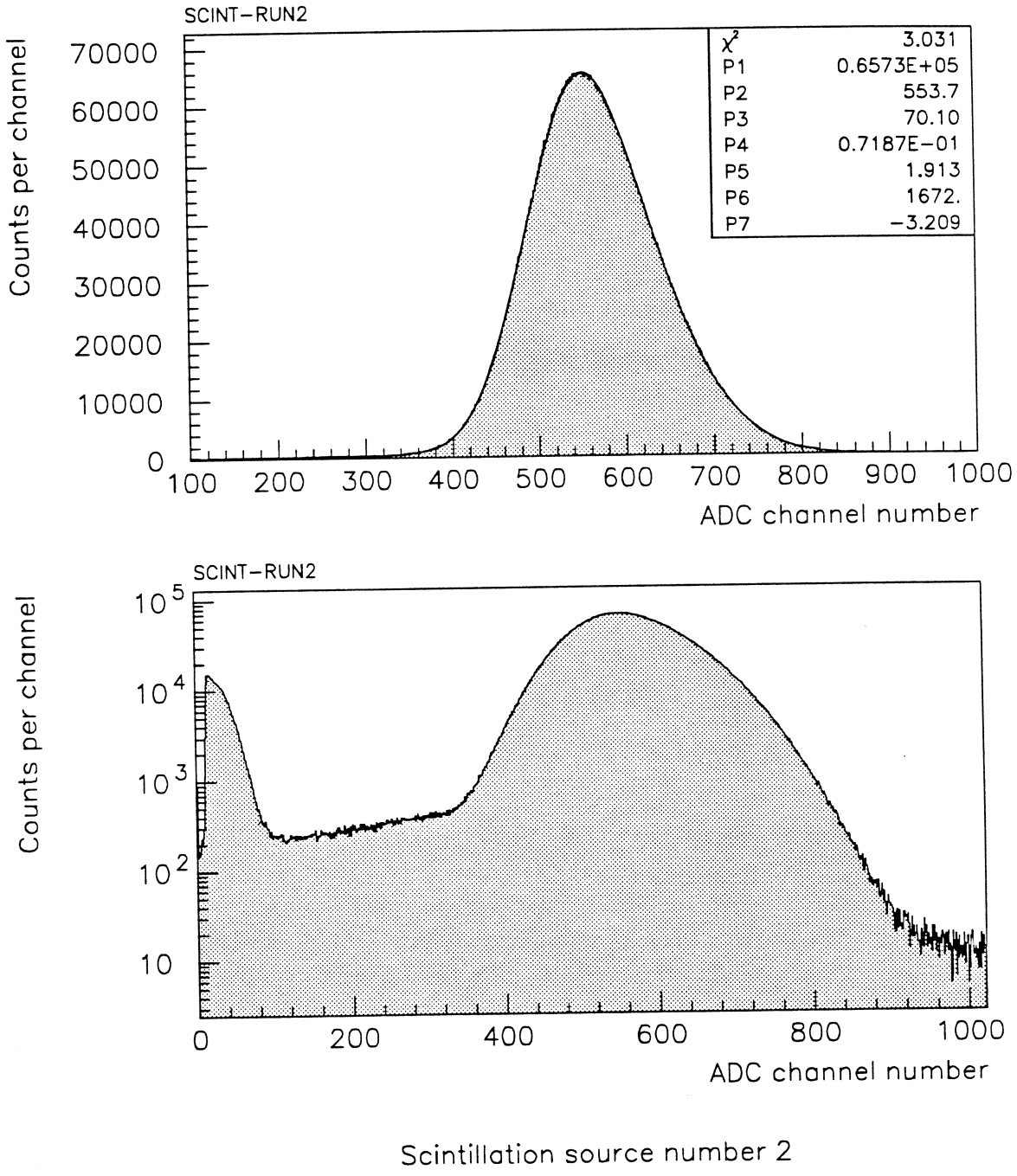

Figure 8.3: The upper plot shows the pulse height spectrum with a fitted skewed kurtosoid Gaussian between channels 350 and 800; see text. The lower plot presents the data logarithmically to show the tails of the distribution.

light output of electrons in the whole energy range of interest to SNO. In a glass walled source slightly more ultra-violet light may be available by virtue of its superior optical transmission in the ultra-violet. A source with more ultra-violet light may be desirable as this gives a test of the transmission/reflection of the optical components of the detector over a wider range of wavelengths.

The Minuit fit gave a value of 70.11 channels (22 photoelectrons) for the width parameter σ. This may be expressed as a resolution (i.e. σ/n_0) of 12.7%. This is a most satisfactory result but one should bear in mind that this fit is only valid in the region between channels 350 to 800 and so the fit value of σ does not express the size of the tails of the distribution. However this value of σ should be interpreted as the upper limit of the width parameter as the contribution from the charge resolution of the photomultiplier has not been subtracted from this value[3]. The sharply peaked nature of the pulse height spectrum makes this source an ideal candidate for a routine calibration source.

There seems to be little doubt that the stability of the light output of the scintillation source over several years should be investigated closely. After a six month period a sample of the scintillation cocktail which had been sealed under argon but with a poor quality (glass-plastic) air seal had degraded. This degradation may be due to the either scintillator or wavelength shifter being oxidized. A sample with a superior glued seal, also sealed under argon was found not to have suffered in this respect after six months. The latter was still visibly fluorescing in sunlight, whilst the former was not. This underlines the importance of a high quality seal of the scintillation phial in the presence of argon.

If more confidence in this type of source is to established then further work must be done to address the following concerns.

1. An apparatus to monitor the light output of the scintillator over a period of time should be established. This is a difficult task, as such apparatus should be stable at the percent level for a period of at least one year. This is a critical measurement tool which permits detailed investigation of the source properties.

2. The phase diagram of the scintillation cocktail used should be investigated, and the chosen point should be shown to be stable between 5 and 40°C.

3. The permitted level of oxygen contamination in the final sealed scintillation phial should be established. If necessary the phial could be sealed in the presence of argon after outgassing the cocktail mixture.

4. A suitable phial material should be established which is mechanically strong enough,

[3]This procedure yields a model-independent upper limit on the resolution of the scintillation source.

resistant to attack from the scintillation cocktail (especially toluene) and has adequate optical transmission in the ultra-violet.

8.3 Conclusions

In Chapter 3 the computations of yields of Čerenkov radiation from Monte Carlo simulations was shown to be consistent with a simple analytic model of a stopping electron in a transparent medium. The limiting uncertainties in the computation were shown to be from the knowledge of the stopping power of electrons in various media and the assumptions about the optical properties of the media. It seems likely that the Čerenkov yield from low energy electrons (2 MeV) can be calculated at the few percent level.

In Chapter 4 a candidate source (Mark 3) of Čerenkov radiation was reported with light output known at the 4% level. The plans to include such a source of Čerenkov radiation in the calibration of the SNO detector rely on making several slight modifications to the basic design reported here. The safety of the source, and in particular its structural integrity, have to be assessed more fully. If the source is to be used in the light water region between the photomultiplier support structure and the acrylic vessel, then the source should be constructed from silica instead of glass. This is necessary as the transmission of the acrylic no longer dominates the spectral intensity visible to the photomultipliers.

In Chapter 5 the use of the Mark 3 Čerenkov source to calibrate photomultipliers was demonstrated. Systematic measurements of the absolute efficiency of counting single photons as a function of the operating condition was demonstrated for several photomultipliers. The results were found to be in broad agreement with those reported by other authors. The distance between the photomultipliers and source is far greater in SNO than in the Mortar, and consequently an order of magnitude more ^{90}Sr activity will be needed if the same signal to noise ratio is to be used. Other properties of the SNO photomultipliers were measured in Chapters 6 and 7 and the photomultipliers were demonstrated to be suitable for use in the SNO detector.

In this chapter the suitability of an alpha decay isotope in liquid scintillator for a routine calibration source has been demonstrated. Independent work by Leslie *et al.* at Queen's University has yielded similar results using broadly similar but not identical methods and chemicals. Further work is need to demonstrate that the stability and safety criteria of a SNO calibration source can be met.

Appendix A

The MSW effect

Here the effective mixing angle and resonant condition for neutrino flavor oscillations are computed for neutrinos propagating through a medium of constant electron number density. Suppose that the weak eigenstates for two neutrino flavors ν_e and ν_μ can be transformed into the vacuum eigenstates by a unitary transformation of the type

$$\begin{bmatrix} \phi_e \\ \phi_\mu \end{bmatrix} = \begin{bmatrix} \cos\theta_v & \sin\theta_v \\ -\sin\theta_v & \cos\theta_v \end{bmatrix} \begin{bmatrix} \phi_1 \\ \phi_2 \end{bmatrix} = R[\theta_v] \begin{bmatrix} \phi_1 \\ \phi_2 \end{bmatrix}, \tag{A.1}$$

where $R[\theta_v]$ is the unitary matrix[1] for a rotation of angle θ_v. In the vacuum, the mass eigenstates obey the Schrödinger wave equation with a diagonal Hamiltonian

$$i\frac{\partial}{\partial t}\begin{bmatrix} \phi_1 \\ \phi_2 \end{bmatrix} = \begin{bmatrix} E_1 & 0 \\ 0 & E_2 \end{bmatrix} \begin{bmatrix} \phi_1 \\ \phi_2 \end{bmatrix} = H_v \begin{bmatrix} \phi_1 \\ \phi_2 \end{bmatrix}. \tag{A.2}$$

Now in a medium containing matter there is an extra interaction Hamiltonian which is generally non-trivial. However if only the difference in the phase velocity of the neutrinos is required it is sufficient to consider only the interactions which are different for the two neutrino flavors. As discussed in Chapter 1 there is a charged current scattering channel only available to electron neutrinos which has amplitude $\sqrt{2}GN_e$ where G is the Fermi coupling constant and N_e is the number density of electrons in the medium. For constant electron number density, this interaction has a Hamiltonian

$$H_i = \begin{bmatrix} \sqrt{2}GN_e & 0 \\ 0 & 0 \end{bmatrix}, \tag{A.3}$$

when expressed in the flavor basis. Note that this interaction Hamiltonian cannot be simply added to that in Equation (A.2), the wave equation must be transformed to the flavor basis

[1] $R[\theta_v]$ is a member of the Abelian group $\Re_2$ with an inverse $R[\theta_v]^{-1} = R^\dagger[\theta_v] = R[-\theta_v]$.

first. Then the wave equation becomes

$$i\frac{\partial}{\partial t}\begin{bmatrix}\phi_e\\ \phi_\mu\end{bmatrix} = R[\theta_v]\,H_v\,R^\dagger[\theta_v]\begin{bmatrix}\phi_e\\ \phi_\mu\end{bmatrix} + H_i\begin{bmatrix}\phi_e\\ \phi_\mu\end{bmatrix}, \tag{A.4}$$

where $R^\dagger[\theta_v]$ is the Hermitian conjugate (and inverse) of $R[\theta_v]$. Note that the addition of the interaction Hamiltonian has now made the wave equation non-diagonal in both the flavor (ϕ_e, ϕ_μ) and vacuum (ϕ_1, ϕ_2) representations. There exists another representation in which the total Hamiltonian in Equation (A.4) becomes diagonal; these states (with wavefunctions ϕ_{1m}, ϕ_{2m}) are known as the matter eigenstates. By analogy with the vacuum eigenstates, they are related to the weak eigenstates by a unitary transformation with angle θ_m:

$$\begin{bmatrix}\phi_e\\ \phi_\mu\end{bmatrix} = \begin{bmatrix}\cos\theta_m & \sin\theta_m\\ -\sin\theta_m & \cos\theta_m\end{bmatrix}\begin{bmatrix}\phi_{1m}\\ \phi_{2m}\end{bmatrix} = R[\theta_m]\begin{bmatrix}\phi_{1m}\\ \phi_{2m}\end{bmatrix}. \tag{A.5}$$

Transformed to the basis of matter eigenstates the total Hamiltonian[2] becomes

$$H_m = R^\dagger[\theta_m]\left(R[\theta_v]\,H_v\,R^\dagger[\theta_v] + H_i\right)R[\theta_m]\,. \tag{A.6}$$

The multiplicative property of the elements of $\Re_2$ (rotation matrices), $R[x]\,R[y] = R[x+y]$, is then used to simplify H_m. The matter mixing angle θ_m is defined by demanding that H_m is diagonal, and so the non-diagonal component must vanish:

$$\sqrt{2}GN_e\sin\theta_m\cos\theta_m - (E_2 - E_1)\sin(\theta_m - \theta_v)\cos(\theta_m - \theta_v) = 0\,. \tag{A.7}$$

After rearranging, squaring both sides, and using compound angle formulae, Equation (A.7) simplifies to

$$\sin^2 2\theta_m = \frac{\sin^2 2\theta_v}{\sin^2 2\theta_v + (l_v/l_m - \cos 2\theta_v)^2}\,, \tag{A.8}$$

where $l_v = 2\pi\hbar c/(E_2 - E_1)$ is the vacuum mixing length and $l_m(N_e) = 2\pi\hbar c/\sqrt{2}GN_e$ is the neutrino-electron interaction length for a certain electron density. The MSW resonance occurs when $\sin^2 2\theta_m = 1$ and hence $l_v/l_m = \cos 2\theta_v$ gives the condition for resonant electron density

$$N_e = \frac{\Delta m^2\cos 2\theta_v}{2\sqrt{2}GE}\,, \tag{A.9}$$

where the approximation $E_2 - E_1 \simeq \Delta m^2/2E$ has been used for neutrinos in the relativistic limit. The quantity $\Delta m^2 = m_2^2 - m_1^2$ must be positive for this condition to be established.

[2]Note that any number of arbitrary (unitary) transformations of the basis states always leave the Hamiltonian as Hermitian. More explicitly, if $H' = R[\theta_v]\,H\,R^\dagger[\theta_v]$ and if $H^\dagger = H$ then $(H')^\dagger = H'$ holds also.

Appendix B

The Čerenkov effect - A dynamical view

The threshold criterion for, and the yield of photons from, Čerenkov radiation are usually derived on classical lines. However, following the suggestion of Cox [109], these may also be derived by assuming only that the energy-momentum relationship for a free photon is altered in the presence of a polarizable medium. The wavelength of a photon of angular frequency ω in a medium of refractive index n is $2\pi c/n\omega$ where c is the speed of light in vacuum. Hence the 'pseudo-momentum' of the photon is defined as $n\hbar\omega/c$, a factor of n larger than the result for a photon in a vacuum. This pseudo-momentum is conserved in interactions which produce a Čerenkov photon. Using this assumption as a basis for Čerenkov radiation, the threshold and photon yield are derived below.

B.1 The Čerenkov threshold

The process of Čerenkov radiation will be assumed to be $e^- \rightarrow e^- + \gamma$ in the presence of a polarizable medium which increases the momentum of the photon as discussed above. This process is forbidden in free space because energy and momentum cannot both be conserved for the emission of any real photon. However the increase in the photon momentum for a given frequency removes this restriction, see Jelley [2] and references therein.

Consider an electron of total initial energy E which emits a Čerenkov photon of energy $\hbar\omega$ at an angle θ to the initial direction. The final state electron has total energy E' as shown in Figure B.1. The four-momenta can then be defined:

$$p^\mu = (\mathbf{p}, E/c) \qquad p'^\mu = (\mathbf{p}', E'/c) \qquad k^\mu = (\hbar\mathbf{k}, \hbar\omega/c)\,, \tag{B.1}$$

where $\mathbf{k}$ is the wavevector of the Čerenkov photon. Conservation of energy and momentum is then expressed as $p^\mu - k^\mu = p'^\mu$. The scalar product of this relation with its covariant

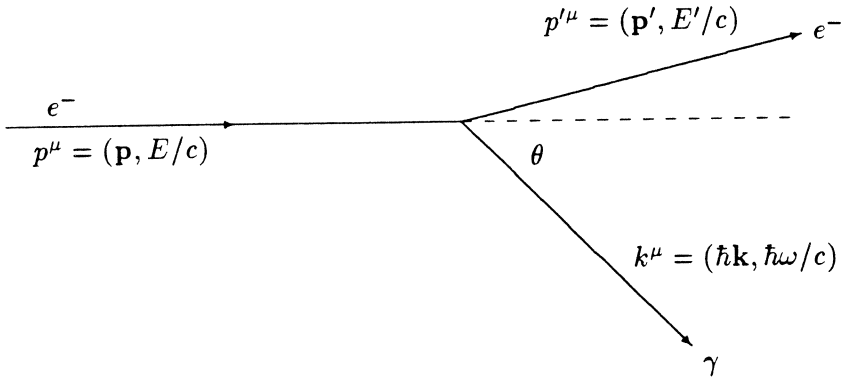

Figure B.1: The kinematics of Čerenkov radiation.

equivalent yields

$$-m^2c^2 - 2\left(\hbar kp\cos\theta - \frac{\hbar\omega E}{c^2}\right) + (n^2-1)\left(\frac{\hbar\omega}{c}\right)^2 = -m^2c^2\,, \tag{B.2}$$

where scalar product $k_\mu k^\mu$ has been expressed in terms of ω using the relation $k = n\omega/c$. Defining $\beta = pc/E$, the angle of emission of a Čerenkov photon with respect to the direction of the initial electron is then found to be

$$\cos\theta_C = \frac{1}{n\beta}\left[1 + \frac{n^2-1}{2}\left(\frac{\hbar\omega}{E}\right)\right]. \tag{B.3}$$

The result of Equation (B.3) is the fully relativistic condition for the emission of a Čerenkov photon and is correct to all orders in $(\hbar\omega/E)$. In the optical regime where $(\hbar\omega/E) \to 0$ this condition reduces to the classical approximation $\cos\theta = 1/n\beta$. Equation (B.3) is in agreement with the corresponding result in Jelley [2] although he expresses the result in terms of the de Broglie wavelength of the initial electron.

B.2 The Čerenkov yield

The Feynman rules in Quantum Electrodynamics (QED) can be used to calculate the number and spectrum of Čerenkov photons produced from an electron per unit track length from the process $e^- \to e^- + \gamma$. An outline of the calculation of the rate is made using first order perturbation theory. The notation and conventions of Aitchison and Hey [110] are used, along with natural units $\hbar = c = 1$ where the meaning is clear.

The equivalent 'decay rate' for the process $e^- \to e^- + \gamma$ represents the number of Čerenkov photons produced per unit time *in the rest frame of the electron* and is denoted Γ. To convert to the laboratory frame the rate is divided by $\gamma(E)$ the relativistic dilation factor. Finally

the most convenient form is the number of photons per unit track length, and so the result is further divided by the velocity βc, and hence

$$\frac{dN}{dx} = \frac{\Gamma}{\gamma\beta c} . \tag{B.4}$$

The rate is given by

$$d\Gamma = \frac{1}{2m} |A|^2 \, d\text{Lips} , \tag{B.5}$$

where m is the electron mass and A is the matrix element for the process. Lips is an abbreviation for the Lorentz Invariant Phase Space, similar to the density of final states. An outline evaluation of these factors is now performed for Čerenkov radiation.

B.2.1 Phase space

The Lips for the lowest order decay process $e^- \rightarrow e^- + \gamma$ is

$$d\text{Lips} \sim \delta^4(p - p' - k) \frac{d^3\mathbf{p}'}{E'} \frac{d^3\mathbf{k}}{\omega} , \tag{B.6}$$

where some constant factors are omitted for simplicity, see Appendix E of Aitchison and Hey [110]. Integration over the three variables $d^3\mathbf{p}'$ ensures that momentum is conserved as the delta function vanishes except when $\mathbf{p} = \mathbf{p}' + \mathbf{k}$. Writing $d^3\mathbf{k}/\omega$ as $n^3 \, \omega \, d\omega \, d\Omega$, where $d\Omega$ is the element of solid angle, the Lips can be expressed as

$$d\text{Lips} \sim \delta(E - E' - \hbar\omega) \frac{n^3 \, \omega \, d\omega \, d\Omega}{E'} . \tag{B.7}$$

In the optical regime where $(\hbar\omega/E) \rightarrow 0$ we can write $E - E' \approx \hbar\omega \, \beta n \cos\theta$ (from conservation of momentum in the direction $\mathbf{p}$), and $E' \rightarrow E$ so that

$$d\text{Lips} \sim \delta(\hbar\omega \, \beta n \cos\theta - \hbar\omega) \frac{n^3 \, \omega \, d\omega \, d\cos\theta}{E} , \tag{B.8}$$

where the azimuthal integration has been performed and so $d\Omega = 2\pi d\cos\theta$. Now $\delta(f(x)) = \delta(x - x_0)/|f'(x_0)|$ if $f(x_0)$ is the only zero of f. Hence

$$d\text{Lips} \sim \frac{n^2 \, d\omega}{p} \delta(\cos\theta - \cos\theta_C) \, d\cos\theta , \tag{B.9}$$

where $p = \beta E$ and $\cos\theta_C$ is defined in Equation (B.3).

B.2.2 Matrix element

Using the standard rules for the computation of Feynman graphs the matrix element for the process $e^- \rightarrow e^- + \gamma$ takes the form

$$A \sim \bar{u}(p', s') \, (ie\gamma^\mu) \, u(p, s) \, \epsilon_\mu(\lambda) , \tag{B.10}$$

where the $\bar{u}$ and u are Dirac spinors for the electron in the final and initial states respectively, and $\epsilon_\mu(\lambda)$ is a four-vector representing the polarization of the Čerenkov photon (and in general is a function of the helicity state λ). Again, several constant factors have been ignored in Equation (B.10) for simplicity. There is however a subtle point that Equation (B.10) overestimates the matrix element by a factor n in the presence of a polarizable medium. This is due to the fact that the Feynman rules are devised for a photon in vacuum. The $1/n$ factor is included in the computation of Tidman [64] who uses a direct field theory approach and not the Feynman rules. Tidman points out this factor of $1/n$ but does attempt to justify it.

The matrix element can be viewed as just a contraction of the polarization vector ϵ_μ with the electromagnetic transition current $j^\mu = \bar{u}\gamma^\mu u$. This will produce a factor of $\sin\theta$ in the matrix element. To demonstrate this explicitly it is convenient to use the Gordon decomposition of j^μ in the form:

$$j^\mu = \bar{u}(p')\gamma^\mu u(p) = \bar{u}(p')\left[\frac{(p+p')^\mu}{2m} + \frac{i\sigma^{\mu\nu}(p'-p)_\nu}{2m}\right]u(p)\,, \tag{B.11}$$

where the tensor $\sigma^{\mu\nu}$ is defined as the commutation of two γ matrices in the usual way; for details see Bjorken and Drell [111]. This is particularly convenient for Čerenkov radiation in the optical limit as $p' \to p$ and so only the first term in the square bracket is non-vanishing and with the spinor normalisation chosen so that $\bar{u}u = 2m$, we have

$$|A| = \frac{ep\cos\phi}{n}\,, \tag{B.12}$$

where $\cos\phi$ is the projection of the polarization on to the momentum vector. Note that a suitable photon gauge has been chosen so that the fourth (timelike) component of ϵ_μ vanishes, so that $p^\mu\epsilon_\mu = \mathbf{p}\cdot\epsilon$. A sum over the photon spin states has to be performed and this is most easily done if the polarization vector is resolved into two components normal to $\mathbf{k}$; one in the plane containing $\mathbf{p}$ and $\mathbf{p}'$ and the other normal to this plane. The latter will have a vanishing scalar product with $\mathbf{p}$ and the former will be the sine of the Čerenkov angle, so that $\cos\phi \to \sin\theta_C$. Hence

$$|A|^2 = \frac{\alpha p^2 \sin^2\theta_C}{n^2}\,. \tag{B.13}$$

B.2.3 Yield of photons in the laboratory frame

By integrating Equation (B.5) with respect to $d\cos\theta$ and using the result in Equation (B.4) the number of photons emitted per unit track length in the laboratory frame is then

$$\frac{d^2N}{dx} = \frac{1}{\gamma\beta c}\frac{1}{2m}\left(\frac{\alpha p^2\sin^2\theta_C}{n^2}\right)\frac{n^2 d\omega}{p}\,. \tag{B.14}$$

Using $p = \gamma\beta m$ (natural units) the final result is

$$\frac{d^2N}{dx\,d\omega} = \frac{\alpha}{c}\sin^2\theta_C = \frac{\alpha}{c}\left(1 - \frac{1}{\beta^2 n^2}\right)\,, \tag{B.15}$$

which is in agreement with the classical result.

Appendix C

Unique first-forbidden beta spectra

From the requirements of Lorentz covariance it can be shown[1] that there are only five bilinear operators that might represent the beta decay interaction:

$$\bar{\psi}\psi\,, \qquad \bar{\psi}\gamma_\mu\psi\,, \qquad i\bar{\psi}\gamma_\mu\gamma_\nu\psi\,, \qquad i\bar{\psi}\gamma_5\gamma_\mu\psi\,, \qquad \bar{\psi}\gamma_5\psi\,, \tag{C.1}$$

where γ_μ are the Dirac matrices, $\gamma_5 = \gamma_1\gamma_2\gamma_3\gamma_4$, and $\bar{\psi} \equiv \psi^\dagger\gamma_4$. These operators are classed in terms of their transformation properties as scalar, 4-vector, tensor, axial 4-vector and pseudoscalar respectively. The matrix element for the beta decay interaction can then be cast in the general form[2]

$$M \;=\; G\sum_\mu \int B_\mu(\mathbf{r})\, L_\mu(\mathbf{r})\, d\tau \;=\; G\sum_\mu \int (\bar{\psi}_p\, \hat{O}\, \psi_n)\,[\bar{\psi}_e\, \hat{O}(C_l + \gamma_5 C_l')\, \psi_{\bar{\nu}}]\, d\tau\,, \tag{C.2}$$

where C_l and C_l' are constants, and the expressions in the parentheses and square brackets represent the baryon and lepton currents respectively. The operator $\hat{O}$ represents the beta-decay interaction with a strength[3] proportional to G. For simplicity, the Hermitian conjugate term is omitted from equation (C.2), and in the case of a nuclear beta decay there is an implied sum over the nucleons present.

The steps to find the specific form of the matrix element are recounted in many textbooks[4], so only the salient points are summarized here. The experimental observation that the neutrino (antineutrino) is found to have negative (positive) helicity, constrains the constants C_l and C_l' to be equal. In addition, beta decay electrons are found to have helicity $-v/c$, and this restricts the interaction operators to have the transformation properties of a vector or axial-vector. Hence the operator $\hat{O}$ must be equal to γ_μ. The currents of equation (C.2) can now be expressed as

$$B_\mu(\mathbf{r}) \;=\; \bar{\psi}_p\, \gamma_\mu(C_V - \gamma_5 C_A)\, \psi_n, \qquad \text{and} \qquad L_\mu(\mathbf{r}) \;=\; \bar{\psi}_e\, \gamma_\mu(1+\gamma_5)\, \psi_{\bar{\nu}}\,, \tag{C.3}$$

[1] See Bjorken and Drell [111].

[2] Following the notation of Weidenmüller [77].

[3] For simplicity, the cosine of the Cabibbo angle is included in the constant G. This represents the reduction of the coupling of the W boson to the u and d quarks in comparison to electrons and antineutrinos, see Cabibbo [112].

[4] See Perkins [113] appendix D.6.

where C_V and C_A are constants specifying the strength of the vector and axial-vector couplings.

For a unique first-forbidden beta decay, the vector current term gives no contribution to the baryon current $B_\mu(\mathbf{r})$ of equation (C.3) to first order in $\mathbf{k}\cdot\mathbf{r}$. There are vector current terms of higher order in the expansion of $e^{i\mathbf{k}\cdot\mathbf{r}}$, but these are usually neglected as $\mathbf{k}\cdot\mathbf{r}$ is small. In this case, the only non-vanishing term of the baryon current is an axial-vector term $C_A \int B_{ij}$, see Weidenmüller [77], where B_{ij} is a traceless symmetric second rank tensor defined by

$$B_{ij} = \sigma_i x_j + x_j \sigma_i - \frac{2}{3}\delta_{ij}(\sigma\cdot\mathbf{r}) . \tag{C.4}$$

This conclusion is critical for the computation of the effects of the Coulomb field on unique beta spectra, as the spin-orbit coupling cannot cause an interference between states of different total angular momentum. Hence the orbital angular momentum is a good quantum number for electrons with $j = l + 1/2$, and in the case of a unique first forbidden decay there is zero probability of having both leptons in $s_{1/2}$ states. Note that in non-unique decays, where the leptons can be emitted in states with $\mathbf{l}$ and $\mathbf{s}$ antiparallel, the emitted electron is not in a definite state of orbital angular momentum. This leads to a non-vanishing amplitude for decay with both leptons in $l = 0$ states, and when the *Quasi-allowed* approximation[5] is satisfied, this coupling can radically alter the beta spectrum to that of an allowed shape. However, since this amplitude vanishes for unique decays, the effects of Coulomb interactions reduce to a simple multiplicative factor. The only additional shape correction arises from the extra momentum dependence of the matrix element.

Setting aside the Coulomb interactions, the energy spectrum of beta decay electrons is altered from the allowed shape only by a factor which occurs because the $l = 0$ term is replaced by the $l = 1$ term of the partial-wave expansion of the lepton wavefunction

$$\phi(\mathbf{r}) \sim e^{i(\mathbf{k}_e+\mathbf{k}_\nu)\cdot\mathbf{r}} = \sum_{l=0}^{\infty} \frac{[i(\mathbf{k}_e+\mathbf{k}_{\bar\nu})\cdot\mathbf{r}]^l}{l!} , \tag{C.5}$$

where $\hbar\mathbf{k}_e$ and $\hbar\mathbf{k}_{\bar\nu}$ are the momenta of the electron and antineutrino respectively. This introduces an additional factor $\mid i(\mathbf{k}_e + \mathbf{k}_{\bar\nu})\cdot\mathbf{r} \mid^2$ into the matrix element. When the spatial integration and averaging over angle between electron and neutrino is performed, the only factor remaining is proportional to

$$k_e^2 + k_{\bar\nu}^2 \sim (\epsilon^2 - 1) + (\epsilon_0 - \epsilon)^2 , \tag{C.6}$$

where ϵ is the total electron energy in units of its rest mass, and ϵ_0 is the end-point value of ϵ.

[5] See Weidenmüller [77] or Wu and Moszkowski [80].

Appendix D

The photoelectric effect

The photoelectric effect is the process whereby a photon liberates an electron from a solid by exciting the electron into a continuum state. In a simple theory of photoelectron emission, the unbound electron leaves the bulk material, provided it has enough kinetic energy to overcome the electrostatic polarization barrier known as the 'work function' ϕ. This leads to the Einstein condition $E \leq \hbar\omega - \phi$ for the emission of a photoelectron of kinetic energy E from a photon of angular frequency ω. The probability and cross-section of this process can, in principle, be calculated from perturbation theory, provided the wavefunctions of the electrons in the solid are known. However, photocathodes often have complex band structures, and the wavefunctions of the electron states are generally unknown. In particular, the Independent Electron Approximation, see Landau [114], is probably invalid[1] in this context. However the photoelectric properties of photocathode-type surfaces have been subject to experimental investigations which are summarised here, see also Weissler [116].

Hintergger [117] measured the kinetic energies of photoelectrons from 10 eV photons, and demonstrated that a negligible number of photoelectrons originate from levels near the Fermi surface in metals. He was also able to demonstrate that a sharp increase of the cross-section for photon-electron interactions in a metal occurs at much deeper levels than thermal emission and field emission. Furthermore, the number of electrons emitted per incident photon rises steeply as the quantum energy increases beyond a value E_{cut}, which is appreciably higher than the work function ϕ. With further increase of photon energy, the yield reaches a flat maximum followed by a slow decrease. These yields for $\hbar\omega > E_{\text{cut}}$ are several orders of magnitude greater than those at longer wavelengths. The energy distribution curves for photoelectrons are cut off at $E = \hbar\omega - E_{\text{cut}}$ and not at the higher maximum $E = \hbar\omega - \phi$ related to the common surface polarization effects. Temperature effects were shown to be small.

Similar results were obtained by Walker and Weissler [118], who looked at electron en-

[1] As Ashcroft and Mermin [115] point out, any property involving electronic levels far from the Fermi surface (such as soft X-ray emission, optical absorbtion as well as photoelectric emission) may be substantially affected by electron-electron interactions.

ergy distributions from Au and Ge photocathodes illuminated with ultra-violet photons with wavelengths of 100 nm. They suggest that photoelectrons released in the bulk of the material undergo multiple electron scattering, and emerge with significantly reduced energies. Their results also suggest that the electrostatic barrier theory fails at higher photon energies.

In practical photocathodes, bialkalis are used as they have much higher photoelectric cross-sections than metals. Indeed the photoelectric cross-section of caesium antimonide Cs_3Sb is typically 1000 times that of potassium. These bialkalis, being semiconductors, are expected to have complex level schemes with band structures. Although this will make detailed calculation of photoelectric transitions rates intractable, experiments indicate that we have some qualitative understanding of photocathodes. Burton [119] has studied both the optical and absorption coefficients and the quantum yields from a surface of caesium antimonide. His results show a steep rise in both the absorption and quantum yield at about 2 eV. He attributes this to an energy band structure with a forbidden region of about 2 eV width between the filled valence band and the empty conduction band. Evidence such as this suggests that negatively biasing photocathodes with voltages large compared to the band-gap energy scale is sufficient to ensure that all photoelectrons are liberated.

Bibliography

[1] J. N. Bahcall, (1989) *Neutrino Astrophysics*, Cambridge University Press. Several of the following references were obtained from this source.

[2] J. V. Jelley, (1958) *Čerenkov radiation*, Pergamon Press, London.

[3] H. A. Bethe, *Phys. Rev.*, **55** 434 (1939).

[4] J. N. Bachall, W. A. Fowler, I. Iben and R. L. Sears, *Ap. J.*, **137** 334 (1963). One of the first of the modern stellar evolution codes in which neutrino fluxes are calculated. See also R. L. Sears, *Ap. J.*, **140** 477 (1964).

[5] J. N. Bachall and R. K. Ulrich, *Rev. Mod. Phys.*, **60** 297 (1988).

[6] J. Christensen-Dalsgaard, D. Gough and J. Toomre, *Science*, **229** 923 (1985).

[7] D. Gough, *Physics World*, **5**, No 7, 21 (1992).

[8] The Debye-Hückel theory calculates the polarisation of gas molecules from (Coulomb-type) interactions with charged particles. For an account of the equation of state for a stellar plasma see M. Schwarzschild, (1958) *Structure and Evolution of the stars*, Princeton University Press.

[9] M. Schwarzschild and R. Härm, *Ap. J.*, **184** 5 (1973) and also M. N. Rosenbluth and J. N. Bahcall, *Ap. J.*, **184** 9 (1973).

[10] P. A. Sturrock (Editor), (1986) *Physics of the Sun - Volume I: The Solar Interior*, D. Reidel Publishing company. See references therein, particularly in Chapter 3 to W.F. Huebner *et al.*, (1977) *Astrophysical Opacity Library*, Los Alamos report LA-6760-M, and in Chapter 2 the nuclear reaction cross-sections.

[11] J. N. Bahcall, W. F. Huebner, N. H. Magee, A. L. Merts and R. K. Ulrich, *Ap. J.*, **184** 1 (1973).

[12] W. A. Dziembowski, A. A. Pamyatnykh and R. Sienkiewicz, *Mon. Not. R. Astr. Soc.*, **244** 542 (1990).

[13] N. Grevesse, *Physica Scripta*, **T8** 49 (1984).

[14] L. H. Aller, (1986) *Spectroscopy of Astrophysical Plasmas*, 33, Cambridge University Press.

[15] A. N. Cox *et al.*, *Ap. J.* **353** 698 (1990).

[16] Sackman *et al.*, *Ap. J.* **360** 727 (1990).

[17] J. N. Bachall *et al.*, *Rev. Mod. Phys.*, **54** 767 (1982).

[18] S. Turck-Chièze, S. Cahen, M. Cassé and C. Doom, *Ap. J.*, **335** 415 (1988).

[19] S. Cahen, C. Doom and M. Cassé, in *'86 Massive Neutrinos in Astophysics and Particle Physics, Proceedings of the Sixth Moriond Workshop,* edited by O. Fackler and J. Tran Thanh Van, 83 (1986).

[20] J. C. Wheeler and A. G. W. Cameron, *Ap. J.*, **170** 157 (1975).

[21] S. M. Chitre, D. Ezer and R. Stothers, *Ap. Lett.*, **14** 37 (1973).

[22] Z. Abraham and I. Iben, *Ap. J.*, **170** 157 (1971).

[23] Wolfendale *et al.*, *Nature*, **238** 130 (1972). R. Davis *et al.*, *Proc. Neutrino '72 conf., Baltonfüred, Hungary* (1972). E. L. Fireman, B. T. Cleveland, R. Davis and J. K. Rowley, (1984) *Solar neutrinos and Neutrino Astronomy, Proceedings of the Homestake Conference*, AIP.

[24] J. N. Bahcall, *Phys. Rev.*, **B135** 137 (1964).

[25] P. D. Parker and A. J. Howard, *Nuc. Phys.*, **A250** 309 (1975).

[26] J. N. Bahcall and M. H. Pinsonneault, *Ap. J.*, (1992) to appear. Details used in this thesis are quoted from the paper presented at the Neutrino '92 conference.

[27] Y. Lebreton and A. Maeder, *Astr. Ap.*, **161** 119 (1986).

[28] D. A. Vandenberg, *Ap. J. Suppl.*, **51** 29 (1983).

[29] Hirata *et al.*, (The Kamiokande collaboration), *Phys. Rev.*, D44 2241 (1991).

[30] A. Suzuki, *Kamiokande Solar Neutrino Experiment and Solar Neutrino Problem*, KEK preprint 91-187 (1991). For an details of the Kamiokande II solar neutrino search see Soo Bong Kim, PhD Thesis, University of Pennsylvania, report UPR-0174E (1989).

[31] The Sage collaboration, *Nucl. Phys.*, (Proc. Suppl.) **B19** 84 (1991). Also *Phys. Rev. Lett.*, **67** 3332 (1991).

[32] L. Paoluzi, *Nucl. Inst. and Meth.*, **A279** 133 (1989).

[33] Talk given by T. Kirsten (for the Gallex collaboration) at Neutrino 92, to appear in *Nucl. Phys.*, B.

[34] Gavrin *et al.*, (the SAGE collaboration), at the XXVI International Conference on High Energy Physics (ICHEP), August 6-12, 1992 in Dallas, Texas.

[35] J. D. Jackson, (1975) *Classical Electrodynamics*, Second edition, Wiley, New York.

[36] L. Wolfentein, *Phys. Rev.*, **D17** 2369 (1978).

[37] S. P. Mikheyev and A. Yu. Smirnov, *Sov. J. Nucl. Phys.*, **42** 913 (1986), and also in *Nuovo Cimento,* **C9** 17 (1986).

[38] Neutrino mass generation and the see-saw mechanism are considered by S. A. Bludman, D. C. Kennedy and P. G. Langacker, *Phys. Rev.*, **D45**, No 5, 1810 (1992). See also R. Gandhi, *Phys. Rev.*, **D45**, No 7, R2192 (1992).

[39] J. N. Bahcall and W. H. Press, *Ap. J.*, **370** 730 (1991).

[40] M. Kobayashi *et al.*, *Phys. Rev. Lett.*, **67** 1685 (1991).

[41] G. Ranucci *et al.*, (The Borex collaboration), *Nucl. Inst. Meth.,* **A315** 229 (1992). See also the Borexino *Proposal for a real time detector of low energy solar neutrinos.*

[42] A. Bettini *et al.* (The ICARUS collaboration), *Nucl. Inst. Meth.*, **A315** 223 (1992). See also the ICARUS proposal, LNF report LNF-89/005 (R).

[43] The SNO collaboration, (1987) *The Sudbury Neutrino Observatory Proposal*, SNO reference number SNO-87-12.

[44] J. N. Bahcall, *Phys. Lett.*, **13** 332 (1964).

[45] N. Tatara, Y. Kohyama and K. Kubodera, *Phys. Rev.*, **C42** 1694 (1990).

[46] M. Doi and K. Kubodera, *Phys. Rev.*, **C45** 1988 (1992).

[47] S. Yang, W. C. Haxton and E. M. Henley, *Phys. Rev.*, **C45** 1982 (1992).

[48] G. t' Hooft, *Phys. Lett.*, **37B** 195 (1971). The paper by t' Hooft contains a possible typographic error at the end of the equation labelled (5). Subject to checking the final bracket should read $(g_A^2 - g_V^2)$ and not $(g_A - g_V^2)$.

[49] S. Weinberg, *Phys. Rev. Lett.*, **19** 1264 (1967).

[50] J. N. Bahcall, K. Kubodera and S. Nozawa, *Phys. Rev.*, **D38** 1030 (1988).

[51] For a review for supernova neutrinos (with extensive references) see A. Burrows, *Ann. Rev. Nucl. Part. Sci.*, **40** 181 (1990).

[52] A. Burrows, D. Klein, and R. Gandhi, *Phys. Rev.* **D45** 3361 (1992).

[53] M. E. Moorhead, D. Phil thesis, Department of Physics, Oxford University, (1992).

[54] W. T. Welford and R. Winston, (1989) *High Collection Non-imaging Optics,* Academic Press.

[55] The SNO collaboration, (1987) *Collection of Annexes in support of the main proposal* SNO-87-12.

[56] P. Thornewell, private communications. For details see R. G. H. Robertson *et al.*, *Neutral Current Detection in the Sudbury Neutrino Observatory*, (revised) appendix to the Los Alamos funding request FIN-94-ER-E324 (1992).

[57] J. C. Zwinkels, W. F. Davidson and C. X. Dodd, *Appl. Opt.*, **29** 3240 (1990).

[58] P. Skensved and B. C. Robertson, SNO reports SNO-STR-90-27 and SNO-STR-90-28, (1990); also SNO-STR-91-06 and SNO-STR-91-07, (1991).

[59] W. R. Nelson, H. Hirayama and D. W. O. Rogers, *The EGS4 code system*, SLAC report 265 (1985).

[60] P. A. Čerenkov, *Dokl. Akad. Nauk, SSSR*, **2** 451 (1934).

[61] I. M. Frank and I. E. Tamm, *Dokl. Akad. Nauk, SSSR*, **14** 109 (1937). See also I. E. Tamm, *Journal of Physics USSR*, **1** 439 (1939), and I. E. Tamm, in *Les Prix Nobel 1958*, Stockholm, pp 122-133 (1959). English translations of the Russian articles can be found in I. E. Tamm, (1991) *I. E. Tamm, Selected papers*, edited by B. M. Bolotovshii and V. Ya. Frenkel, consultant editor R. Peierls, Springer-Verlag, Berlin.

[62] R. T. Cox, *Phys. Rev.*, **66** 106 (1944).

[63] G. Beck, *Phys. Rev.*, **74** 795 (1948).

[64] D. A. Tidman, *Nucl. Phys.*, **2** 289 (1956).

[65] B. D. Nag and A. M. Sayied, *Proc. Roy. Soc.*, **A235** 544 (1956).

[66] G. Czapski and D. Katakis, *J. Phys. Chem.*, **70** 637 (1966).

[67] ICRU, International Commission on Radiation Units and Measurements, *Stopping Powers for Electrons and Positrons*, ICRU Report 37 (1984).

[68] D. W. O. Rogers, *Nucl. Inst. and Meth.*, **227** 535 (1984).

[69] T. M. Jenkins, W. R. Nelson and A. Rindi, (1988) *Monte Carlo Transport of Electrons and Photons*, Plenum Press, New York.

[70] M. D. Lay, D. L. Wark and R. J. Boardman, *Producing Čerenkov Photons from Low Energy Electrons with EGS4*, SNO report SNO-STR-91-047 (1991).

[71] G. Elwert, *Ann Physik*, **34** 178 (1939).

[72] H. W. Koch and J. W Motz, *Rev. Mod. Phys.*, **31** 920 (1959).

[73] P. E. Gill and G. F. Miller, *Comp. J.*, **15** 80 (1972).

[74] W. Paul and H. Reich, *Z. Phys.*, **127** 429 (1950).

[75] W. Anderson and E. H. Belcher, *Brit. J. Appl. Phys.*, **5** 53 (1954).

[76] G. W. C. Kaye and T. H. Laby, (1989) *Tables of Physical and Chemical Constants*, fifteenth edition, Longman group.

[77] H. A. Weidenmüller, *Rev. Mod. Phys.*, **33** 574 (1961).

[78] M. E. Rose, *Phys. Rev.*, **49** 727 (1936).

[79] L . Durand, *Phys. Rev.*, B**135** 310 (1964).

[80] C. S. Wu and S. A. Moszkowski, (1966) *Beta Decay*, Interscience Publishers, John Wiley & Sons.

[81] H. F. Schopper, (1966) *Weak Interactions and Nuclear Beta Decay*, North-Holland Publishing Company, Amsterdam.

[82] M. S. Freedman, *Ann. Rev. Nucl. Sci.*, **24** 209 (1974).

[83] R. J. Boardman, M. D. Lay, N. W. Tanner and D. L. Wark, *Calibration Sources of Čerenkov Radiation*, SNO report SNO-STR-91-033 (1991).

[84] M. R. Adams *et al.*, *Nucl. Inst. Meth.*, A**238** 333 (1985).

[85] A. H. Sommer, (1980) *Photoemissive Materials*, Robert E. Krieger Publishing Company, Huntington, New York.

[86] M. E. Moorhead and N. W. Tanner, *Optical Properties of the K-Cs Bialkali Photocathode*, Oxford University Nuclear Physics preprint OUNP-91-05 (1991).

[87] R. S. Lakes and S. K. Poultney, *Appl. Opt.*, Vol. **10**, No 4, 797 (1971).

[88] A. T. Young and R. E. Schild, *Appl. Opt.*, Vol. **10**, No 7, 1668 (1971).

[89] L. Birenbaum and D. B. Scarl, *Appl. Opt.*, Vol. **12**, No 3, 519 (1973).

[90] M. Calicchio *et al.*, (The MACRO collaboration), *Nucl. Inst. and Meth.*, **A264** 18 (1988).

[91] R. Foord, R. Jones, C. J. Oliver and E. R. Pike, *Appl. Opt.*, Vol. **8**, No 10, 1975 (1969).

[92] A. T. Young, *Appl. Opt.*, Vol. **10**, No 7, 1681 (1971).

[93] R. Jones, C. J. Oliver and E. R. Pike, *Appl. Opt.*, Vol. **10**, No 7, 1673 (1971).

[94] G. A. Morton, H. M. Smith and R. Wasserman, *IEEE Trans. Nucl. Sci.*, NS-**14**, No 1, 443 (1967).

[95] W. C. Paske, *Rev. Sci. Instr.*, **45**, No 8, 1001 (1974).

[96] A. Williams and D. Smith, *Nucl. Inst. and Meth.*, **112** 131 (1973).

[97] Dr. R. W. Engstrom, (1980) *Photomultiplier Handbook*, RCA Solid State Division, Electro Optics and Devices, Lancaster, PA 17604, USA.

[98] The Coil Task Force of the SNO Collaboration, *Cancellation of the Earth's Magnetic Field*, SNO report SNO-STR-91-5 (1991).

[99] E. D. Hallman *et al.*, SNO report SNO-STR-90-101 (1990).

[100] P. Skensved and B. C. Robertson, SNO report SNO-STR-90-27 (1990).

[101] F. James and M. Roos, *MINUIT - Function Minization and Error Analysis*, CERN Program Library D506 (1988). Also F. James, *MINUIT - Interpretation of the Errors on Parameters*, CERN Program Library D506 - Supplement (1988).

[102] M. D. Lay, N. West and D. L. Wark, *It's Alive - The birth of SNOMAN*, SNO report SNO-STR-91-077 (1991).

[103] A direct measurment of the ^{3}He(n,γ)^{4}He cross-section has been made by R. W. Zurmühle *et al.*, *Phys. Rev.* **132** 751 (1963), with the result 42 μb. A larger result can be obtained by requiring detailed balancing of the reaction ^{4}He(γ,n)^{3}He measured by B. L. Berman *et al.*, *Phys. Rev.* **C22**, No 6, 2273 (1980), and *Phys. Rev.* **C27**, No 5, 1866 (1983). Currently the ^{3}He(n,γ)^{4}He cross-section is being measured at Queens University by Leslie *et al.*

[104] P. Paul *et al.*, *Phys. Rev.* **164**, No 4, 1332 (1967).

[105] G. A. Bartholomew *et al.*, *Nucl. Data,* **A3** 367 (1967).

[106] M. A. Lone, R. A. Leavitt and D. A. Harrison *Atomic Data Nucl. Data Tables* **26** 511 (1981).

[107] J. R. Leslie, *Calibration - Aims and Implementation* SNO report SNO-STR-91-017 (1991). See also Annex 8 of SNO-STR-87-12, in support of the SNO proposal.

[108] J. B. Birks, (1967) *The Theory and Practise of Scintillation Counting*, Pergamon Press.

[109] R. T. Cox, *Phys Rev.,* **66** 106 (1944), as quoted by Jelley [2].

[110] I. J. R. Aitchison and A. J. G. Hey, (1989) *Gauge Theories in Particle Physics*, Adam Hilger imprint by IOP Publishing, Bristol, England.

[111] J. D. Bjorken and S. D. Drell, (1964) *Relativistic Quantum Mechanics*, McGraw-Hill Book Company.

[112] N. Cabibbo, *Phys. Rev. Lett.,* **10** 531 (1963).

[113] D. H. Perkins, (1987) *Introduction to High Energy Physics*, Addison-Wesley Publishing Company Inc.

[114] L. D. Landau, *Sov. Phy. JETP,* **3** 920 and **5** 101 (1957). See also L. D. Landau, *Sov. Phy. JETP,* **8** 70 (1959). These references are quoted by Ashcroft and Mermin (see below).

[115] N. W. Ashcroft and N. D. Mermin, (1976) *Solid State Physics*, HRW International edition.

[116] G. L. Weissler, *Handbuch der Physik XXI,* **24** 342 (1956).

[117] H. E. Hintergger, *Phys. Rev.,* **96** 538 (1954).

[118] C. Walker and G. L. Weissler, *Phys. Rev.,* **97** 1178 (1955).

[119] Burton, *Phys. Rev.,* **72** 531 (1947).